DOE/ID-10971

Large-Eddy Simulation of Turbulent Circular Jet Flows

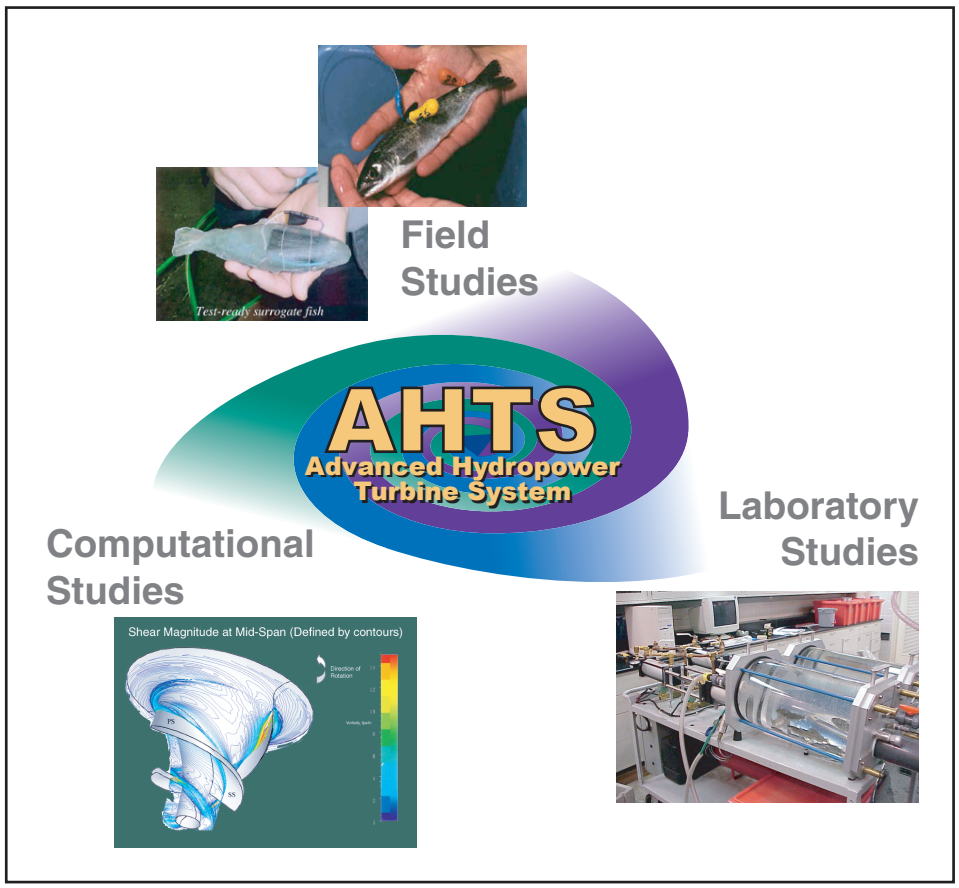

Hydropower R&D

IN PARTNERSHIP WITH THE ENVIRONMENT

United States
Department of Energy

DISCLAIMER

OAK RIDGE NATIONAL LABORATORY
managed by
UT-BATTELLE, LLC
for the
UNITED STATES DEPARTMENT OF ENERGY
under Contract DE-AC05-00OR22725

Printed in the United States of America

Available to DOE and DOE contractors from the
Office of Scientific and Technical Information,
P.O. Box 62, Oak Ridge, TN 37831-0062;
ph: (865) 576-8401
fax: (865) 576-5728
email: reports@adonis.osti.gov

Available to the public from the National Technical Information Service,
U.S. Department of Commerce, 5285 Port Royal Rd., Springfield, VA 22161
ph: (800) 553-6847
fax: (703) 605-6900
email: orders@ntis.fedworld.gov
online ordering: http://www.ntis.gov/ordering.htm

DOE/ID-10971

Large-Eddy Simulation of Turbulent Circular Jet Flows

S. C. Jones
F. Sotiropoulos
School of Civil and Environmental Engineering
Georgia Institute of Technology

M. J. Sale
Oak Ridge National Laboratory

July 2002

Prepared for
the U.S. Department of Energy
under Contract DE-AC05-00OR22725

Executive Summary

In this report, we develop a numerical method for carrying out large-eddy simulations (LES) of turbulent free shear flows and apply the method to simulate the flow generated by a nozzle discharging into a stagnant reservoir. Our objective is to elucidate the complex features of the instantaneous flow field to help interpret the results of recent biological experiments in which live fish were exposed to the jet shear zone. The fish-jet experiments were conducted at the Pacific Northwest National Laboratory (PNNL) under the auspices of the U.S. Department of Energy's Advanced Hydropower Turbine Systems program. The experiments were designed to establish critical thresholds of shear and turbulence-induced loads to guide the development of innovative, fish-friendly hydropower turbine designs.

This report describes in detail the unsteady governing equations and the time-accurate numerical method developed for solving them. Calculations are carried out for a forced circular jet at Reynolds numbers of 100,000 and 300,000. The numerical model is validated by time-averaging the computed instantaneous flow and comparing the results with the mean flow and turbulence statistics measured at PNNL. The comparisons reveal that the simulated mean flow and turbulence statistics are in good overall agreement with the measurements, especially in the fully turbulent region. The calculated instantaneous flow fields are analyzed in detail and their complex, highly three-dimensional, and unsteady structure is juxtaposed with the relative simple structure of the time-averaged flows. Particle tracking studies are also carried out to analyze the computed flow fields from the so-called Lagrangian viewpoint, that is, from the viewpoint of a fish transported by and interacting with the turbulent flow.

The results presented here demonstrate that the actual flow environment experienced by the fish is vastly more complicated than the mean flow and underscore the need for understanding and quantifying the structure of turbulence at the fish scale to guide the design and interpret the results of laboratory experiments with live fish. Our particle tracking simulations demonstrate the need for developing an advanced numerical model for simulating fish passage in complex turbulent flows. That is, a model is needed that couples the fish motion with the unsteady flow and that can simulate the complex deformations of the fish body observed in the laboratory experiments. Employed in conjunction with unsteady numerical simulations of turbulence at the fish-scale and laboratory experiments, such a model should help us understand the mechanisms that lead to injury and mortality in turbulent flows and allow to the development of refined guidelines for improving the fish friendliness of hydropower turbines.

Acknowledgments

This project was conducted under the general guidance of Mike Sale of the Environmental Sciences Division at Oak Ridge National Laboratory (ORNL). The authors thank Brennan Smith, TVA, and Mufeed Odeh, USGS, for their helpful peer-review comments on an early draft of this report. The contributions of Glenn Čada and Charles C. Coutant also of the Environmental Sciences Division at the Oak Ridge National Laboratory are also greatly appreciated. Funding was provided by the U. S. Department of Energy Office of Energy Efficiency and Renewable Energy Hydropower Program. DOE's Hydropower Program is managed by Peggy A. M. Brookshier through the DOE Idaho Operations Office in Idaho Falls, Idaho. The research described in this report was conducted primarily at The Georgia Institute of Technology (Georgia Tech), under subcontract with ORNL, which is managed by UT-Battelle, LLC, for the U.S. Department of Energy under contract DE-AC05-00OR22725.

Contents

Glossary

AHTS	Advanced Hydropower Turbine System Program of the U.S. Department of Energy
DNS	Direct numerical simulation. A means of predicting turbulent flows where all scales of motion present in the flow are resolved. Direct numerical simulations are extremely expensive and can only be performed for relatively simple turbulent flows at relatively small Reynolds numbers.
Eulerian	A frame of reference (or coordinate system) that is fixed in space. Contrast with Lagrangian.
Lagrangian	A frame of reference (or coordinate system) that is fixed on a particular mass of fluid (or on a fish) which moves with the flow.
Large-scale motion	Turbulent flows contain motion at a range of scales. Large-scale motions or coherent structures occur at scales comparable to the flow geometry, and their dynamics are primarily governed by inviscid instabilities. For the jet flow, large scale motion occurs at scales similar to the diameter of the jet nozzle.
LDV	Laser Doppler Velocimetry is an experimental technique to measure the velocity of a fluid by shining a laser into the flow and measuring the reflected light.
LES	Large-eddy simulation. An approach for simulating turbulent flows by resolving directly all turbulent eddies whose size is greater than the spacing of the computational grid. Eddies smaller than the grid spacing are modeled via a so-called subgrid-scale model.
Navier–Stokes equations	Equations that describe the motion of fluids. The equations are derived from fundamental scientific laws—the laws of conservation of mass, momentum, and energy. See Eqs. 4, 5 on p. 16.
Pressure gradient	Force due to pressure per unit volume of the fluid. See Eq. 36, p. 48.
RANS	The Reynolds-averaged Navier–Stokes equations. See Reynolds

averaging.

Reynolds averaging	A method to represent the instantaneous velocity (and pressure) in a turbulent flow field by decomposing it into a time-averaged, mean part and a random fluctuating part.
Reynolds number (*Re*)	The ratio of inertial forces to viscous forces in a flow. A high *Re* indicates that the flow is turbulent (the definition of what is high varies widely from one type of flow to another). For the jet flow in this report, *Re* is calculated as Ud/ν where U is the mean velocity at the jet nozzle, d is the diameter of the jet nozzle, and ν is the kinematic viscosity of the water.
Reynolds stresses	A measure of the transport of momentum by turbulent velocity fluctuations. The Reynolds stresses result from Reynolds averaging the Navier–Stokes equations. See the discussion on p. 37.
Small-scale motion	In a turbulent flow, the small-scale motion corresponds to the flow at scales where viscosity becomes important.
Strain-rate magnitude	A measure of the effect of shear within the flow. Shear would act to tear apart a body within the flow. See Eq. 39, p. 49.
Turbulence kinetic energy, *k*	A measure of the amount of energy in a turbulent flow due to the fluctuating part of the velocity. See Eq. 35, p. 37.
Velocity gradient	A measure of how fast the velocity is changing with direction at a point within a flow. Because there are three directions in space and a velocity component for each direction, there are nine components (3×3) or different combinations of velocity gradient in a three-dimensional flow. These nine combinations make up the velocity-gradient tensor. See Eq. 1 on p. 5 and the accompanying discussion.
Vortex	A region in the flow were vorticity of sufficient strength concentrates for sufficiently long time to make particle paths spiral. A tornado is a well-known example of a vortex.
Vorticity magnitude	A measure of the intensity of vorticity at a point within the flow. Vorticity would tend to rotate a body (fish) within the flow. See Eq. 36, p. 48.

Figures

Figures (continued)

Figures (continued)

1. Introduction

A major objective of the work currently sponsored by U.S. Department of Energy's (DOE) Advanced Hydropower Turbine System (AHTS) program is to enhance the fundamental understanding of the mechanisms that lead to disorientation, injury, and mortality of fish passing through hydropower installations. Understanding the interaction of fish with the flow field is critical prerequisite for arriving at innovative design modifications that enhance the environmental compatibility of existing hydropower facilities. Achieving this objective, however, is particularly challenging for a number of reasons. First and foremost, the flow environment experienced by fish in the field, that is the flow within the hydropower plant, occurs within very complex geometrical configurations (the various subsystems of a hydropower plant) and is characterized by strong three-dimensionality, both forced and naturally excited unsteadiness, intense large scale vortices, high levels of turbulence anisotropy, regions of rapid pressure changes, and cavitation. Second, very little is known about how fish respond to and are affected by these complex flow phenomena. Issues such as the biological effect of intense swirling motion, shearing zones, and turbulence on passing fish are far from being understood (see Coutant and Whitney (2000) for an excellent, up-to-date review).

A first step toward enhancing our understanding of these complex issues is to conceive and carry out small-scale laboratory experiments with real fish. Such experiments should be designed so that they are representative of the flow conditions that fish are likely to encounter in specific areas within the power plant. By quantifying in detail the structure of the flow, via both laboratory measurements and numerical simulations; monitoring the interaction of fish with the flow; and recording the impact of this interaction on their biological integrity one can gain valuable insights that can lead to specific design guidelines for fish-friendly hydropower turbines. Along these lines, the Pacific Northwest National Laboratory (PNNL) recently carried out a series of experiments aimed at studying the effect of intense shearing zones and turbulence on fish (Neitzel et al. 2000). The specific flow field investigated by PNNL is that created by a nozzle issuing into a reservoir filled with stagnant water. PNNL researchers first carried out detailed measure-

ments to quantify the mean flow and turbulence structure in the near field of the resulting jet flow. Subsequently they introduced real fish into the shear zone of the jet, recorded their trajectories using video photography, and documented the biological effects of exposing fish to this flow. By varying the flow rate of the jet, they exposed fish into varying levels of flow-induced forces and attempted to quantify the biological effects of shear and turbulence. It should be pointed out that within this jet configuration fish are likely to be exposed to shear and turbulence levels that could occur in a variety of regions within the power plant where strong shear zones exist. For example, in Kaplan turbines strong jet-like flows are likely to occur locally near the gaps between the runner blade and the hemi-spherical base on the hub on which the blades are mounted (Franke et al. 1997; Fisher et al. 1999). Such gaps are believed to be the source of injuries in Kaplan turbines, and turbine manufacturers are making considerable efforts to modify existing designs so that adverse effects are minimized (Franke et al 1997). Other areas where shearing zones as intense as those created in this experiment may be encountered include the clearance zone between the tip of a runner blade and the shroud and the wakes of stay vanes, wicket gates, and the runner blades.

The PNNL experiments have shed new light on the biological effects of shear and turbulence on fish. There is, however, one important aspect of the fish/flow interaction that cannot be fully understood with laboratory measurements alone. Namely, laboratory experiments (at least for those experimental methods that currently can be practically used in the biological laboratory) can only provide information about the mean flow characteristics—the time-averaged or Reynolds-averaged flow field. Yet in the laboratory and in the field, fish interact with and get injured by the instantaneous flow field and not the steady mean flow field, which they never experience. For complex turbulent flows such as those we investigate here, the instantaneous flow is vastly different than the steady time-averaged flow field. For example, for the circular jet flow studied by PNNL the time-averaged flow is, in the absence of any disturbances, a “simple” steady axisymmetric flow field with the primary shearing force produced by the derivatives of the axial velocity with respect to the radial direction. The instantaneous flow field, however, is a highly three-dimensional flow characterized by intense velocity and pressure temporal fluctuations and strong velocity gradients of all three-velocity components along all three spatial direc-

tions. Therefore to interpret and better understand the biological impact of the flow on fish, there is a need to quantify in great detail the structure of the instantaneous flow within the jet-shearing zone.

The objective of this work is to supplement the knowledge gained from the PNNL experiment by carrying out large-eddy numerical simulations (LES) of the turbulent jet flow to gain a more comprehensive understanding of the actual flow environment experienced by fish in the laboratory. In a LES, we only resolve directly the scales of turbulent eddies that are larger than the spacing of the computational mesh. Eddies smaller than the grid spacing (so-called subgrid scale eddies) are modeled with an appropriate turbulence model. Since we are only interested in the effects of eddies whose size is comparable to the size of the fish body (see subsequent discussion), LES is ideally suited for our present objective—provided of course that the spacing of our computational mesh is considerably smaller than the typical size of the fish used in the experiment. It is important to note that a meaningful LES of wall bounded, three-dimensional flows at high Reynolds numbers, and in complex geometries (such as those that occur within the power plant) are not feasible with today's computational resources. Yet, LES is ideally suited for the present jet flow because it is a free-shear flow (the shear zone of interest is far from solid boundaries) and good resolution can be obtained for Reynolds numbers within the range studied in the experiment on computational grids well within the reach of present day computers (Gristein et al. 1996). The accuracy of our numerical computations is demonstrated by comparing the mean flow velocities and turbulence statistics extracted from the LES simulations with the PNNL laboratory measurements. The computed instantaneous flow is then analyzed to quantify the differences between the mean flow and the actual flow experienced by the fish. Lagrangian particle tracking is employed to illustrate the vastly different flow properties (shearing stresses, pressure gradients, vorticity) encountered by particles originating from the same point in the flow but at different times. Even though in this study a fish is over simplified to be a passive material point, these computations underscore the need for developing a model that can simulate the interaction of three-dimensional fish bodies with the unsteady instantaneous flow.

The outline of this report is as follows. In §2, we review some fundamental fluid mechanics concepts essential for understanding and quantifying the biological effects of shear and turbu-

lence on fish. In §3, we review prior work on turbulent jet flows to gain an understanding of the physics of such flows. In §4, we present the governing flow equations, the numerical method used to solve them, and the numerical method used to calculate particle trajectories. In §5, we show comparisons with the PNNL measurements. In §6, we discuss in detail the computed results, analyze in detail the structure of the instantaneous flow, and juxtapose it with that of the time-averaged flow field. In §7, we compare the predicted flow fields at Reynolds numbers of 100,000 and 300,000. In §8, we present the calculated particle trajectories and illustrate the broad variations of flow properties along various trajectories. Finally in §9, we summarize the main conclusions of this work and provide recommendations for future research.

2. Shear- and Turbulence-Induced Mortality: A Fluid Mechanics Perspective

Since the main emphasis of the PNNL experiments was to quantify the biological effects of shear and turbulence on fish, let us briefly review some fundamental fluid mechanics concepts regarding the definition of shear and its relation to the turbulence in a fluid flow. This brief review will be useful in our subsequent discussion as it will help us evaluate the completeness and usefulness of existing experiments as well as identify specific needs for future experiments.

The flow field in most subsystems of a hydropower plant is complex, highly three-dimensional, and unsteady. The level of spatial complexity of a flow field can be quantified in terms of the gradients of the three velocity components (u, v, w) along each spatial direction (x, y, z). For a three-dimensional flow, these gradients comprise a 3 × 3 velocity-gradient tensor, defined as follows:

$$\nabla\vec{V} = \begin{bmatrix} \frac{\partial u}{\partial x} & \frac{\partial u}{\partial y} & \frac{\partial u}{\partial z} \\ \frac{\partial v}{\partial x} & \frac{\partial v}{\partial y} & \frac{\partial v}{\partial z} \\ \frac{\partial w}{\partial x} & \frac{\partial w}{\partial y} & \frac{\partial w}{\partial z} \end{bmatrix} \tag{1}$$

As a general rule, the complexity of a flow field is directly proportional to the number of non-zero components of the above tensor. For example, for parallel Couette flow (flow driven by two flat belts moving at different speeds), the simplest viscous flow field, the velocity gradient tensor has only non-zero component, $\partial u/\partial y$. Within the power plant, on the other hand, there are no regions where some components of the velocity gradient tensor are identically zero, although in certain areas some may be considerably smaller than others. For instance, within the intake the spatial derivatives of u, the velocity component along the predominant flow direction, should be expected to be significantly greater than the derivatives of the other velocity components. Further downstream, however, the geometrical complexities of the distributor and the wicket gates, the rotation of the runner, and the complex curvatures and area expansion within the draft-tube make all velocity derivatives non-zero and of comparable relative magnitude.

For a viscous fluid, the velocity-gradient tensor produces a shear-stress field, which is also quantified in terms of a 3 × 3 tensor, the so-called shear-stress tensor. For a Newtonian fluid of viscosity μ, this tensor is symmetric and is expressed in terms of the velocity gradients as follows:

$$\overline{\overline{t}} = \begin{bmatrix} t_{xx} & t_{xy} & t_{xz} \\ t_{xy} & t_{yy} & t_{yz} \\ t_{xz} & t_{yz} & t_{zz} \end{bmatrix} \equiv m\left(\nabla\vec{V} + \nabla\vec{V}^T\right) = m\begin{bmatrix} 2\dfrac{\partial u}{\partial x} & \dfrac{\partial u}{\partial y}+\dfrac{\partial v}{\partial x} & \dfrac{\partial u}{\partial z}+\dfrac{\partial w}{\partial x} \\ \dfrac{\partial u}{\partial y}+\dfrac{\partial v}{\partial x} & 2\dfrac{\partial v}{\partial y} & \dfrac{\partial v}{\partial z}+\dfrac{\partial w}{\partial y} \\ \dfrac{\partial u}{\partial z}+\dfrac{\partial w}{\partial x} & \dfrac{\partial v}{\partial z}+\dfrac{\partial w}{\partial y} & 2\dfrac{\partial w}{\partial z} \end{bmatrix} \tag{2}$$

Let us now consider a small material surface of area *A* within the flow field that is arbitrarily oriented with respect to the local velocity vector. The orientation of this surface can be defined in terms of three, mutually perpendicular, unit vectors $\dot{n}_1, \dot{n}_2, \dot{n}_3$—$\dot{n}_1$ and $\dot{n}_2$ are oriented parallel to the surface and $\dot{n}_3$ is normal to the surface. The components of the shear stress tensor will induce a shearing force, $\dot{F}_S$, on this surface which can be expressed in terms of its components along each of the three unit vectors ($\dot{F}_s = \dot{F}_{s_1} + \dot{F}_{s_2} + \dot{F}_{s_3}$):

$$\vec{F}_{s_k} \equiv \overline{\overline{t}} \cdot \vec{n}_k = \begin{bmatrix} t_{xx}n_{k_x} + t_{xy}n_{k_y} + t_{xz}n_{k_z} \\ t_{xy}n_{k_x} + t_{yy}n_{k_y} + t_{yz}n_{k_z} \\ t_{xz}n_{k_x} + t_{yz}n_{k_y} + t_{zz}n_{k_z} \end{bmatrix} \quad \text{for } k = 1,2,3 \tag{3}$$

where n_{k_x}, n_{k_y}, and n_{k_z} are the three Cartesian components of the $\dot{n}_k$ unit vector. The above equation serves to demonstrate that in a complex three-dimensional flow the shearing force acting on an arbitrarily oriented surface has components along all three spatial directions. Furthermore, it is important to emphasize that to determine the total flow-induced force on the material surface under consideration we should also consider the contribution of the pressure field, which creates a force acting along the $\vec{n}_3$ direction, that is, the direction normal to the surface.

Let us consider now a fish traveling with velocity $\vec{V}_f$ within a complex three-dimensional flow environment. With respect to an observer that moves with the fish, the ambient flow velocity is $\vec{V} - \vec{V}_f$. Thus, Eqs. 1 and 2 can be readily applied to obtain the velocity gradient and stress tensors as observed by the fish simply by replacing *u*, *v*, and *w* with $u - u_f$, $v - v_f$, and $w - w_f$.

If the material surface we considered in our previous discussion is now thought to represent a small panel on the fish skin, then Eq. 3 can be used to calculate the three components of the shearing forces acting on that panel. Since fish bodies exhibit both longitudinal and transverse curvatures, the orientation of the $\vec{n}_1,\vec{n}_2,\vec{n}_3$ vectors changes continuously as we move along the fish skin. For that reason, it is more convenient to express the resulting shearing forces in terms of a coordinate system whose origin is attached to a fixed point on the fish body (say the center of gravity of the fish) and whose axes are always oriented along the principal and two minor axes of the fish body. Clearly the total shearing force will have, in the general case, three non-zero components along each one of these axes. The component along the principal axis of the fish (from head to tail) will act to stretch or compress the fish body, leading to possible decapitation and descaling, and could also induce bending loads. The components along the two lateral directions, on the other hand, would tend to compress or stretch the fish laterally as well as produce twisting or bending loads. It is, therefore, clear from these general qualitative arguments that shear experiments, that are representative of real-life situations encountered by passing fish in hydropower plants, should be able to reproduce, quantify, and correlate with specific injuries all these possible three-dimensional loads.

Most previous shear experiments have been conducted by introducing fish in the turbulent shear layer generated by a high-speed jet discharging into a tank of stagnant water (Groves 1972; Turnpenny et al. 1992)—experiments involving the flow between two co-rotating cylinders have also been reported (Morgan et al. 1976), but these have focused on the effects of mild shear on eggs and larvae of bass and perch. In such a flow field, the predominant components of the mean (time-averaged) velocity-gradient and shear-stress tensors are du/dy and t_{xy}, respectively. It is important to emphasize, however, that in the vicinity of the jet the instantaneous flow field, which is the actual environment encountered by the fish, is very complex, highly three-dimensional, unsteady, and characterized by a broad range of spatial and temporal scales. In other words, in such experiments, and for that matter in any flow field in which strong mean velocity gradients exist, it is very difficult, if not impossible, to isolate the effects of “shear” from those of “turbulence”—this point is further discussed in more detail in the subsequent section.

The main limitation of previous experiments is the lack of any flow measurements. As a result, the jet velocity is the only parameter that has been traditionally used, (Groves 1972; Turnpenny et al. 1992) to estimate the magnitude of the shearing force experienced by the fish and develop correlations with observed adverse effects, such as disorientation, severe injuries, and even mortality. Although this velocity can be used to come up with an order of magnitude estimate of the mean shearing force experienced by the fish, it is important to recognize that any particular injury could have been the result of an instantaneous, extreme turbulent flucuation that could be considerably higher than the mean. To estimate the likelihood and intensity of such events, it is necessary to supplement whatever method of fish tracking and observation that is employed with detailed mean velocity and turbulence statistics measurements, such as those reported in the recent PNNL experiments.

Moreover, although jet experiments can expose fish to very high levels of shearing forces and turbulence fluctuations, they do not necessarily represent, either quantitatively or qualitatively, all real-life situations encountered within a power plant. Quantitatively similar flow fields, in the sense that they exhibit a single dominant component of the mean shear-stress tensor, could of course occur in regions within the power plant such as near gaps at the downstream end of overhanging wicket gates or hub gaps of Kaplan turbines, where the local geometry could possibly induce high-speed jet-like flow fields. Clearly, however, these experiments are not representative of situations such as those a fish could encounter within a swirling flow core entering a region of strong adverse pressure gradients (draft-tube inlet), or within strong longitudinal vortices developing along a wall, like those emanating from tip clearance gaps. Such regions of the flow are highly three-dimensional, with most components of the mean velocity-gradient tensor being comparable to each other and with distinctly different, as compared to jet configurations, turbulence structures. For that reason, it is important that any attempt to design controlled laboratory experiments with real fish begin with a detailed examination of the flow within the various components of the hydropower plant to identify and carefully classify, based on their overall structure, all local flow scenarios a fish is likely to encounter during its passage. This zonal approach will naturally lead to a number of different laboratory experiments with real fish, each de-

signed to reproduce the features of the various flow zones within the power plant and study the type and intensity of loads they impart on passing fish.

Turbulence-induced fish damage is probably the least understood and most commonly misunderstood injury mechanism. A few simple experiments conducted by introducing "turbulence" into a chamber via a series of water jets (Killgore et al. 1987) have shown that although there is practically no dependence of fish mortality on the frequency of the turbulent fluctuations, there is significant dependence on "turbulence" intensity. To facilitate a more in-depth critical look in such experiments, let us briefly start by discussing some fundamental aspects of turbulent flows.

Turbulent flows are unsteady, three-dimensional, and characterized by a broad range of spatial and temporal scales. Within a hydropower plant, the largest turbulent scales are associated with eddies whose size is comparable to a characteristic dimension of a given subsystem (say, the height of the runner blades or the diameter of the draft-tube). The smallest scales (the so-called Kolmogorov scales), on the other hand, are those eddies whose energy is dissipated directly into heat by the molecular viscosity of the fluid. The resulting disparity in scales and the complex, highly non-linear transfer of energy among them is what makes turbulent flows extremely difficult to study and understand. In hydropower plants, this disparity is further exaggerated by the large size of real-life hydropower turbines and the very high Reynolds numbers—the smallest turbulent scales tend to become smaller as the Reynolds number increases and the relative importance of the molecular viscosity of the fluid diminishes.

The most common engineering approach for describing a turbulent flow field is the so-called Reynolds decomposition. The instantaneous values of the various flow quantities (velocity components and pressure) are expressed as a sum of a mean value plus a fluctuating, about the mean, component of variable frequency and intensity. It is important to recognize that in hydropower turbines even the resulting mean value is not necessarily constant in time, but it contains large scale organized temporal changes in the flow, such as those induced by the rotation of the runner. By substituting the Reynolds decomposition of the velocity components and pressure into the instantaneous equations of motion (continuity and momentum) and averaging the resulting equations, we obtain the so-called Reynolds-averaged Navier-Stokes (RANS) equations. The resulting equations look very similar to the original instantaneous Navier-Stokes equations, but

they are formulated in terms of the mean velocity and pressure components (Eqs. 1 and 2 are still applicable, but now they represent the mean velocity-gradient and shear-stress tensors, respectively). Most importantly, the Reynolds-averaged momentum equations contain additional terms, the so-called Reynolds stresses, that represent the effects of turbulent velocity fluctuations on the evolution of the mean flow quantities. We refer to these terms as stresses because like the mean shear-stress tensor given by Eq. 2, which represents transport of momentum by molecular action in the flow, they too represent momentum transport but due to the action of turbulent eddies. Since turbulence is far more effective in transporting momentum and enhancing mixing, the Reynolds stresses are, for the most of the flow field, considerably larger than the viscous stresses. The production and evolution of the Reynolds stresses are governed by a set of very complex transport equations, which contain the mean velocity components and their gradients, and correlations involving Reynolds-averaged products of velocity and pressure fluctuations as well as triple fluctuating velocity products. The importance of these equations for our discussion lies in the fact that they clearly demonstrate that Reynolds-stresses, and, thus, turbulence, can be produced and sustained only when gradients in the mean velocity exist.

The above discussion has important implications for fish experiments. It is obvious that it is very difficult to design experiments in which the effects of mean shear as an injury-inducing mechanism can be separated from those of turbulence, as the former is responsible for producing and affecting the structure of the latter. Although in principal experiments could be carried out by introducing fish into a homogeneous turbulence field (which in the absence of mean shear will decay in time), it is unlikely that such a situation will ever occur in a real hydropower plant where the geometrical complexities induce intense velocity gradients and, thus, continuously produce turbulence. Therefore, rather than trying to isolate the effects of mean shear from those of turbulence we, once again, recommend that the zonal experimental approach described above be adopted. By carefully designing controlled laboratory experiments that reproduce various local flow scenarios within the hydropower plant, we can ensure that fish will be exposed to flow environments whose mean flow and turbulence structures are broadly similar to typical real-life situations.

It should be recognized, however, that meaningful quantification of turbulence-induced loads on fish bodies in such experiments is a particularly challenging task. This is because out of the broad range of turbulent eddies present within the hydropower plant, those whose size is comparable to the characteristic length and time scales associated with a given fish will mainly determine the severity of the local loads imparted on the fish body and the extent of possible disorientation effects. The typical length and time scales of such “fish-sized” eddies are determined by the size of the fish and the relative, with respect to the fish, ambient flow velocity. Turbulent eddies much smaller than a “fish-sized” eddy are, from the fish standpoint, small-scale noise. Much larger eddies, on the other hand, contribute to the general motion of the fish within the flow field, while intermediate size eddies could cause mild disorientation. Therefore, quantifying the potential for turbulence-induced injuries and disorientation requires information about the so-called spectral content of turbulence, that is, the manner in which turbulent energy is distributed among the various eddies in the flow. Generally speaking, the more energetic “fish-sized” eddies are the more likely it is that they could inflict serious damage on passing fish.

3. Previous Experimental and Computational Work on Turbulent Circular Jets

In this section, we briefly review previous experimental and computational work with circular, turbulent jets. Our objective is to introduce some of the fundamental instabilities of such flows to facilitate the discussion, interpretation, and analysis of our numerical results that are presented in §§5–8. As we show in those sections, our numerical simulations reveal instability modes that are very similar to those documented in previous experiments.

Fig. 1 shows an experimental picture of a turbulent jet. The jet can be divided into two regions: (1) a developing region also called the potential core and (2) a fully developed, turbulent region. Large-scale structures at the end of the potential core are clearly evident in Fig. 1 just before the jet breaks up into a completely random, turbulent flow. As for the far-field region, it has been widely studied and much of the early experimental work on the turbulence characteristics of far field jets was reviewed by Hinze (1975) and by Rajaratnam (1976).

We, however, are most interested in the near field of the jet. The end of the potential core occurs at $x \sim 10d$ where x is the distance measured from the jet nozzle and d is the diameter of the nozzle. The precise end of the potential core depends strongly on the conditions at the exit of the nozzle, and the focus of much current research on jets is on how to manipulate those initial conditions to shorten this potential core and to increase entrainment and mixing (Zaman et al. 1994) or to decrease noise production (Samimy et al. 1993).

Fig. 2(a) shows a close-up, three-dimensional picture of the potential core for an unforced circular jet, and Fig. 2(b) shows the same jet being forced at one of the fundamental frequencies of the jet. As these figures show, vortex rings play a dominant role in the transition of the jet from laminar to turbulent. The forced jet (Fig. 2b) shows several initially stable, distinct vortex rings becoming unstable as the jet transitions to turbulence. These vortex rings and other detectable large-scale motions are collectively known as coherent structures—and understanding how these structures form, merge, interact, and break is one of the fundamental keys to understanding how jets work (Gutmark and Grinstein 1999).

Fig. 3 shows an experimental picture from Lasheras and Prestridge (1997) of a five-lobed jet where the axial forcing increases from Fig. 3(a) to 3(d). The last two of these pictures show very distinct, mushroom-shaped, lateral ejections that extend radially outward from the jet. The presence of these types of coherent structures have been shown to decrease the length of the potential core by 4-6 times over normal circular jet (Gutmark and Grinstein 1999), and thus, increase its mixing effectiveness.

Previous computational work on turbulent, circular jets, like most computational work, has been driven by the availability of computer resources. Some of the earliest studies were two-dimensional simulations (assuming axisymmetric flow) that followed the jet in space and time (Grinstein et al 1987). Martin and Meiburg (1991) used vortex methods to investigate the susceptibility of axisymmetric jets to axial and azimuthal perturbations. With this technique, they produced jet cross-sections that looked like Fig. 3(a). Later work by Danaila et al. (1997) used spectral-element methods to perform direct numerical simulations of very low Reynolds number jets (200 to 500) to investigate the relative effects of helical (twisting) and axisymmetric perturbations. Perhaps the most comprehensive computational study to date of the circular jet was by Grinstein et al. (1996). They computed compressible (but subsonic) flow along with the chemical reactions associated with combustion using a modified large-eddy simulation technique.

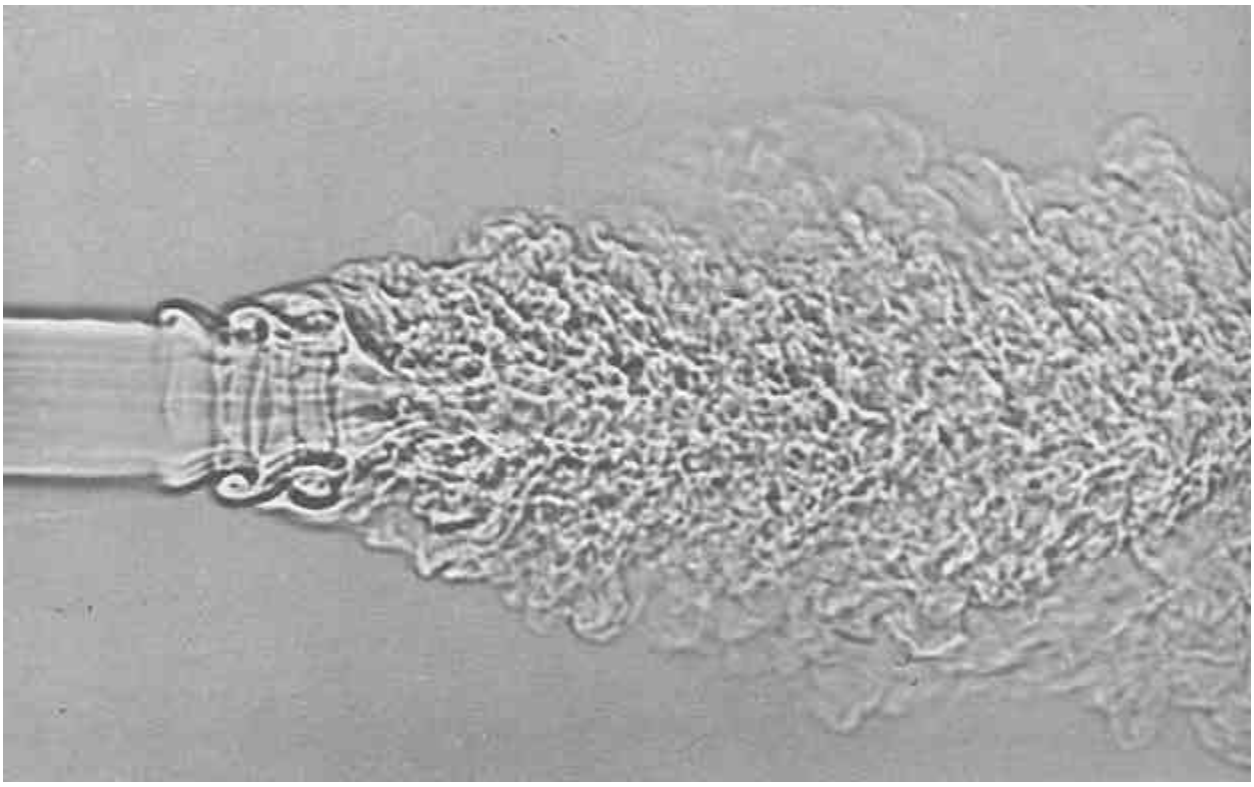

Figure 1. A two-dimensional picture of a turbulent, circular jet showing the near-field and far-field regions (Photo by F. Landis and A. H. Shapiro. Published in Van Dyke 1982).

a) b)

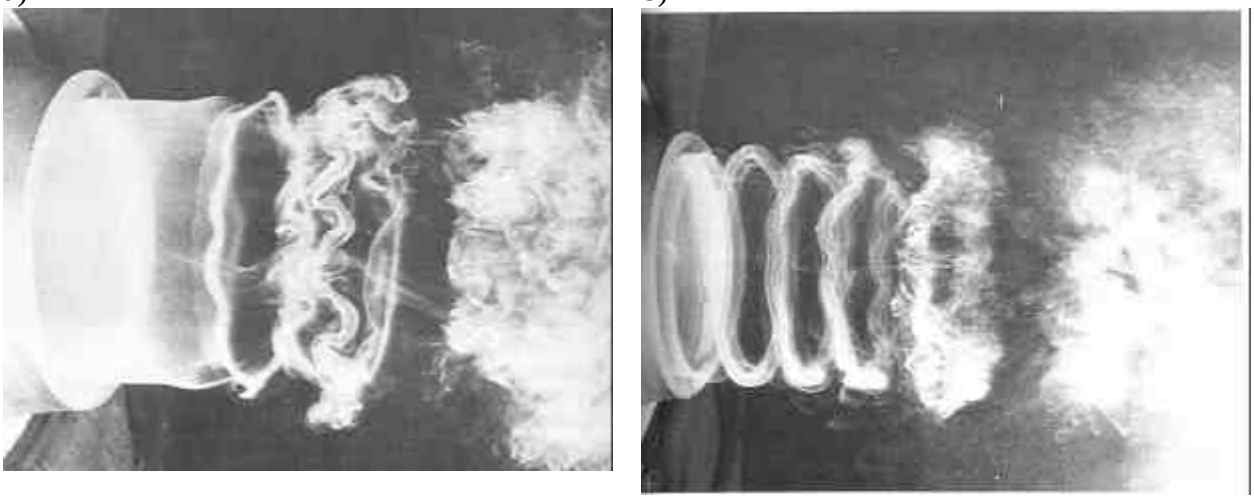

Figure 2. Three-dimensional picture of the potential core of (a) an unforced circular jet and (b) a forced circular jet (Photos by R. Willie and A. Michalke. Published in Van Dyke 1982).

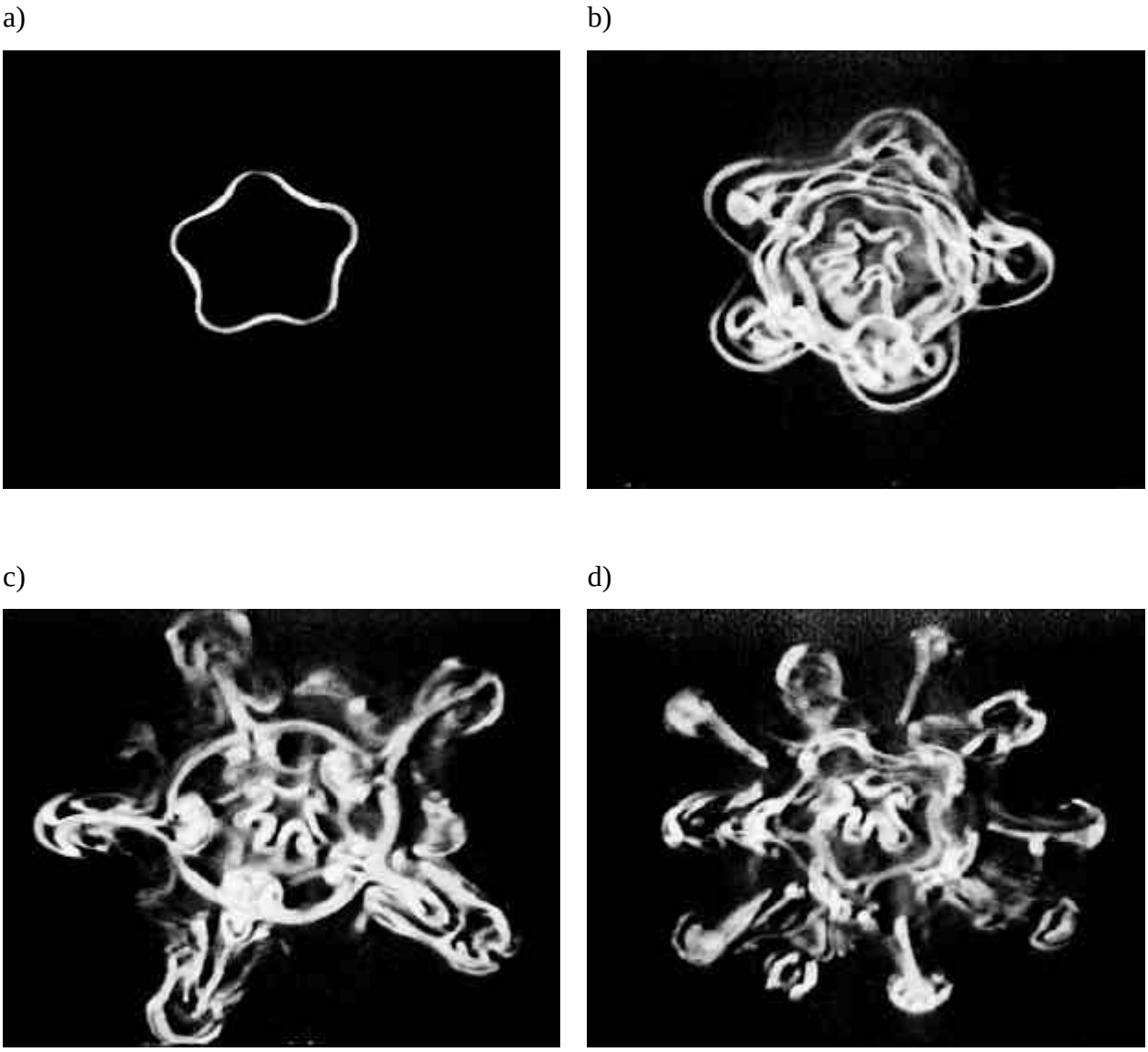

Figure 3. Flow visualization of a five-lobed axially forced jet showing distinct modes of lateral ejections (Lasheras and Prestridge 1997).

4. Description of the Numerical Model

This section presents in detail the governing flow equations for the LES approach (§4.1), the numerical method (§4.2) for solving these equations for turbulent, circular jet flows, the numerical treatment of outflow boundary conditions (§4.3), and the Lagrangian particle tracking algorithm (§4.4) for calculating the trajectories of passive particles in an unsteady, three-dimensional flow. The LES code developed here is based on the Georgia Tech Reynolds-averaged Navier–Stokes (RANS) flow solver, which has been successfully used to predict the turbulent flow in a wide variety of complex geometries. Details on the original development of this code can be found in Lin and Sotiropoulos (1997a, 1997b), and its success for a variety of complex geometries is reviewed by Sotiropoulos (2001).

4.1 Governing equations and turbulence model for LES

In LES, only turbulent eddies larger than the grid size are directly computed while the effect of smaller eddies (so-called subgrid eddies) is modeled. To separate the large eddies from the small eddies, the three-dimensional, instantaneous Navier–Stokes equations are filtered in space. This spatial filtering operation is designed to remove from the equations scales of motion whose size is smaller than the filter width (see Piomelli (1999) for a recent review of the fundamentals of LES). The resulting spatially filtered equations—the LES equations—look exactly like the Navier-Stokes equations for the spatially averaged velocity pressure fields plus an additional subgrid term, which represents the effects of the small eddies on the resolved flow. For three-dimensional, incompressible flows, the LES equations read in Cartesian tensor notation as follows:

$$\frac{\partial u_i}{\partial x_i} = 0 \tag{4}$$

$$\frac{\partial u_i}{\partial t} + u_j \frac{\partial u_i}{\partial x_j} + \frac{\partial p}{\partial x_i} - \frac{1}{\mathrm{Re}} \frac{\partial^2 u_i}{\partial x_j^2} + \frac{\partial t_{ij}}{\partial x_j} = 0 \tag{5}$$

where x_i are the Cartesian coordinates with i = 1, 2, 3; u_i are the spatially averaged velocity components; p is the spatially averaged pressure; Re is the Reynolds number; and t_{ij} is the subgrid-stress (SGS) tensor, which needs to be modeled for closure.

We should note that the above equations look exactly like the RANS equations but the latter govern the transport of time-averaged quantities. Perhaps the most important difference between the RANS and LES equations is that in the former the t_{ij} term is the Reynolds-stress tensor, which does not depend on the grid spacing but rather on the gradients of the mean flow and the local turbulence length and velocity scales. In an LES, however, the subgrid stress tensor is proportional to the local grid spacing and the gradients of the resolved flow. In other words, if we perform an LES for a given flow and keep on refining the grid spacing, the contribution of the subgrid scales decreases continuously; and when the grid spacing is smaller than the size of the energy dissipating eddies (the so called Kolmogorov scale) the LES formulation becomes an exact direct numerical simulation (DNS)—that is, all scales of motion are resolved. A grid-independent LES is a DNS. In a RANS formulation, on the other hand, we can obtain a grid independent solution for the mean (Reynolds averaged) velocity field because the eddy viscosity does not depend on the grid size.

Many different SGS models have been proposed in the literature with varying levels of complexity and associated computational cost. However, none has been established so far as being suitable for all types of flows (Piomelli 1999). In fact, some LES studies of free shear flows use no explicit turbulence model and rely instead on the dissipation inherent in the numerical scheme to suppress the small, unresolved scales of turbulence (Boris et al. 1992, Grinstein and DeVore 1996). In the present study, we chose the standard Smagorinsky (1963) SGS model, which was successfully used in a recent LES study of turbulent flows in rectangular jets by Wilson and Demuren (1998). The Smagorinsky model is a simple, algebraic model based on the eddy viscosity concept

$$t_{ij} = \frac{1}{3}\delta_{ij} t_{kk} - 2\nu_T S_{ij} \tag{6}$$

which relates the subgrid-scale stresses to the large-scale strain-rate tensor (S_{ij}) and which is calculated as

$$S_{ij} = \frac{1}{2}\left(\frac{\partial u_i}{\partial x_j} + \frac{\partial u_j}{\partial x_i} \right) \tag{7}$$

The other terms in Eq. 6 are d_{ij}, Kronecker's delta, and n_T, the subgrid viscosity. In the Smagorinski model, the eddy viscosity is calculated as

$$n_T = C\Delta^2 |S| \tag{8}$$

where C is a constant set equal to 0.01—a value typically used for shear flows (Wilson and Demuren 1998). For the anisotropic grid used in this study, the grid size Δ is computed at each grid point as

$$\Delta = \left(\Delta_1 \Delta_2 \Delta_3\right)^{\frac{1}{3}} \tag{9}$$

The magnitude of the strain-rate tensor is

$$|S| = \left(2 S_{ij} S_{ij}\right)^{\frac{1}{2}} \tag{10}$$

With Eq. 10, the LES equations are closed.

For the sake of generality, we will describe the numerical method in generalized, non-orthogonal coordinates. To reduce the required computational effort, however, the actual simulations have been carried out using orthogonal coordinates since the computational mesh we employed is Cartesian. The governing equations are transformed in generalized, curvilinear coordinates and formulated in vector form as follows:

$$\Gamma \frac{1}{J}\frac{\partial Q}{\partial t} + \frac{\partial}{\partial x^j}\left(F^j - F_v^{\ j}\right) = 0 \tag{11}$$

where

$$\begin{aligned}
&\Gamma = \mathrm{diag}\begin{bmatrix} 0 & 1 & 1 & 1 \end{bmatrix} \\
&Q = \begin{bmatrix} P & u_1 & u_2 & u_3 \end{bmatrix}^T \\
&F^j = \frac{1}{J}\begin{bmatrix} U^j & u_1 U^j + P x_{x_1}^{\ j} & u_2 U^j + P x_{x_2}^{\ j} & u_3 U^j + P x_{x_3}^{\ j} \end{bmatrix}^T \\
&F_v^{\ j} = \frac{1}{J}\left(\frac{1}{\mathrm{Re}} + n_T \right) g^{mj} \frac{\partial}{\partial x^m}(\Gamma Q)
\end{aligned} \tag{12}$$

The term P is a modified pressure that includes part of Eq. 6, that is,

$$P = p + \frac{1}{3} d_{ij} t_{kk} \tag{13}$$

As for the other terms in Eq. 12, J is the Jacobian of the geometric transformation, $x_{x_i}^{\ j}$ are the metrics of the geometric transformation, U^j are the contravariant velocity components $\left(U^j = u_i x_{x_i}^{\ j}\right)$, and g^{ij} are the components of the contravariant metric tensor $\left(g^{ij} = x_{x_k}^{\ i} x_{x_k}^{\ j}\right)$. For completeness, the resolved strain rate tensor in curvilinear coordinates is

$$S_{ij} = x_{x_j}^{\ k} \frac{\partial u_i}{\partial x_k} + x_{x_i}^{\ k} \frac{\partial u_j}{\partial x_k} \tag{14}$$

4.2 Numerical method

Spatial discretization

A semi-discrete approximation of Eq. 11 can be written as

$$\Gamma \frac{1}{J} \frac{\mathrm{d}Q_{i,j,k}}{\mathrm{d}t} + \frac{\tilde{F}^1_{i+\frac{1}{2},j,k} - \tilde{F}^1_{i-\frac{1}{2},j,k}}{\Delta x^1} + \frac{\left(F_v^1\right)_{i+\frac{1}{2},j,k} - \left(F_v^1\right)_{i-\frac{1}{2},j,k}}{\Delta x^1} + \cdots = 0 \tag{15}$$

where for clarity only derivatives in the x^1 direction are shown. The viscous fluxes at the cell interfaces are discretized using second-order accurate central differencing. The convective fluxes, on the other hand, are approximated in a general manner as

$$\tilde{F}^1_{i\pm\frac{1}{2},j,k} = \frac{1}{2}\left(F^1_{i,j,k} + F^1_{i\pm1,j,k}\right) + D^1_{i\pm\frac{1}{2},j,k} \tag{16}$$

where $D^1_{i\pm\frac{1}{2},j,k}$ is an artificial dissipation flux. In this study, a dissipative flux is constructed using a third-difference matrix-valued artificial dissipation model (Lin and Sotiropoulos 1997a). This dissipation takes the form

$$D^1_{i\pm\frac{1}{2},j,k} = e d_{x^1}\left[\left|A^1\right| d_{x^1} d_{x^1}\right] Q_{i\pm\frac{1}{2},j,k} \tag{17}$$

where e is a positive constant, which controls the amount of dissipation, $\left|A^1\right| = M_1 \left|\Lambda_1\right| M_1^{-1}$, M_1 and Λ_1 are the modal and eigenvalue matrices of $A^1 \equiv \partial F^1 / \partial Q$. For a more detailed description of the matrix-valued dissipation scheme, see Lin and Sotiropoulos (1997a).

Temporal integration

The physical time derivative in Eq. 15 is approximated using second-order accurate, three-point backward finite differencing. To satisfy the continuity equation at every physical time step, a dual (or pseudo) time derivative (see Sotiropoulos and Ventikos (1998) for details) is introduced into the discrete equations as

$$\frac{\mathrm{d}}{\mathrm{d}t} Q_{i,j,k} + \mathbf{R}^m_{i,j,k} = 0 \tag{18}$$

where

$$\mathbf{R}^m_{i,j,k} = \Gamma \frac{3Q^{m+1}_{i,j,k} - 4Q^n_{i,j,k} + Q^{n-1}_{i,j,k}}{2\Delta t} + J \left(\frac{\tilde{F}^1_{i+\frac{1}{2},j,k} - \tilde{F}^1_{i-\frac{1}{2},j,k}}{\Delta x^1} + \cdots \right)^m \tag{19}$$

and the superscripts *m* and *n* denote levels in dual and real time, respectively. To advance the solution to the next physical time step, Eq. 18 is integrated in dual-time using a four-stage, point-wise implicit Runge–Kutta algorithm enhanced with implicit residual smoothing and local dual time-stepping. The resulting multistage algorithm is formulated as follows. For l = 1 to 4,

$$Q^l = Q^{l-1} + \left(\mathbf{I} + a_l \frac{3}{2} \frac{\Delta t}{\Delta t} \Gamma \right)^{-1} \left(-Q^{l-1} + Q^0 - a_l \Delta t \Im^{-1} \mathbf{R}^{l-1} \right) \tag{20}$$

where $\mathbf{I}$ is the unit matrix, a_l are the Runge–Kutta coefficients, and $\Im$ is the standard, constant-coefficient implicit-residual-smoothing operator (see Sotiropoulos and Ventikos (1998) for more details). It should be emphasized that implicit treatment of the first term in the right hand side of Eq. 19, which produces the point-wise implicit algorithm given in Eq. 20, was crucial for the success of the present method. Local "pseudo" time-stepping and multigrid acceleration techniques were both employed to improve the convergence of the algorithm during every pseudo time step. Details of the multigrid algorithm are given below.

Multigrid acceleration strategy

In this work, we adopted the non-linear full approximation storage scheme of Brandt (1977) in conjunction with the multigrid strategy developed by Jameson (1985) for the solution of the Euler equations to the solution of our governing equations. The Runge–Kutta algorithm (Eq. 19) is used as the basic smoother. A series of successively coarser grids is constructed by doubling the grid spacing in all three spatial coordinate directions, that is, full coarsening (semi-coarsening or doubling the grid in two of the three directions is also possible). Starting with an estimate of the solution on the finest grid, the flow variables are transferred (or restricted) to the coarser grid using injection, that is, a transfer operator $T^s_{2h,h}$ is defined, which picks flow variable at every other point to define the solution on the coarse grid as well as defining the coarser grid itself

$$Q^n_{2h} = T^s_{2h,h} Q_h \tag{21}$$

where the subscripts *h* and 2*h* denote fine- and coarse-grid values, respectively. To ensure that the coarse-grid solution is driven by fine-grid residuals—so that the reduced coarse-grid accuracy does not contaminate the accuracy of the fine-grid solution—the equations solved on the coarse grid are modified by including a forcing term $\wp_{2h}$ defined by Jameson (1985) as

$$\wp_{2h} = T^r_{2h,h} \mathbf{R}_h \left(Q_h \right) - \mathbf{R}_{2h} \left(Q_{2h} \right) \tag{22}$$

where T^r is the residual restriction operator that computes a coarse grid residual by averaging the fine-grid residuals over the 27 nodes that surround every node on the coarse grid. The solution on the coarse grid is then advanced in pseudo time using the Runge–Kutta algorithm of Eq. 20, which for l = 1 to 4 becomes

$$Q^l_{2h} = Q^{l-1}_{2h} + \left(\mathbf{I} + a_l \frac{3}{2} \frac{\Delta t}{\Delta t} \Gamma \right)^{-1} \left[-Q^{l-1}_{2h} + Q^0_{2h} - a_l \Delta t \Im^{-1} \right] \left(\mathbf{R}^{l-1}_{2h} + \wp_{2h} \right) \tag{23}$$

Once the coarsest grid is reached, the accumulated corrections are transferred (or prolonged) back to the finest grid using a series of simple trilinear interpolations on successively finer grids. On highly stretched grids, this interpolation procedure; which is carried out in the transformed, equally spaced, computational domain; may introduce high-frequency errors back to the fine grid and degrade the convergence rate. To eliminate such errors, the corrections on a given coarse

grid are processed through a constant-coefficient, implicit residual smoothing operator before using them to update the solution on the finer grid.

In this work, a three level V-cycle with sub-iterations was used for each pseudo-time step on the fine grid. One iteration was performed on the h grid, two on the $2h$ grid, and three on the $4h$ grid. In LES models, the contribution of the SGS model comes entirely through the eddy viscosity (see Eqs. 7, 8, and 10). The eddy viscosity was calculated on the fine grid only and transferred to the coarser grids using the transfer operator.

4.3 Outflow boundary conditions

One of the main challenges we had to overcome in the course of this study was to develop a mathematical framework for specifying outflow boundary conditions that are numerically robust without distorting the physics of the flow. Note that for the present jet flow, as we move further away from the nozzle, the jet undergoes a series of three-dimensional instabilities (see discussion in §6) and eventually transitions into a fully turbulent flow. However, it is in this fully turbulent region that we must truncate the computational domain and apply outflow boundary conditions. Due to the complexity of the flow in this region, the outflow conditions should be formulated such that they allow very complex vortical structures (eddies) to continuously cross the outflow boundary without causing the build-up of non-physical flow gradients at the exit. Such non-physical gradients, once they form, would invariably propagate upstream, contaminate the numerical solution, and lead to numerical instability. Some of the simpler boundary conditions, commonly used in numerical calculations, which we implemented unsuccessfully, include (1) extrapolating the flow variables (p and u_i) to the boundary and (2) solving a simplified, linear convection equation at the boundary for the velocity components. Other researchers have used a variation of the second technique in their predictions of turbulent jets with some success. Wilson and Demuren (1998) added a buffer layer to the outlet of their computational domain. In this buffer layer, the governing equations were gradually relaxed from the full Navier–Stokes equations to the simple linear convection equation. Although this buffer-layer technique worked well for their case, it has a definite disadvantage in that the size of the buffer layer substantially increases the computer resources required for the simulation (in Wilson and Demuren's calcula-

tion, the increase was 20%). Because of its increased cost and some ambiguities concerning the accuracy of the buffer layer technique for unsteady simulations (Grinstein 1994), we did not attempt to use it.

The outlet boundary conditions used in the present simulation were developed by adopting the characteristics-based approach proposed by Thompson (1990). This approach has been successfully applied in a variety of compressible, viscous flow simulations (Poinsot and Lele 1992; Grinstein 1994) and can be readily adapted to our numerical formulation since we solve the incompressible, filtered Navier-Stokes equations using the artificial compressibility approach (see Eq. 18)—that is, we transform the incompressible equations into a hyperbolic-like system in pseudo-time. The main idea behind this characteristic-based formulation for implementing outflow boundary conditions can be summarized as follows. At the outflow boundary, waves could both enter or exit the computational domain. Outgoing waves need no boundary conditions because they depend only on information from within the computational domain. However, incoming waves require boundary conditions because they transport information from outside of the domain, which, of course, is not available at an outflow boundary. These different types of waves, which are implicitly embedded within the convective terms of the governing equations, can be identified by diagonalizing the convective terms along the direction perpendicular to the outflow boundary (Thompson 1990). Following Thompson (1990), we diagonalize the artificially compressible Navier-Stokes equations to calculate the “amplitude” of these waves (the quantities that would be conserved along each wave for a local one-dimensional approximation of the full equations) and recast the governing equations explicitly in terms of the these amplitudes. Amplitudes corresponding to outgoing waves are directly computed using one-sided backward differencing from the calculated solution in the interior. On the other hand, amplitudes corresponding to incoming waves are set equal to zero to ensure that they do not reflect any information into the computational domain as such information could contaminate the computed solutions. In other words, we treat the outflow boundary as a fully absorbing, albeit one-way, sponge that allows information from within the domain to cross without distortion but absorbs fully any upstream propagating waves.

We present in detail the outlet boundary conditions as follows: we rewrite the governing equations in terms of the characteristic wave amplitudes (Thompson 1990); we apply absolutely non-reflecting boundary conditions at the outlet and thus simplify the boundary condition equations; and we discuss the implementation of these new boundary conditions within the existing numerical method.

Governing equations in characteristic form

By applying the procedure outlined by Thompson (1990), the governing equations (Eq. 18) can be rewritten in Cartesian coordinates as

$$\frac{\partial Q}{\partial t} + \Gamma \frac{\partial Q}{\partial t} + \mathbf{S}\mathcal{L} + H = 0 \tag{24}$$

where Q, t, Γ, t are defined as before, and H is a vector that includes all the x_2 and x_3 derivatives in Eq. 18. The matrix **S** is calculated after considerable algebraic manipulations, involving the diagonalization of the one-dimensional, inviscid approximation of the full three-dimensional equations (Thomson 1990), and it reads as follows:

$$\mathbf{S} = \begin{bmatrix} -bc & bc & 0 & 0 \\ b + l_1 u_1 & b + l_2 u_1 & 0 & 0 \\ l_1 u_2 & l_2 u_2 & 1 & 0 \\ l_1 u_3 & l_2 u_3 & 0 & 1 \end{bmatrix} \tag{25}$$

where the eigenvalues are

$$\begin{aligned} l_1 &= u_1 - c \\ l_2 &= u_1 + c \\ l_3 &= l_4 = u_1 \end{aligned} \tag{26}$$

and where $c = \sqrt{u_1^2 + b}$ and b is the artificial compressibility coefficient, which is a constant of $\mathcal{O}(1)$. The components of the vector $\mathcal{L}$ are the amplitudes of the various waves and are defined as follows:

$$
\begin{aligned}
\mathcal{L}_1 &= \frac{l_1}{2c^2}\left(-\frac{l_2}{b}\frac{\partial P}{\partial x_1}+\frac{\partial u_1}{\partial x_1}\right)\\
\mathcal{L}_2 &= \frac{l_2}{2c^2}\left(-\frac{l_1}{b}\frac{\partial P}{\partial x_1}+\frac{\partial u_1}{\partial x_1}\right)\\
\mathcal{L}_3 &= \frac{l_3}{2c^2}\left[\frac{1}{b}\left(l_2 d_1 + l_1 d_2\right)\frac{\partial P}{\partial x_1}-\left(2c^2+d_5\right)\frac{\partial u_1}{\partial x_1}+2c^2\frac{\partial u_2}{\partial x_1}\right]\\
\mathcal{L}_4 &= \frac{l_4}{2c^2}\left[\frac{1}{b}\left(l_2 d_3 + l_1 d_4\right)\frac{\partial P}{\partial x_1}-\left(2c^2+d_6\right)\frac{\partial u_1}{\partial x_1}+2c^2\frac{\partial u_3}{\partial x_1}\right]
\end{aligned}
\tag{27}
$$

The components of the vector *d* are

$$
\begin{aligned}
d_1 &= -b + l_1\left(u_2-u_1\right)\\
d_2 &= -b + l_2\left(u_2-u_1\right)\\
d_3 &= -b + l_1\left(u_3-u_1\right)\\
d_4 &= -b + l_2\left(u_3-u_1\right)\\
d_5 &= -2b + 2l_3\left(u_2-u_1\right)\\
d_6 &= -2b + 2l_4\left(u_3-u_1\right)
\end{aligned}
\tag{28}
$$

We can expand Eq. 24 by expanding the term $\mathbf{S}\mathcal{L}$ to obtain a set of equations that can be used to define any boundary condition for a x_1 boundary for the incompressible Navier–Stokes equations using the artificial compressibility method.

$$
\begin{aligned}
\frac{\partial P}{\partial t} + bc\left(\mathcal{L}_2-\mathcal{L}_1\right)+H_1 &= 0\\
\frac{\partial u_1}{\partial t}+\frac{\partial u_1}{\partial t}+\left(b+l_1u_1\right)\mathcal{L}_1+\left(b+l_2u_1\right)\mathcal{L}_2+H_2 &= 0\\
\frac{\partial u_2}{\partial t}+\frac{\partial u_2}{\partial t}+\left(l_1\mathcal{L}_1+l_2\mathcal{L}_2\right)u_2+\mathcal{L}_3+H_3 &= 0\\
\frac{\partial u_3}{\partial t}+\frac{\partial u_3}{\partial t}+\left(l_1\mathcal{L}_1+l_2\mathcal{L}_2\right)u_3+\mathcal{L}_4+H_4 &= 0
\end{aligned}
\tag{29}
$$

The only terms from the original governing equations omitted in Eq. 29 are the viscous terms in the x_1 direction. The viscous terms in the other two directions are contained in the components of

H. Now given Eq. 29, we can specify boundary conditions simply by specifying the components of $\mathcal{L}$, which are the only terms involving derivatives in the direction normal to the outflow boundary.

Outlet boundary conditions in terms of the characteristic equations

The components of the eigenvalue vector l give the characteristic speed of each of the waves across the outflow boundary and the corresponding components of the vector $\mathcal{L}$ give the amplitude of these waves. At an outflow boundary, negative eigenvalues are associated with incoming waves and positive eigenvalues are associated with outgoing waves. Boundary conditions are needed for the incoming waves only. Here, we apply an absolutely non-reflecting boundary condition such that no information from outside the domain propagates into the domain; that is, we set the amplitude of all incoming waves to zero. Thus for each *i*, if $l_i < 0$ we set $\mathcal{L}_i = 0$; otherwise, we compute $\mathcal{L}_i$ from Eq. 27 using one-sided, backward finite-difference approximations. From the definition of l in Eq. 26, there are two different cases depending on the sign of u_1, if $u_1 \geq 0$ then only $l_1 < 0$ and we set $\mathcal{L}_1 = 0$ and compute the other components of $\mathcal{L}_i$ using Eq. 27. If $u_1 < 0$, then only $l_2 > 0$ and we set $\mathcal{L}_1 = \mathcal{L}_3 = \mathcal{L}_4 = 0$. The one common result for either case is that $\mathcal{L}_1 = 0$. So we can simplify Eq. 29 to

$$\begin{aligned}
\frac{\partial P}{\partial t} + b\,c\mathcal{L}_2 + H_1 &= 0 \\
\frac{\partial u_1}{\partial t} + \frac{\partial u_1}{\partial t} + \left(b + l_2 u_1\right)\mathcal{L}_2 + H_2 &= 0 \\
\frac{\partial u_2}{\partial t} + \frac{\partial u_2}{\partial t} + l_2\mathcal{L}_2 u_2 + \mathcal{L}_3 + H_3 &= 0 \\
\frac{\partial u_3}{\partial t} + \frac{\partial u_3}{\partial t} + l_2\mathcal{L}_2 u_3 + \mathcal{L}_4 + H_4 &= 0
\end{aligned} \tag{30}$$

These equations are solved for every node on the outlet boundary. In the next section, we discuss the implementation of this boundary condition routine within the present numerical method.

Numerical implementation of the new boundary condition

The boundary conditions are implemented only on the finest grid. The components of H are computed just as the right hand side is computed in the interior of the domain except that all the derivatives in the x_1 direction are neglected. The unsteady terms in Eq. 30 are treated implicitly just as in Eq. 20. The resulting right hand side vector (containing the unsteady terms and the H terms from Eq. 30) is included in the constant coefficient, implicit residual smoothing. The x_1 derivatives that appear in the definition of $\mathcal{L}$ in Eq. 27 are computed with first-order central differencing. Since our original scheme is second-order accurate, according to Poinsot and Lele (1992), using a first-order accurate differences in computing the boundary conditions for the outgoing waves will not reduce the global accuracy of our scheme below second order.

Even though this approach for specifying outflow boundary conditions has not yet been tested extensively, the results contained in this report are promising (see especially §6). In particular, very complex flow structures can continuously cross the outlet boundary with no apparent distortion. Moreover, when the simpler boundary conditions mentioned above were used, numerical instabilities, which caused the computation to "blow-up", grew within 1000 time steps. The current simulation has run for more than 5000 time steps with no stability problems.

4.4 Unsteady particle tracking algorithm

As a first preliminary attempt to analyze the computed unsteady flow field from the standpoint of a fish transported by the flow (that is, examine the computed flow field from the so-called Lagrangian point of view), we developed a method for computing the trajectories of passive fluid particles within an unsteady flow field. By passive particles, we mean particles that are sufficiently small and inert to be simply transported by the local flow without actually modifying the flow. Of course this is a very crude approximation of the three-dimensional fish body and cannot be expected to yield any quantitatively meaningful information about the actual fish trajectories in the laboratory flume. Obviously, real fish are three-dimensional bodies with inertia and will not follow the paths of passive particles. In addition, fish affect the local flow characteristics via the boundary layers that grow around and the vortices that are shed from their bodies. This influence could be considerable given the fact that, as we already discussed, we are interested in

quantifying the impact of “fish-sized” eddies on the fish body, and these are precisely the eddies that will be affected the most by the presence of fish in the flow. Finally, and this has been demonstrated in the PNNL experiments, fish introduced into the shearing zone of the jet tend to flex and undergo a tumbling-like motion, and this deformation will further impact both the local flow and the fish trajectory. In spite of these obvious and rather severe limitations, analyzing the trajectories of passive particles serves to underscore the kind of information that can be extracted from a Lagrangian description of the flow. Therefore, this analysis should provide some, albeit very approximate, understanding of the manner in which a traveling fish experiences the highly unsteady and three-dimensional, turbulent flow environment.

The trajectory of a passive particle can be obtained by integrating the following three ordinary differential equations:

$$\frac{\mathrm{d}x_1}{\mathrm{d}t} = u_1\left(x_1, x_2, x_3, t\right) \quad \frac{\mathrm{d}x_2}{\mathrm{d}t} = u_2\left(x_1, x_2, x_3, t\right) \quad \frac{\mathrm{d}x_3}{\mathrm{d}t} = u_3\left(x_1, x_2, x_3, t\right) \tag{31}$$

where x_i is the i-th coordinate of the particle location, u_i is the i-th component of the flow velocity at the current particle position (obtained from the solution of the governing equations, t is the time, and $i = 1, 2, 3$. We solve this equation using a two-stage, second-order, Runge–Kutta method, which is given as

$$\begin{aligned} a_i &= \Delta t u_i\left(x_i^n, t^n\right) \\ b_i &= \Delta t u_i\left(x_i^n + a_i, t^n + \Delta t\right) \\ x_i^{n+1} &= x_i^n + \frac{1}{2}\left(a_i + b_i\right) \end{aligned} \tag{32}$$

where n is the present time level and $n + 1$ is the new time level. Refer to Darmofal and Haimes (1996) for a detailed discussion of this and other higher-order methods for integrating Eq. 31. The time step Δt cannot be greater than the time step in our LES computation, which provides the velocity u_i at discrete points in time. We chose the time step in Eq. 32 to be equal to that of our LES computation, and we have encountered no stability problems to date.

Our LES computation provides the velocity of the fluid at discrete spatial locations, which are defined by the computational grid. Since the numerical method for solving the LES equations

requires storing the velocity field at two time instants (n and n - 1), no temporal interpolation is necessary. Therefore, to solve Eq. 32 we need only interpolate in space to find the velocity of the fluid particle. However, before the particle velocity can be determined, the particle must be located within the computational grid. We use a search algorithm that is based on a triple-cross-product technique. For each grid cell, we construct six pairs of vectors $\vec{e}_j$ and $\vec{f}_j$ for j = 1…6 defined by the diagonals of each one of the six faces of a given quadrilateral cell. For every cell face, that is, for every vector pair $\left(\vec{e}_j, \vec{f}_j\right)$, we construct a third vector $\vec{h}_j$ defined by the particle location and center point of the cell face. The particle resides within the computational cell in which all six cross products, $\vec{e}_j \times \vec{f}_j \times \vec{h}_j$, have the same sign. Once the particle is located with the computational grid, the particle velocity is determined using trilinear interpolation (Murman and Powell 1989).

5. Problem Description and Comparison with PNNL Experimental Data

In this section, we present comparisons between our computations and the PNNL experimental measurements. In §5.1, we describe the geometry of the problem, the computational mesh, and various numerical details of the simulations; in §5.2, we describe the inlet velocity profile; and in §5.3, we compare the predictions of the LES model with the mean velocity and turbulence statistics measured by PNNL.

5.1 Geometry, computational mesh, and numerical details

The flow under consideration is generated by a circular nozzle issuing into a quiescent reservoir at Reynolds numbers in the turbulent flow regime. In the PNNL flume, a pipe for introducing fish into the flow was also included right above the nozzle (see Neitzel et al. 2000, for a detailed description of the geometry). In the present calculations, however, we omitted the fish-injection pipe because of the increased computational resources that would be required to perform a LES for such a complex geometry. The simplified computational geometry is shown in Fig. 4 together with a computed iso-surface of constant mean axial velocity of u = 0.1, which illustrates the spreading and overall extent of the jet.

Simulations were performed at Reynolds numbers of 100,000 and 300,000. The Reynolds number is defined as $\left(Re = Ud/\nu\right)$ where U is the mean velocity of the jet, d is the diameter of the nozzle exit, and ν is the kinematic viscosity of the jet fluid. All lengths in the simulations were made non-dimensional with respect to the jet diameter d and all velocities with respect to the jet velocity U.

Computational meshes

For the Re = 100,000 case, the computational domain was a cube with nominal dimensions of $10d \times 10d \times 10d$. The circular jet was centered at (0,0,0). The y and z axes extended from $-5d$ to $5d$; the x axis extended from 0 to $10d$. The computational mesh is shown in Fig. 5. Fig. 5(a) shows a x-z plane, and Fig. 5(b) shows a y-z plane together with the location of the jet entrance.

The size of the computational grid was 89 × 121 × 121 in the *x*, *y*, and *z* directions, respectively (approximately 1.3×10^6 nodes). The nodes in the *x* direction were uniformly distributed giving a streamwise grid spacing of $\Delta x = 0.1087$. The nodes in the *y* and *z* directions were uniformly distributed within a $6d \times 6d$ square centered around the axis, $\Delta y = \Delta z = 0.133\overline{3}$, in the core region of the jet. In the outer region near the side walls, the grid nodes were distributed using a hyperbolic tangential stretching function. The extent of the refined core region of the grid was carefully chosen to include as much of the developing shear layer as possible over the whole length of the computational domain, since this is the region where much of the complex flow occurs within the jet. The time step was 0.025 in non-dimensional time units.

In the *Re* = 300,000 simulation, the computational domain was $10d \times 6d \times 6d$. The *x* axis extended from 0 to 10*d*; the *y* and *z* axes extended from -3*d* to 3*d*. The size of the computational grid was 201 × 121 × 121 in the *x*, *y*, and *z* directions for a total of more than 2.9×10^6 nodes. The nodes in each spatial direction were uniformly distributed to give a grid spacing of $\Delta x = \Delta y = \Delta z = 0.05$. The time step was $\Delta t = 0.0125$. Therefore, the grid and time step used in the *Re* = 300,000 provided more than twice the spatial resolution and exactly twice the temporal resolution of the *Re* = 100,000 simulation.

For reference to the PNNL experiments, the fish used in the experiments varied in length from 8.5 to 21 cm. The jet diameter in the PNNL experiment was 6.35 cm. Thus, in these terms, the fish were between 1.3 and 3.4 diameters long. In the simulations, time is non-dimensionalized by the jet diameter and jet velocity. For the Re = 100,000 case using the 10 ft/s experiment as reference, one dimensional time unit corresponds to 0.020 s. Thus, a time step of 0.025 equals 0.00052 s. The computational mesh corresponds to 7.0 mm in the axial direction and 8.5 mm in the transverse directions. For the *Re* = 300,000 simulation using the 20 ft/s experiment as reference, a non-dimensional time unit corresponds to 0.010 s, and a time step of 0.015 equals 0.00015 s. The grid spacing corresponds to 3.2 mm.

Numerical details

The boundary conditions were the same for both Reynolds number simulations. On the side boundaries of the computational domain, first-order extrapolation was used for the pressure, and the velocity components were set equal to zero. The pressure was fixed at one point in the center of the outlet boundary. The outlet boundary conditions were applied as described in §4.3. In both simulations, the residual smoothing coefficients were 1.0 in all directions. The CFL, von Neumann, and artificial compressibility coefficients were all set to 1.0. The convergence of the inner iterations of the dual time stepping scheme was carefully monitored. In general, an inner iteration was declared converged after the average residual for all three velocity components had decreased by more than 2 orders of magnitude. Typically, such a reduction occurred within 20 iterations.

The Re = 100,000 simulation was started on a computational grid one-half as dense in the cross-sectional directions (89 × 61 × 61), and the flow field in the reservoir was initially at rest. The simulation was run on the coarser grid for approximately 1000 time steps before the solution was transferred to the 1.3-million node grid and run for another 2000 time steps. The actual Re = 100,000 simulation began (the time at which we began storing solutions) after a total of 3000 time steps.

The initial solution for the Re = 300,000 simulation was obtained by interpolating the Re = 100,000 solution (after 4000 time steps) from the the 1.3-million node grid to the 2.9-million node grid. Initially, the Re = 300,000 simluation ran for approximately 4000 time steps to allow errors created by interpolation and any other transients to exit the domain. This amount of time was also enough to allow the mean velocities and turbulence statistics (e.g., the Reynolds stresses) to statistically converge. The convergence was confirmed by montioring the running average of the turbulence statistics at various points in the flow field as the solution progressed.

In terms of computer resources, the Re = 300,000 simulation required three times the memory and more than three times the wall clock time for one time step compared to the Re = 100,000 simulation.

5.2 Inlet conditions

The inlet velocity profile specified in the present simulations was selected to meet two criteria: (1) to represent as closely as possible the flow at the exit of the nozzle in the PNNL experiments; and (2) to ensure that the three-dimensional instabilities of the jet that lead to transition to turbulence grow within a relatively short simulated time interval, thus, avoiding excessive computational times. The first criterion was met by using a mean velocity profile obtained by fitting the experimental measurements at the exit of the nozzle. The second criterion was met by forcing the jet, that is, imposing on the mean profile a small, time-periodic perturbation at one of the fundamental frequencies of the flow. By exciting this particular frequency, the initially axisymmetric jet shear-layer becomes unstable to azimuthal disturbances and transitions to turbulence much faster than would otherwise occur in an unforced jet, thus, significantly reducing the overall computational time. The imposed forcing could be thought as representing at least some of the disturbance modes that are bound to be present in the laboratory flume, say, due to small vibrations of the piping system. The effect of this particular forcing on the turbulence statistics in the simulated jet is investigated in the §5.3.

The inlet velocity profile varies with radius r and time t. The profile is given by the general formula

$$u(r,t) = u^*(r)\left[1 + A\sin(2p\, ft)\right] \tag{33}$$

where u^* is a top-hat-like velocity profile given by

$$u^*(r) = \frac{1}{2}\left\{1 + \tanh\left[\frac{1}{8q}\left(\frac{1}{2r} - 2r\right)\right]\right\} \tag{34}$$

In the above equations, A is the amplitude of the imposed forcing, f is the frequency of the forcing, t is time, r is the radial distance measured from the center of the jet, and q is the momentum thickness of the boundary layer for this velocity profile. In this study, the amplitude of the forcing was chosen to be 0.04 or 4 % of the mean jet velocity. The frequency of the forcing was chosen as 0.4 (Grinstein et al. 1996). The momentum thickness of the boundary layer q was adjusted to fit the measured velocity profile. The success of this fit is shown in Fig. 6 in the pro-

file denoted by $x = 0.0$. The momentum thickness that gives this agreement was found to be $q = 0.005$.

5.3 Comparison of predictions and measurements

The PNNL experiments were conducted in an outdoor flume measuring 9 m long × 1.2 m wide × 1.2 m deep. The jet was produced through a nozzle whose diameter narrowed from 25.4 cm to 6.35 cm. The nozzle extended 50 cm into the tank, and the centerline of the nozzle exit was located 50 cm from the bottom of the tank. The nozzle was roughly centered between the side walls of the tank. Laser Doppler velocimetry (LDV) measurements taken as part of the PNNL study are available for a variety of *Re* from approximately 180,000 to 900,000, which correspond to mean jet velocities of 10 to 70 ft/s. We compare the *Re* = 100,000 simulation to the 10-ft/s jet (*Re* = 180,000) and the *Re* = 300,000 simulation to the 20-ft/s jet (*Re* = 350,000).

The notation used in this report is slightly different from that used in the PNNL final report (Neitzel et al. 2000). In that report, the axial direction of the jet was called the *z* direction with corresponding velocity component *u*. The cross-sectional directions were called *x* and *y* with velocity components *v* and *w*, respectively. In this report as shown in Fig. 4, the axial direction of the jet is called the *x* direction with corresponding velocity component *u*. The cross-sectional directions are called *y* and *z* with velocity components *v* and *w*, respectively.

Re = 100,000 case

The LES of the jet flow produces a sequence of instantaneous snapshots of the turbulent flow field. To compare the *Re* = 100,000 simulation with the mean velocity measurements, we ran the numerical simulation for 4400 time steps (a non-dimensional time interval $t = 110$), stored instantaneous solutions every 25 time steps (this storage frequency was dictated by the available computer disk storage capacity), and averaged the resulting sequence. The simulated time interval appears to be sufficiently long for obtaining satisfactory results for the mean flow although these results may be not entirely converged in a statistical sense.

Fig. 6 compares the time-averaged LES predictions of the axial velocity *u* to the measured axial velocity reported by Neitzel et al. (2000) in the PNNL study. Overall, the computed mean

axial velocity profiles are in excellent agreement with the measurements. Some small discrepancies are observed between $1d < x < 2d$, where the experimental profiles appear to spread somewhat faster than the simulated profiles. However, at $x = 5d$, the predictions and experiments practically coincide with each other. We suspect that these discrepancies could be due to the presence of the fish injection tube in the experiment, which has not been accounted for in the numerical simulation and should certainly be expected to affect the flow in the vicinity of the nozzle. Increased levels of turbulent mixing due to vortices shed by the surface of this tube could, for example, account for the faster spreading rate of the jet in the laboratory experiment. Another possibility for this discrepancy could be the lack of detailed measurements at the exit of the nozzle, which would allow us to prescribe more realistic inflow conditions. For instance in the laboratory, the nozzle is mounted at the exit of a 180-degree pipe bend and, thus, the flow at the exit of the nozzle could exhibit some three-dimensionality due to residual secondary motion generated within the upstream bend. Even though such three-dimensional effects may be small, they could greatly impact the growth of the jet in the near field. It is well known in the literature that the presence of even rather weak longitudinal vortices at the exit of the nozzle could affect the near-field characteristics of the jet by inducing very complex three-dimensional instability modes (Gutmark and Grinstein 1999). Given these uncertainties, we consider the level of agreement between experiments and simulations shown in Fig. 6 to be very satisfactory—especially since it is obvious that the effect of these uncertainties has practically disappeared five diameters downstream of the nozzle.

Fig. 7 shows comparisons for the cross-sectional components of the velocity field, v and w. The predicted and experimental profiles are in reasonable agreement in some areas of the flow, but significant discrepancies are observed in other areas. For instance, notice that the experiments reveal the presence of a considerable negative v-component (almost 10% of the axial flow) just downstream of the nozzle within the core region of the jet ($x = 0.0d$). Although small negative v velocities should be expected and indeed are measured at the edge of shear layer, where the jet entrains fluid from the stagnant flow, it is not clear why such a significant vertical velocity component would exist within the core of the jet so close to the nozzle. A possible explanation, which is also consistent with our previous discussion, is that residual secondary motion from the

upstream bend persists at the exit of the nozzle in the experiment. Since sufficient experimental information was not reported at the inlet (such as velocity measurements across the entire nozzle cross-section), in the computations we set both v and w components equal to zero—which could of course account for some of the observed discrepancies. At the outer edge of the shear layer, where, as we discussed above, stagnant fluid is entrained into the core of the jet, both experiments and simulations predict a small negative component of v, at least for $x < 5d$. The comparisons for the v profile at the $x = 5d$ are especially troublesome, especially in light of the very good agreement between the axial velocity profiles at that section (see Fig. 6). The measured v component appears to be almost unchanged as compared to its upstream levels and this is indeed curious since, as also indicated by the measured axial velocities, the jet has started spreading considerably at this location and one would expect a significant vertical velocity component to be present—such a trend is indeed observed in the calculations.

The mean w component of the velocity should be equal to zero everywhere on this plane if the mean flow field is azimuthally symmetric. The calculations indeed yield a zero mean value for w almost everywhere except the $x = 5d$ section where very small levels of w are computed. Note that at this section the jet is fully turbulent and we suspect that the calculated time-averages may not have fully converged in a statistical sense (see also Fig. 8). The measurements once again exhibit persistent small levels of w throughout, starting even from the $x = 0.$ section. We should recognize, however, that both v and w velocity components in this flow are very small compared to the axial component of velocity and, thus, especially difficult to accurately measure using LDV. Other reasons for the observed discrepancies could include the differences in the Reynolds numbers (180,000 in the experiment versus 100,000 in the calculation) and, as discussed above, the presence of the fish-injection tube in the flow field.

Re = 300,000 case

The $Re = 300{,}000$ simulation is compared with the 20-ft/s jet experiment ($Re = 350{,}000$) from the PNNL study. As an extension to the comparisons that were presented for the $Re = 100{,}000$ case, comparisons of the turbulence statistics are presented in addition to the mean velocity components. For the $Re = 300{,}000$ case, we focused the comparisons on the region downstream of

the nozzle exit. In the following after looking at the comparison between the simulated and experimental jets, we further discuss the issue of inlet conditions in the experiments and the simulations in detail.

The mean velocity components and turbulence statistics were calculated by saving the entire flow field and eddy viscosity every 25 time steps for more than 5500 time steps for a total of 220 independent realizations of the instantaneous flow field. To compute turbulence statistics, the instantaneous velocity at a given point $\tilde{u}$ (this occurs for each velocity component) is decomponsed into a mean part u and a fluctuating part u', that is, $\tilde{u} = u + u'$. The turbulence normal stresses are calculated by taking the time average of the product of the instantaneous fluctuations, for example, $\langle u'u' \rangle$ where the brackets < > indicate a time average. The turbulence shear stresses are calculated by taking the time average of the product of the fluctuations of two different velocity components, for example, $\langle u'v' \rangle$. The turbulence normal stresses are often presented in root-mean-squared form $u_{rms} = \sqrt{\langle u'u' \rangle}$ and in that case are called the turbulence intensity. The turbulence kinetic energy is the sum of the turbulence normal stresses and is calculated as

$$k = \frac{1}{2}\sqrt{\langle u'u' \rangle + \langle v'v' \rangle + \langle w'w' \rangle} \tag{35}$$

The comparisons between the *Re* = 300,000 predictions and the PNNL experimental measurements for the 20-ft/s jet are presented in Figs. 8–11. Fig. 8 shows the three components of the mean velocity. Fig. 9 shows the turbulence normal stresses as the root-mean-squared turbulence intensity of each velocity component. Fig. 10 shows the turbulence kinetic energy, and Fig. 11 shows the only significant component of the turbulence shear stress $\langle u'v' \rangle$. Each of these figures contains a radial profile of the given quantity at three axial locations: $x = 2d$, $5d$, and $10d$.

Refering to Fig. 8, the overall agreement between mean velocity profiles in the computations and the experiments is satisfactory. Considering u at $x = 2.0d$, the experimental jet spread faster than the simulated jet in the region very near the nozzle; thus the higher u velocity in the region $y > 0.5$. Further into to turbulent region, however, the simulated jet spread faster than the experimental one with the two jets having nearly the same profile at $x = 5d$. The centerline velocity in the simulated jet is lower in the simulation than the experiment at $x = 0$. Also from Fig. 8, the two other velocity components are much smaller in magnitude than the axial component and

nearly zero—especially in the turbulent region ($x = 10d$) for both the simulated and experimental jet, which is the expected behavior for an axisymmetric jet. The simulated jet at $x = 2d$ shows a v velocity directed radially outward in the core region of the jet ($y < 0.5d$), and this effect is more pronounced although still small at $x = 5d$. This effect is likely due to the mode-four stucture caused by the rectangular computational domain. This mode-four structure was repeatedly seen in the lower Re = 100,000 jet (see for example Fig. 26) and is also present in the Re = 300,000 jet albeit to a lesser extent (see §7).

Figs. 9–11 show that there are clear differences between the turbulence statistics in the simulated and experimental jets in the region near the nozzle. The profiles of the individual components of the turbulence intensity at the $x = 2d$ cross sections in Fig. 9 show that the turbulence energy is distributed differently in the two jets with the simulated jet having all of the turbulence energy in the u and v components; whereas, the experimental jet has the turbulence energy is evenly distributed among each component. Also note that the total turbulence energy k is roughly the same in the two jets at this cross section (see Fig. 10, $x = 2.0$). Moving further away from the nozzle, the turbulence statistics (including the distribution of the turbulence energy) become much more similar in the two jets, and in the fully turbulent region (that is, at $x = 10d$, Figs. 9-11) all of the components of the Reynolds stresses are in remarkable agreement including the turbulence shear stress $\langle u'v' \rangle$.

The different distributions of the turbulence energy in the simulated and the experimental jet can be attributed to the different levels of turbulence in the two jets at the nozzle exit. In the simulated jet, there is no turbulence at the nozzle exit (see §5.2 for details). A small axial forcing at one frequency is added at the inlet of the simulated jet to shorten zone over which the jet transitions to turbulence (and thus shorten the required length of the computational domain). The simulated jet needed to transition to turbulence as fast as possible to match the experimental jet, because in the PNNL experiments the flow was already turbulent when it exited the nozzle. The experimental flow was consistent with a thin, turbulent boundary layer with a large, thin peak of turbulence kinetic energy located at the edge of the jet. As this thin turbulent boundary layer exited the nozzle, more turbulence energy was produced. These turbulent fluctuations were at least partly responsible for the faster spreading of the experimental jet (see Fig. 8). As a result, more

energy is present in the shear layer. This same process occurs in the simulated jet only further away from the nozzle because before it can begin, the jet must transition to turbulence, which occurs in the first couple of diameters downstream of the nozzle exit for the Re = 300,000 simulation.

We should note that designing a simulation and experiment to match at the level of the turbulence statistics in the region very near the nozzle is not a trival task. At a minimum, this requires very detailed measurements over the entire cross section of the nozzle exit. These measurements should contain enough information to allow the calculation of turbulence spectra for all components of the Reynolds stress tensor. Moveover, frequency spectra of the time-varying velocity signals would be needed to show any significant vibrations that might be present in the experimental apparatus.

Using this experimental information, two possibilities exist for designing a *turbulent* inlet condition for the jet simulation. These two possibilities are discussed in detail by Lund et al. (1998) for turbulent boundary layer simulations. One possibility is to use randomly generated velocitiy fields that are scaled to produce Reynolds stresses equivalent to those measured in the experiments. Although this approach would meet the goal of providing a turbulent flow for the inlet of the simulation, this approach still requires a significant development length before a 'true' turbulent flow develops (Lund et al. 1998) because the random velocity fields still lack much of the information characteristic of a true turbulent flow. In particular, the velocity fields are uncorrelated and lack the structure of a turbulent flow. The second possibility for designing a turbulent inlet condition is to perform an additional LES calculation of an incoming turbulent boundary layer and to chose a plane of experimental data based on the thickness of the incoming boundary layer measured in the experiment. Such a parallel simulation method would be require significantly more computational resources although these resources can be mitigated somewhat by recycling the inlet data from the separate simulation after a sufficient length of time (Li et al. 2000). Either of the above two possibilities requires that the flow exiting the nozzle is axisymmetric in the mean. If the flow happens to be nonaxisymmetric, then performing a separate LES to produce a nonaxisymmetric inlet would require significant resources that would be equivalent to performing a LES of the interior of the entire nozzle—a very difficult and expensive task.

So although the inlet conditions that were used in the simulations were the most practical and most realistic given the lack of a complete description of the nozzle exit conditions in the PNNL experiments, one can ask whether or not the forcing used in the experiments makes the jets too different to make comparisons useful. However, if we refer again to the comparison of the turbulence statistics in Figs. 9-11, although very near the nozzle exit the turbulence statistics in the two jets are not consistent (as would be expected); this inconsistency is no longer present in the fully turbulent region (see for example, $x = 10d$ in Figs. 9, 10). This fact confirms that the forcing frequency in the simulated jet does not affect the flow in the fully turbulent region.

As a prelude to the next section, we show in Fig. 12 the time-averaged axial velocity field for the $Re = 100{,}000$ simulation at cross sections through the jet corresponding to the constant x locations shown in Figs. 6 and 7. As seen in this figure, the mean velocity field essentially retains the basic characteristics of a circular axisymmetric jet spreading radially up until $x = 5d$. At this station, the velocity contours suggest the growth of very complex instability modes that lead to the observed lateral, mushroom-like contour patterns—the nature of these instabilities and the evolution of the jet beyond this section are discussed in the next section.

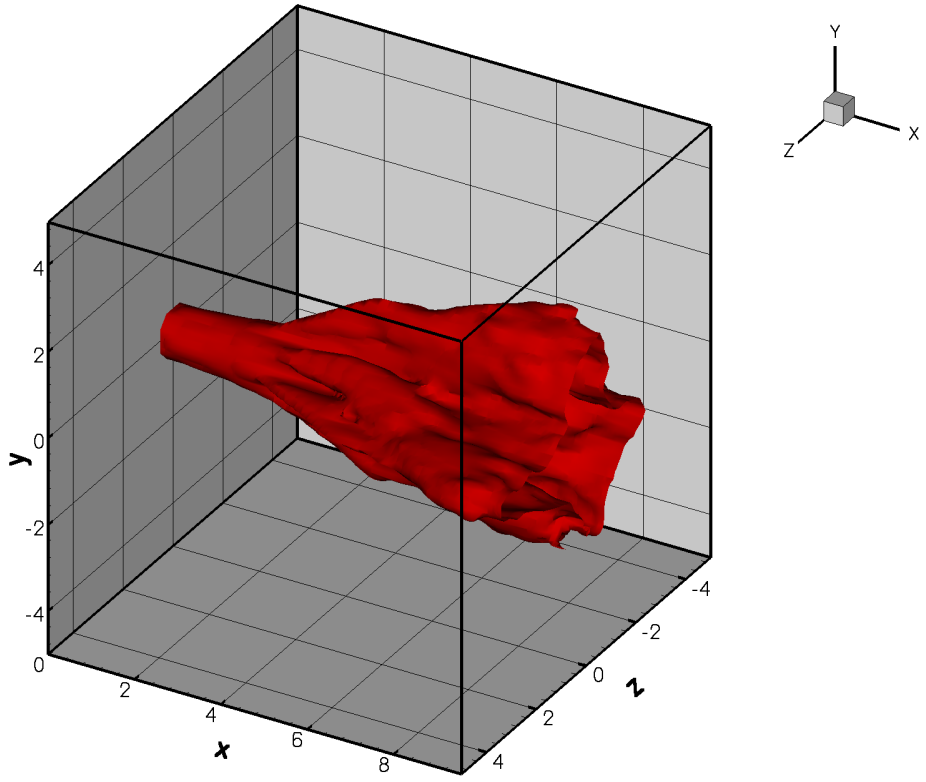

Figure 4. The computational domain for the circular jet flow along with a calculated iso-surface of the time-averaged velocity (u = 0.1), which serves to illustrate the overall structure of the jet flow field.

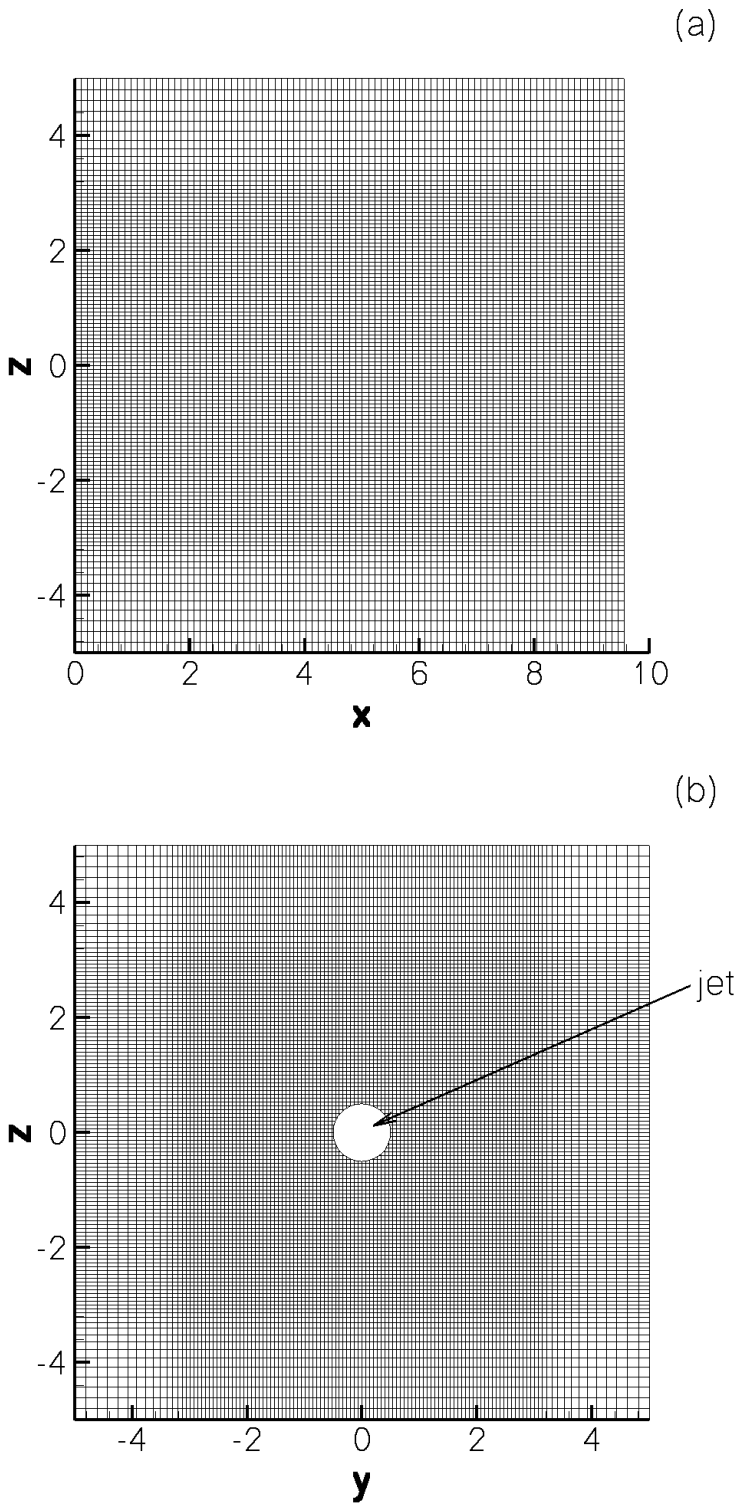

Figure 5. Typical cross sections of the computational mesh on the *x*-*z* and *y*-*z* planes.

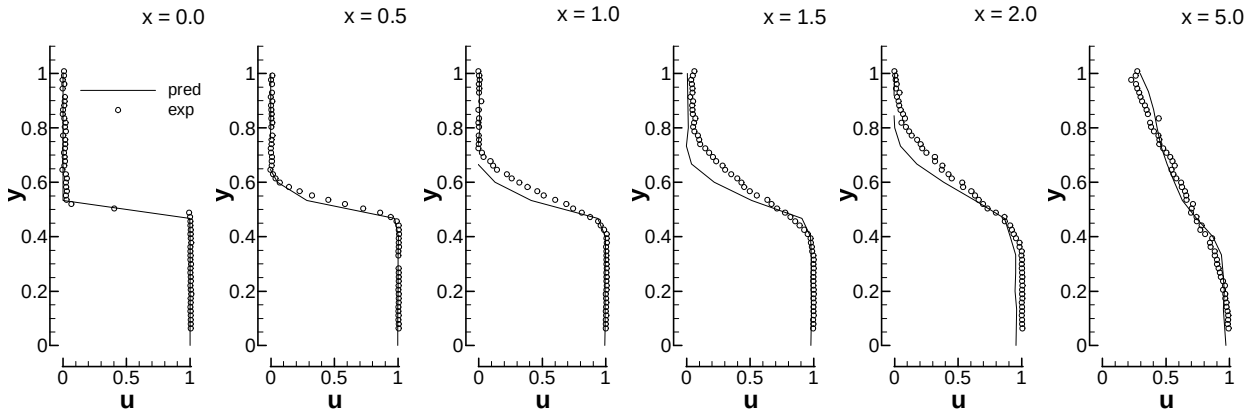

Figure 6. Comparison between the PNNL measurements (symbols) and the computational results (lines) for the time-averaged velocity *u* profiles on the $z = 0$ symmetry plane.

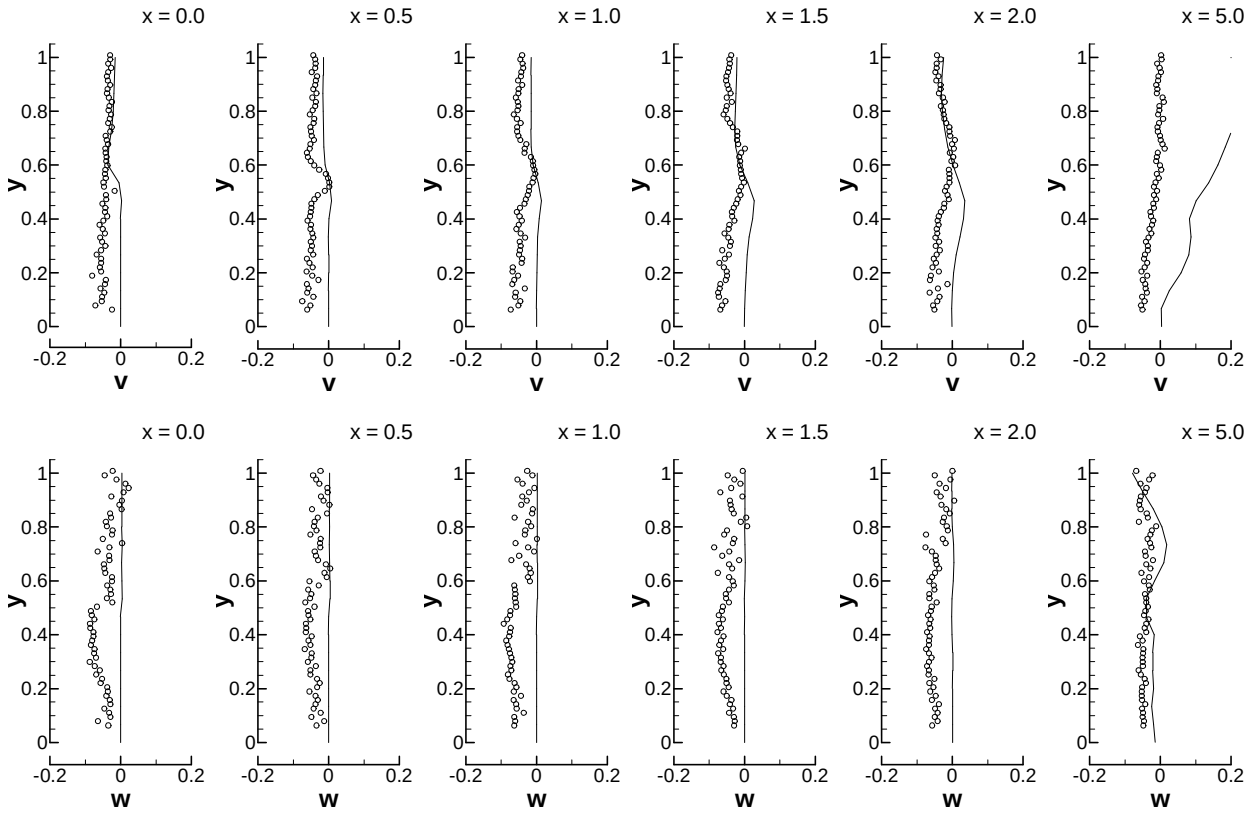

Figure 7. Comparison between the PNNL measurements (symbols) and computational results (lines) for the time-averaged *v* and *w* velocity profiles on the $z = 0$ symmetry plane.

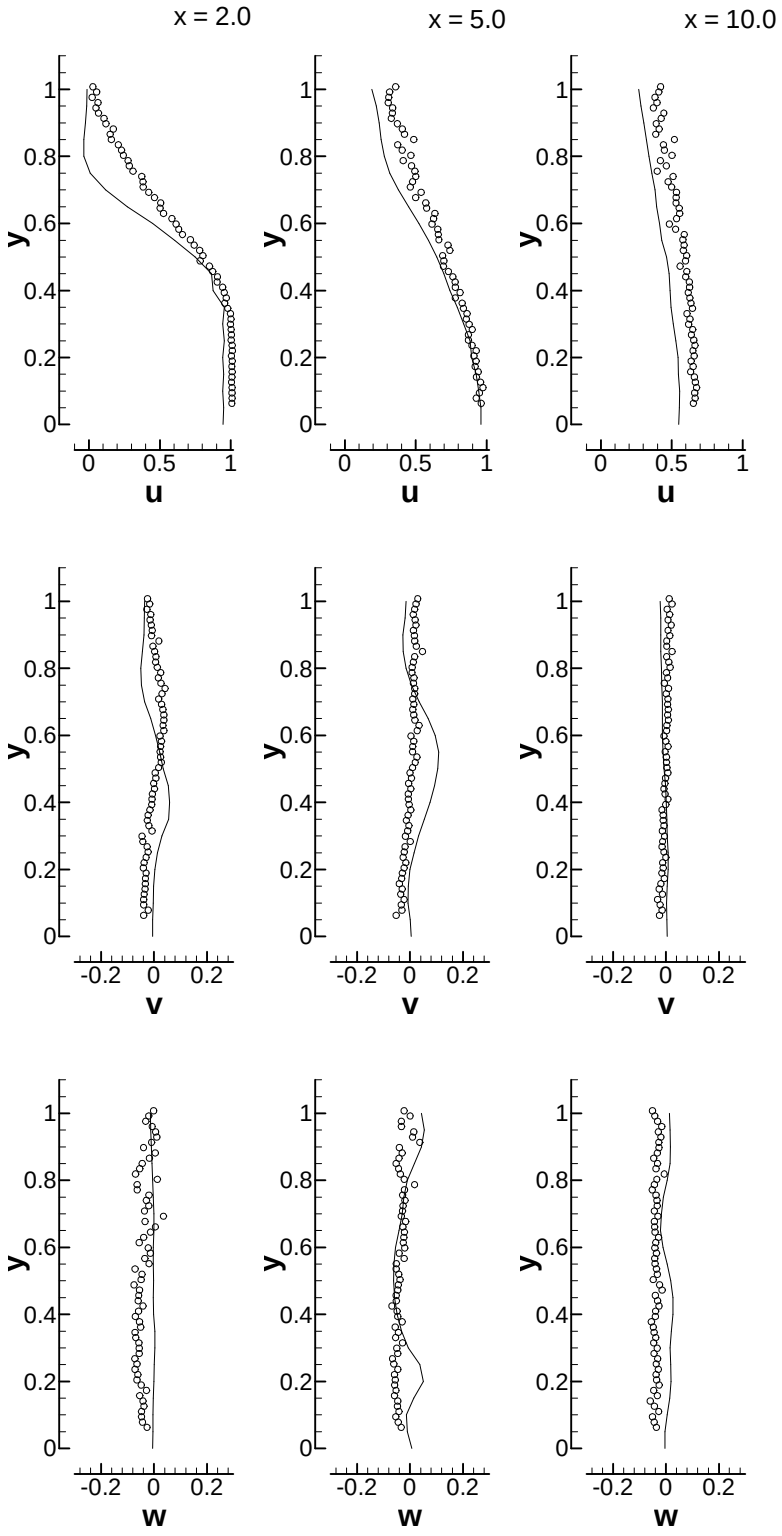

Figure 8. Comparison of the PNNL measurements (symbols) and the LES predictions (lines) for the mean velocity components.

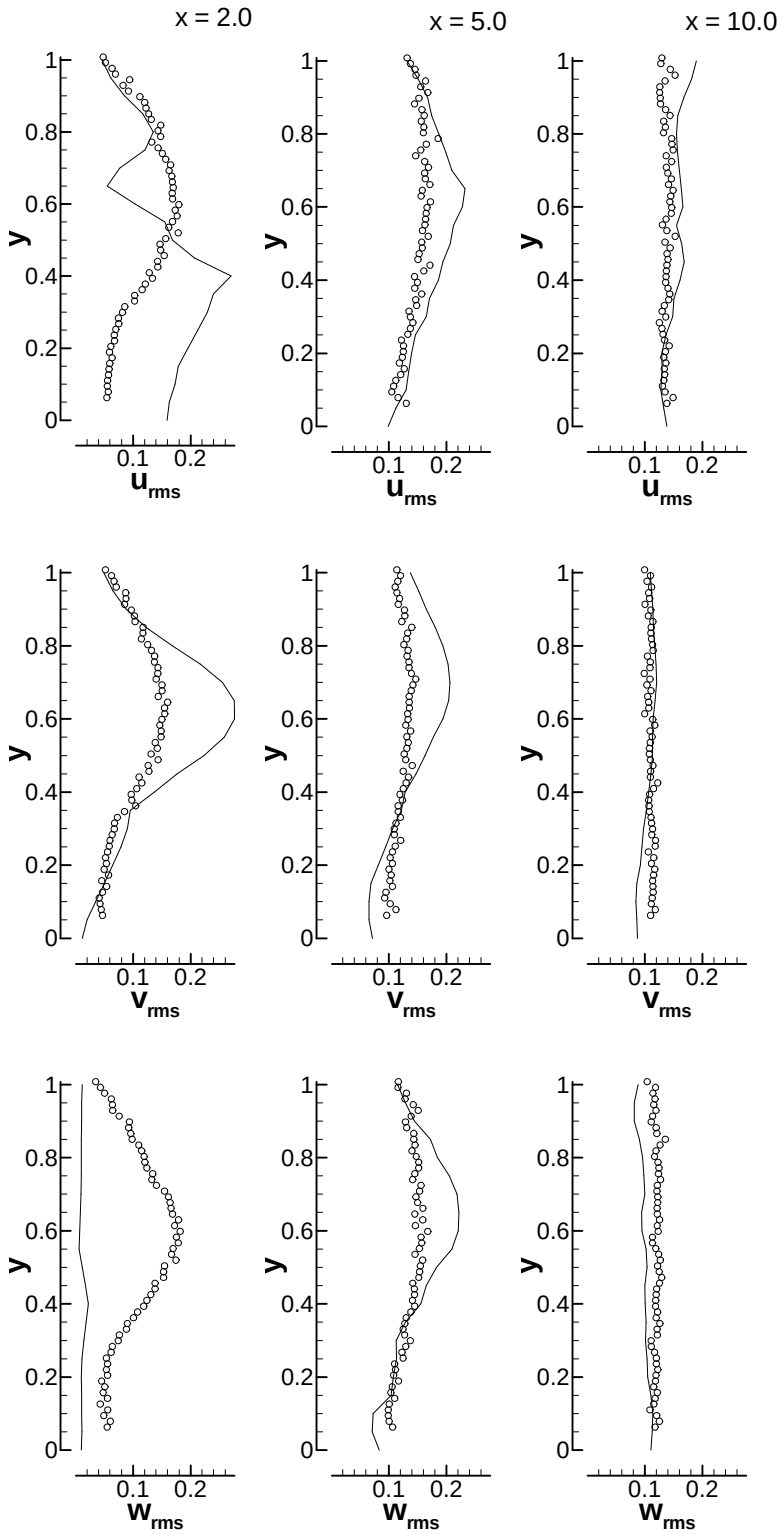

Figure 9. Comparison of the PNNL measurements (symbols) and the LES predictions (lines) of the individual components of the root-mean-squared turbulent velocity fluctuations.

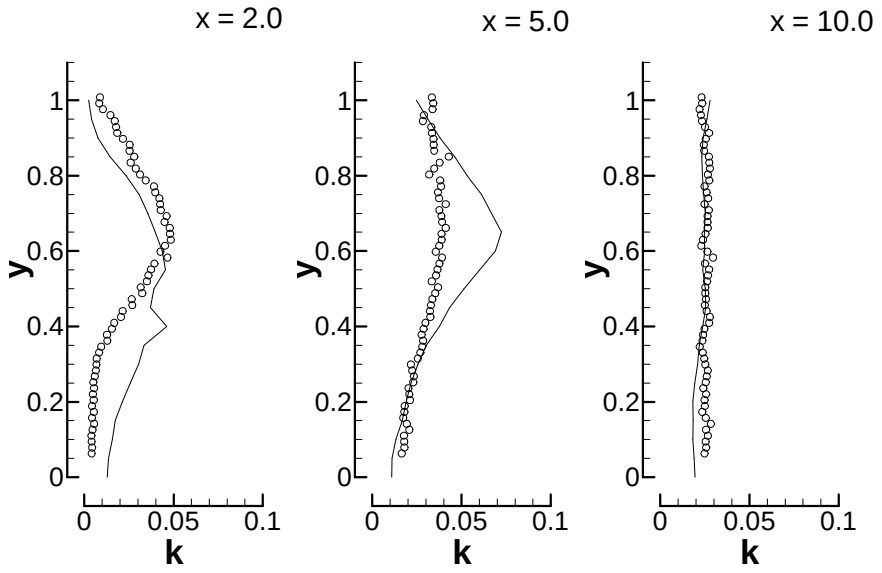

Figure 10. Comparison of the PNNL measurements (symbols) and the LES predictions (lines) of the turbulent kinetic energy *k*.

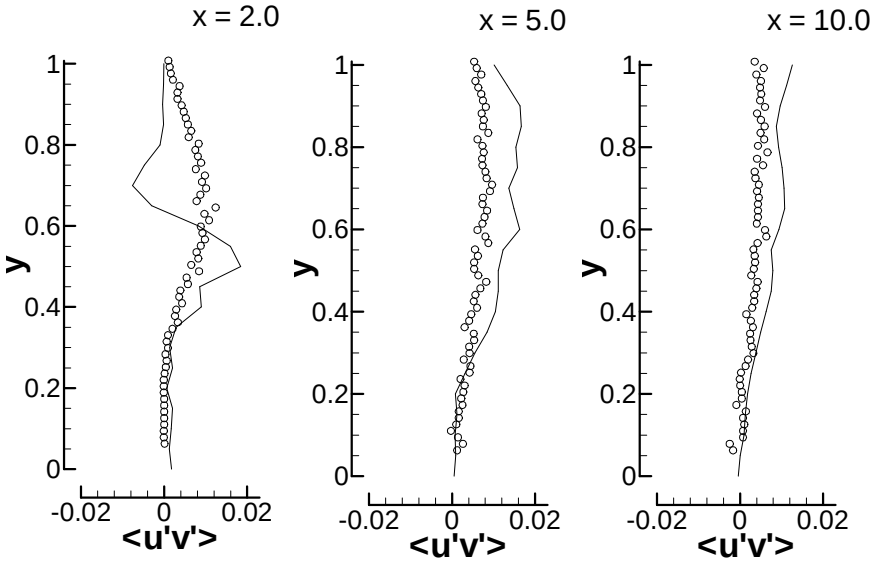

Figure 11. Comparison of the PNNL measurements (symbols) and the LES predictions (lines) of the mean turbulence shear stress $\langle u'v' \rangle$.

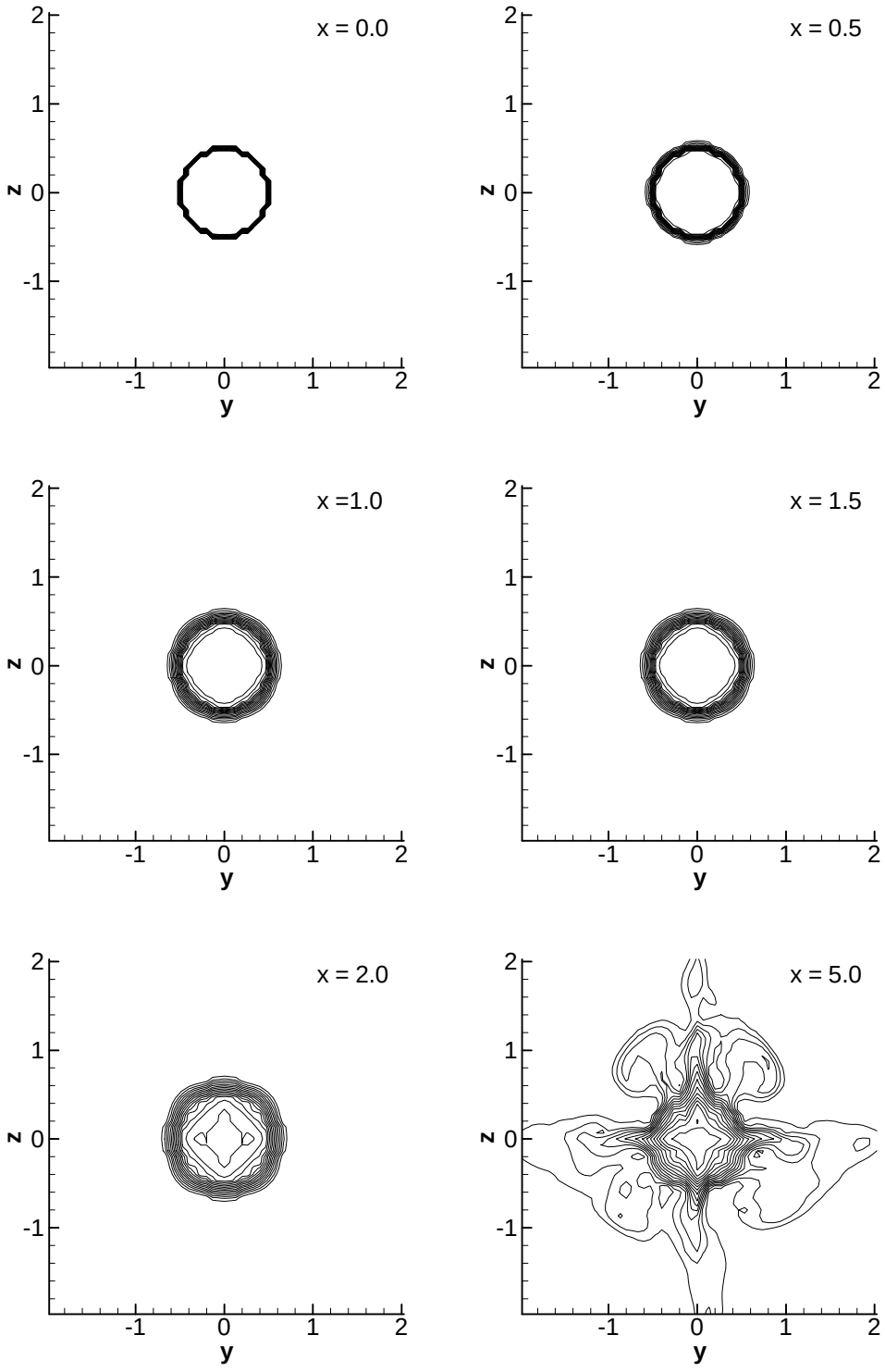

Figure 12. Calculated contours of time-averaged axial velocity at the same *x* locations shown in the Figs. 6 and 7. The plot shows 15 equally spaced contours levels between 0.1 and 0.95.

6. Analysis of the Instantaneous Flow Field

In this section, we analyze in detail the complex temporal and spatial variations of the computed flow field and juxtapose the instantaneous and time-averaged descriptions of the flow. As we have already discussed above, fish introduced into the flow never experience the time-averaged flow but are rather exposed to a very complex turbulent environment that varies randomly both in space and in time. Therefore, our objective is twofold: (1) to quantify the extent to which the instantaneous flow could vary from the mean; and (2) to demonstrate the need for understanding the structure of this instantaneous flow, at least at scales comparable to the fish size, to be able to interpret in a meaningful way injury and mortality events observed in the laboratory. In this section, we make the comparisons of instantaneous and time-averaged flow fields using the *Re* = 100,000 simulation. In §7, we compare the instantaneous flow fields at the two Reynolds numbers.

In addition to visualizing the flow in terms of the predicted velocity components (*u*, *v*, *w*), we also compute several quantities whose magnitude is proportional to the various flow-induced forces acting on a fish. The computed quantities that are used in the following analysis are: (1) the magnitude of the pressure gradient $\left(|\nabla P|\right)$, which quantifies pressure-induced forces that could compress, stretch or possibly bend the fish; (2) the vorticity given by the magnitude of the vorticity vector $\left(|\Omega|\right)$ and the axial component of vorticity $\left(\Omega_x\right)$, which quantify the rate of spinning a fish may experience and, thus, dizziness and disorientation effects; and (3) the magnitude of the strain-rate tensor $\left(|S|\right)$, which quantifies the intensity of shearing forces—see the earlier discussion in §2. Complete definitions for each of these quantities in Cartesian coordinates are as follows:

$$|\nabla p| = \left[\left(\frac{\partial p}{\partial x}\right)^2 + \left(\frac{\partial p}{\partial y}\right)^2 + \left(\frac{\partial p}{\partial z}\right)^2\right]^{\frac{1}{2}} \tag{1}$$

$$|\Omega| = \left(\Omega_x^2 + \Omega_y^2 + \Omega_z^2\right)^{\frac{1}{2}} \tag{2}$$

where

$$\Omega_x = \frac{\partial w}{\partial y} - \frac{\partial v}{\partial z}; \quad \Omega_y = \frac{\partial u}{\partial z} - \frac{\partial w}{\partial x}; \quad \Omega_z = \frac{\partial u}{\partial y} - \frac{\partial v}{\partial x} \tag{3}$$

$$|S| = \left\{ 2\left[\left(\frac{\partial u}{\partial x} \right)^2 + \left(\frac{\partial v}{\partial y} \right)^2 + \left(\frac{\partial w}{\partial z} \right)^2 \right] + \frac{1}{2}\left[\left(\frac{\partial u}{\partial y} + \frac{\partial v}{\partial x} \right)^2 + \left(\frac{\partial u}{\partial z} + \frac{\partial w}{\partial x} \right)^2 + \left(\frac{\partial v}{\partial z} + \frac{\partial w}{\partial y} \right)^2 \right] \right\}^{\frac{1}{2}} \tag{4}$$

Figs. 13 and 14 depict the calculated time histories of selected quantities at two points in the flow: one very near the jet inlet (x = 0.5d) and the other in the middle of the computational domain (x = 5.0d). The various quantities shown in these figures have been normalized with their respective mean values to readily quantify the deviation of the instantaneous value from the mean. For example, the normalized velocity magnitude $|\mathbf{u}|^*$ is computed as

$$|\mathbf{u}|^* = \frac{|\mathbf{u}|}{|\bar{\mathbf{u}}|} \tag{5}$$

where the velocity magnitude is computed as

$$\mathbf{u} = \left(u^2 + v^2 + w^2 \right)^{\frac{1}{2}} \tag{6}$$

The other normalized quantities are computed in a similar manner.

Fig. 13 shows the normalized velocity magnitude, pressure gradient, vorticity magnitude, and strain rate very close to the inlet of the jet. Since the inlet flow is forced (see §5.2), it is no surprise that in the immediate vicinity of the inlet the calculated flow quantities oscillate in time in a periodic manner. The velocity and pressure fluctuate between ±20% of the mean and the vorticity and the strain rate fluctuate at ±10% and ±5%, respectively. Note that the fluctuation of the velocity is already 5 times greater than the forcing of the inlet velocity profile, which was only 4%. That is, the imposed inlet perturbation is amplified very rapidly downstream of the nozzle. In fact, it is the very rapid growth of this disturbance that triggers the transition to turbulence within a very short simulated time interval—recall that the reason that this perturbation was imposed in the first place was to produce turbulent flow without having to run the simulation for an excessively long time. Fig. 14 shows signals of the same quantities at a point in the middle of the flow domain where the flow has transitioned to turbulence. In stark contrast with the regular periodic signals of Fig. 13, the signals at this point exhibit clear characteristics of a chaotic

turbulent flow. Note that there is no longer any readily apparent correlation with the imposed inlet forcing as all quantities fluctuate randomly and by as much as 200% above their mean values. It is also worth noting from Fig. 14 that the time record of each quantity appears uncorrelated with the others, even though both the vorticity and strain rate are computed by differentiating the velocity field—a feature that underscores the different flow processes expressed by the vorticity vector and the strain-rate tensor. Note also that these time histories have a spacing of $25\Delta t$, which means that smaller temporal-scale fluctuations are present in our simulation, but these are not included in the results presented here.

Figs. 15-18 show instantaneous profiles of the axial velocity (Figs. 15 and 17) and the vorticity magnitude (Figs. 16 and 18) on y = constant or z = constant planes for six different x locations. These figures also show the time-averaged profile with a thick black line. Like the time histories in Fig. 14, these figures are very revealing as they quantify the extent to which the instantaneous flow field differs from the time-average flow field. The axial velocity profiles shown in Figs. 15 and 17 show that the flow essentially remains laminar up to approximately 3 diameters downstream of the nozzle. Random velocity fluctuations begin to grow at approximately $x = 4d$ primarily near the edge of the shear zone of the jet while the core of the jet remains laminar and nearly steady. The fact that temporal fluctuations originate within the shear layer is to be expected since turbulence is produced and sustained by the presence of mean shear. Furthermore, shear-layer instabilities are known to be one of the primary mechanisms that causes transition to turbulence in jet flows. As seen in Figs. 15 and 16, the intensity of the velocity fluctuations grow rapidly and spread toward the core region of the jet with increasing distance from the nozzle. A fully turbulent flow, in which any trace of the inlet periodic forcing has completely disappeared, is established within six diameters. The vorticity magnitude profiles shown in Figs. 16 and 18 exhibit the same overall qualitative characteristics as the velocity profiles but significant quantitative differences are clearly evident. The intense vorticity fluctuations that appear within the shear layer begin closer to the nozzle as compared to the velocity profiles—note that small vorticity fluctuations are evident even at the $x = 2.5d$ profile. Most importantly, the overall intensity of the vorticity fluctuations about the mean is significantly higher than those of the axial velocity component throughout the jet. In fact, there are several profiles where the instantaneous vorticity

values are almost an order of magnitude larger than the mean value—these trends are consistent with the general features of turbulent flows, which are characterized by very intense vorticity fluctuations. It is important to emphasize that Figs. 15 to 18 clearly show why consideration of the instantaneous flow field is extremely important for meaningful interpretation of the injury, disorientation, and mortality records obtained from laboratory experiments. Clearly the flow environment encountered by the fish is far more complicated and could be considerably more or considerably less hazardous than the mean flow suggests.

The profiles in Figs. 15–18 also allow us to evaluate (by comparing the top and bottom profile for each x location) the symmetry of the time-averaged jet flow field, which we would expect to be symmetric with respect to the axis. As seen, the velocity profiles are symmetric for most of the x locations shown here, but the vorticity profiles are overall less symmetric than the velocity profiles. This should be attributed to the fact that, as we already discussed above, we have not carried out the computation for sufficiently long times to establish a statistically converged time-averaged flow.

Figs. 19-22 examine the flow field in terms of contours of the instantaneous axial velocity, the pressure gradient, vorticity magnitude, and strain rate on the $y = 0$ plane. In each figure, we show four snapshots in time separated by $1000\Delta t$. The axial velocity plots shown in Fig. 19 reveal that the so-called potential region of the jet (the high-velocity core) remains rather stable in time for $x < 4$. The forcing we impose at the inlet is clearly visible in this region as pockets of increased axial velocity travel continuously and in a regular manner from the inlet to the interior along this potential core. Further downstream, however, the potential core undergoes a flapping-like instability as it breaks up into turbulence and appears to wander about the axis in a seemingly random manner—video animations illustrate this feature very clearly. The flow outside of this potential core becomes very complex, both spatially and temporally, at approximately $x > 3d$—this is consistent with the growth of temporal velocity fluctuations within the shear layer in the previously discussed set of figures. The imposed forcing was designed to excite the most unstable modes of the shear layer and causes it to transition to turbulence very near the nozzle. The outer flow is characterized by intense fluctuations and exhibits a highly intermittent behavior, an unmistakable signature of a turbulent flow. Notice for instance that patches of very low

(almost stagnant) axial velocity appear and disappear randomly in this outer region of the jet. As we will show subsequently, this very complex spatio-temporal behavior results in the formation of pockets of very high levels of instantaneous shear in this region (see Fig. 22).

The instantaneous pressure gradient shown in Fig. 20 reveals overall milder temporal variations as compared to the other quantities examined. A series of ring-like structures of high pressure gradient travel continuously from the nozzle into the interior of the flow. These rings mark low pressure regions associated with the donut-like vortices (smoke rings) that are shed as the jet exits the nozzles and roll up to form vortical structures (Fig. 2). Due to the rapid variations in axial velocity, rings are deformed in a non-linear manner, catch up with rings that originated at earlier times, pair together, and engage in very complex interactions. At approximately 4 diameters downstream of the jet (where transition to a fully turbulent flow occurs), the large-scale rings break up into smaller scale structures, and the pressure gradient field starts varying in a very complex manner.

The vorticity magnitude contours shown in Fig. 21 further clarify some of the flow features suggested by the pressure gradient variations. The two red “tongues” of very high vorticity levels emanating from the nozzle mark the initially coherent shear layer of the jet. This shear layer becomes wavy and starts shedding large-scale, donut-like vortices in a regular manner. Each new ring is transported by the axial flow but is also affected by its own self-induced velocity and the velocities induced by rings shed at earlier times. As a result a very complex interaction ensues. Vortex rings tilt forward, pair with rings that were shed earlier, and eventually break up into smaller scale structures. These fundamental instabilities and complex, non-linear interactions, revealed both by the pressure gradient and vorticity fields, are among the primary mechanisms via which the jet transitions into a turbulence. It is also worth noting in Fig. 21 that pockets of very high vorticity levels—equal to and even more intense than those occurring in the shear zone immediately downstream of the nozzle—appear randomly throughout the flow field in an erratic and very intermittent fashion.

The contours of strain-rate magnitude in Fig. 22 are as revealing as those of the vorticity field. Overall they exhibit similar patterns and suggest, as one would expect, the persistence of a very intense shear zone in the immediate vicinity of the nozzle (extending approximately two di-

ameters). Further downstream, however, the strain-rate field becomes very complex and pockets of very high levels of shear (even considerably higher than in the vicinity of the nozzle) appear in a random manner throughout the flow field. A very interesting feature readily apparent in Fig. 22 is that the spatial extent of these pockets of high strain-rate is often comparable to the jet diameter. That is, the spatial scale of these structures is well within the range of what we would call fish-sized eddies and can, thus, inflict serious damage to fish that happen to be there at the instant in time when they form. In fact, Fig. 22 explains the reason for the very consistent mortality results observed in the PNNL experiments. Fish were introduced within the shear zone immediately downstream of the nozzle, which is seen to be very stable in time for almost two diameters downstream. Therefore, most such fish were likely to be exposed consistently to very high levels of shear and, thus, suffer serious injury. Moreover, in this region, the jet bulk velocity is an appropriate parameter to quantify the intensity of the shear zone and, thus, can be used as the parameter to correlate the flow field with observed biological effects. Further downstream, however, the picture that emerges from the simulations is far more complex, and fish that either somehow survived the near-nozzle region or were introduced downstream of the nozzle would be very likely to exhibit far more erratic and unpredictable biological effects. In fact, given the spatial and temporal complexity of the flow in this region, it is unlikely that a single mean flow parameter (like the jet velocity) could be used to correlate the biological effects with the flow field. We should emphasize that the region of the flow further downstream of the nozzle should be far more representative of the turbulent flow environment encountered by fish within the hydropower plant than the near-nozzle, which is a relatively steady region of the jet.

Incidentally, Figs. 19-22 also show the success of the outlet boundary condition described in §4.3. In particular, the complicated flow structures that arise near the outlet boundary in the turbulent region of the jet are transported outside of the computational domain without causing any apparent disturbance to the calculated flow field.

The spatial and temporal variations of the jet in cross-sectional slices normal to the x axis are illustrated in Figs. 23–34. These figures are grouped in pairs, with the first figure in each pair showing an instantaneous quantity and the second figure showing the corresponding time-averaged distributions of the same quantity. For example, Fig. 23 shows contours of axial veloc-

ity for several different cross sections through the jet at one instant in time (t = 30), and Fig. 24 shows the same axial velocity contours at the same cross sections for the time-averaged flow field. In the following, we discuss each of these figures, which, in addition to the axial velocity contours (Figs. 23, 24), include transverse velocity vectors (Figs. 25, 26), pressure gradient (Figs. 27, 28), vorticity magnitude (Figs. 29, 30), strain rate (Figs. 31, 32), and axial vorticity (Figs. 33, 34).

Looking at all of these figures together show several distinct trends. First, note that the large-scale features of the flow in the potential core (up until $x = 4.0d$) are roughly the same in both the instantaneous and time-averaged flow fields. This is consistent with the previous findings that turbulent fluctuations begin to grow first near the edge of the shear layer. Another important feature of the flow, which is present in almost all quantities examined, is the growth of transverse instabilities in the jet cross-section that lead to the formation of very complex, mushroom- and spike-like lateral injections of the flow from the potential core to the outer flow. These instabilities, which are clearly visible up to $x < 4.0d$, are large-scale features of the flow and for that reason are present both in the instantaneous and mean flow fields. As we have already discussed, the growth of such lateral injections is a well established flow feature and has been previously reported in the literature as flow visualization experiments of circular jet flows in which azimuthal non-uniformities are present at the exit of the nozzle. That is, any imperfections of the nozzle or the overall experimental apparatus will lead to the emergence of lateral injections. The precise structure (mushroom-like structures or spike-like injections) and spatial mode (that is the number of these azimuthal structures) depends on the Reynolds number of the flow and the azimuthal non-uniformities that are present at the exit of the nozzle. In fact, experiments have shown that by appropriately perturbing the inlet flow, any number of such structures could emerge (Lasheras and Prestridge 1997). In our numerical computations, we observe the growth of four pairs of mushroom/spike injections along the circumference of the jet. The preference of the computed flow to this mode-four instability is the result of the computational grid we employ, which due to its Cartesian topology introduces a mode-four disturbance into the flow. Note, however, that this mesh-imposed mode affects the flow near the nozzle, but its effect almost disappears completely when transition to turbulence occurs.

Another rather striking feature of the flow, one that may seem counter-intuitive when thinking about the jet from the time-average standpoint, is the existence of very intense secondary (transverse) flow throughout the flow domain. The transverse velocity vector plots shown in Figs. 25 and 26, show that near the nozzle the lateral, spike-like, instability modes we discussed above lead to strong injections of the flow from the potential core radially outward along the *y* and *z* axes. The mushroom structures shown in the contour plots of various quantities in the same region, on the other hand, are seen to entrain flow from the outer region into the potential core. Further downstream, the secondary velocity field becomes extremely complex and consists of several very intense eddies. In fact, the velocity vector plots provide perhaps the most visually striking evidence yet that establishes the inadequacy of the time average flow insofar as understanding biological effects is concerned. Compare for instance the instantaneous with the mean transverse velocity vectors at any section $x > 5d$. The former exhibit very intense and very complex secondary motion patterns while the latter yield essentially zero secondary velocities.

The same overall features are also present in the contour plots of axial vorticity (Figs. 33, 34), which quantifies the intensity of the transverse secondary motion. Note that the growth of axial vorticity component and its interaction with the circumferential vorticity component (concentrated along the circumference of the donut-like vortices we have discussed before) is thought to be among the leading mechanisms leading to transition to turbulence in circular jets (Martin and Meiburg 1996). The comparisons between the instantaneous and mean axial vorticity distributions at any section $x > 5d$ are indeed stunning. The instantaneous Ω_x field reveals that very intense, clockwise $(\Omega_x < 0)$ and counter-clockwise $(\Omega_x > 0)$ longitudinal vortices persist throughout the domain all the way to the exit boundary. Yet, the time-averaged axial vorticity field suggests that, in the mean, vorticity generated near the exit of the nozzle (due the large scale lateral instabilities discussed before) decays rapidly and essentially disappears for $x > 5d$.

Longitudinal vortices in the flow would tend to rotate and bend passing fish and could possibly lead to severe disorientation. If we were to attempt to estimate this biological effect from the mean flow field, we would obviously conclude that only in the immediate vicinity of the nozzle disorientation may be an issue of concern. Yet it is obvious from the results discussed above that such a conclusion could not be further removed from the real situation. Fish would

pass through the instantaneous flow and, thus, experience random spinning and deformation in all three directions, which could frequently reach very high and potentially hazardous levels. Similar conclusions can also be derived from the distributions of the strain-rate tensor magnitude shown in Figs. 31 and 32. In the mean flow field, this quantity decays rapidly with distance from the nozzle. In the instantaneous flow, on the other hand, rather extensive patches of very high strain rate (as high as or even higher than its maximum value in the shear zone just downstream of the nozzle) form randomly throughout the flow domain.

The figures discussed thus far have provided us with a comprehensive understanding of the complexity of the instantaneous flow and an appreciation of the stark contrast between the actual flow environment experienced by fish and the rather simple and seemingly innocuous (except for the few diameters downstream of the nozzle) time-averaged flow. To further underscore the differences between mean and instantaneous flow, we show in Figs. 35–38 iso-surface plots of the total and axial vorticity. In both figures, we juxtapose an instantaneous snapshot of the iso-surfaces with the calculated mean structure. As seen, the instantaneous flow field is characterized by large- and small-scale vortical structures that occur intermittently in regions of the jet where no structures exist at all in the mean flow. This feature is illustrated much clearer in video animations we have created using the calculated flow fields. We should also note, once again, the striking differences between the instantaneous and mean iso-surfaces of axial vorticity. In the mean flow, longitudinal, rib-like vortices are found only within $2d < x < 4d$, while in the instantaneous flow such structures occur across the entire length and in regions where the mean axial vorticity is practically equal to zero.

To conclude this section, we should re-iterate the primary conclusion suggested by our computations and flow analysis. Namely, a fish swimming through the instantaneous flow field will experience; interact with; and be disorientated, injured, or even killed by a flow environment that is vastly different than the time-averaged flow. The only exception to this general conclusion is perhaps the region near the nozzle, where the flow remains reasonably laminar and, thus, mean flow measurements and computations should yield an accurate description of the flow environment. Within a few diameters downstream of the nozzle, however, transition to turbulence occurs and the actual flow becomes extremely complicated. Regions of shear as intense as (or even

stronger than) those occurring within the shear zone near the nozzle should be expected to occur randomly in space and time throughout the flow domain. Strong vortices, and in particular, intense longitudinal structures are found even in regions where the mean flow exhibits very little vorticity. In other words, the mean flow field could be used to correlate biological effects with the flow properties in the vicinity of the nozzle, but further downstream its usefulness is rather limited. A comprehensive understanding of the instantaneous flow field and its statistics at the scale of the fish is essential for interpreting the results of present and guiding the design of future laboratory experiments with real fish.

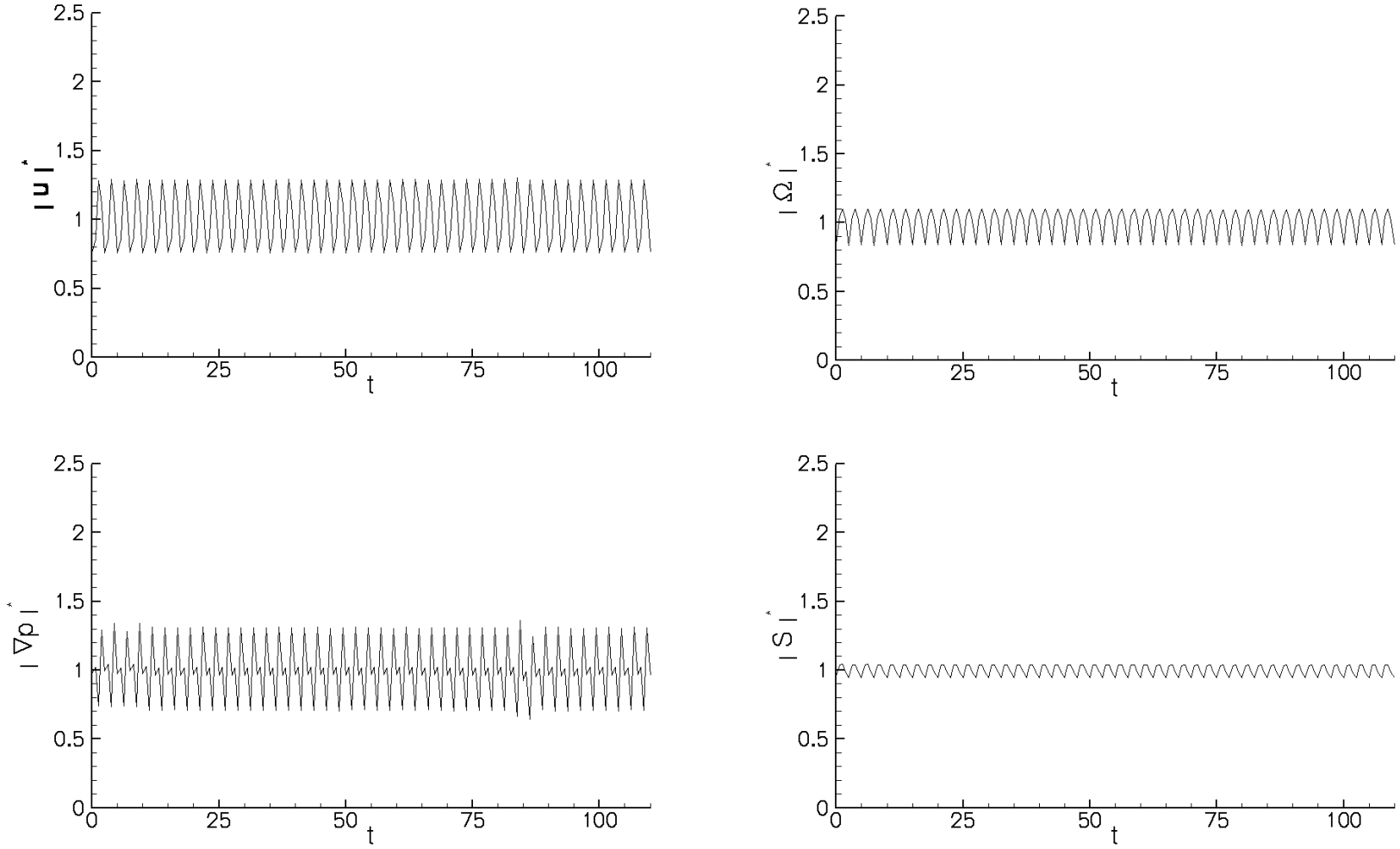

Figure 13. Calculated time histories of the normalized velocity magnitude $|\mathbf{u}|^*$, vorticity magnitude $|\Omega|^*$, pressure gradient $|\nabla P|^*$, and the strain-rate $|S|^*$ at $x = 0.5$, $y = 0.5$, $z = 0.0$.

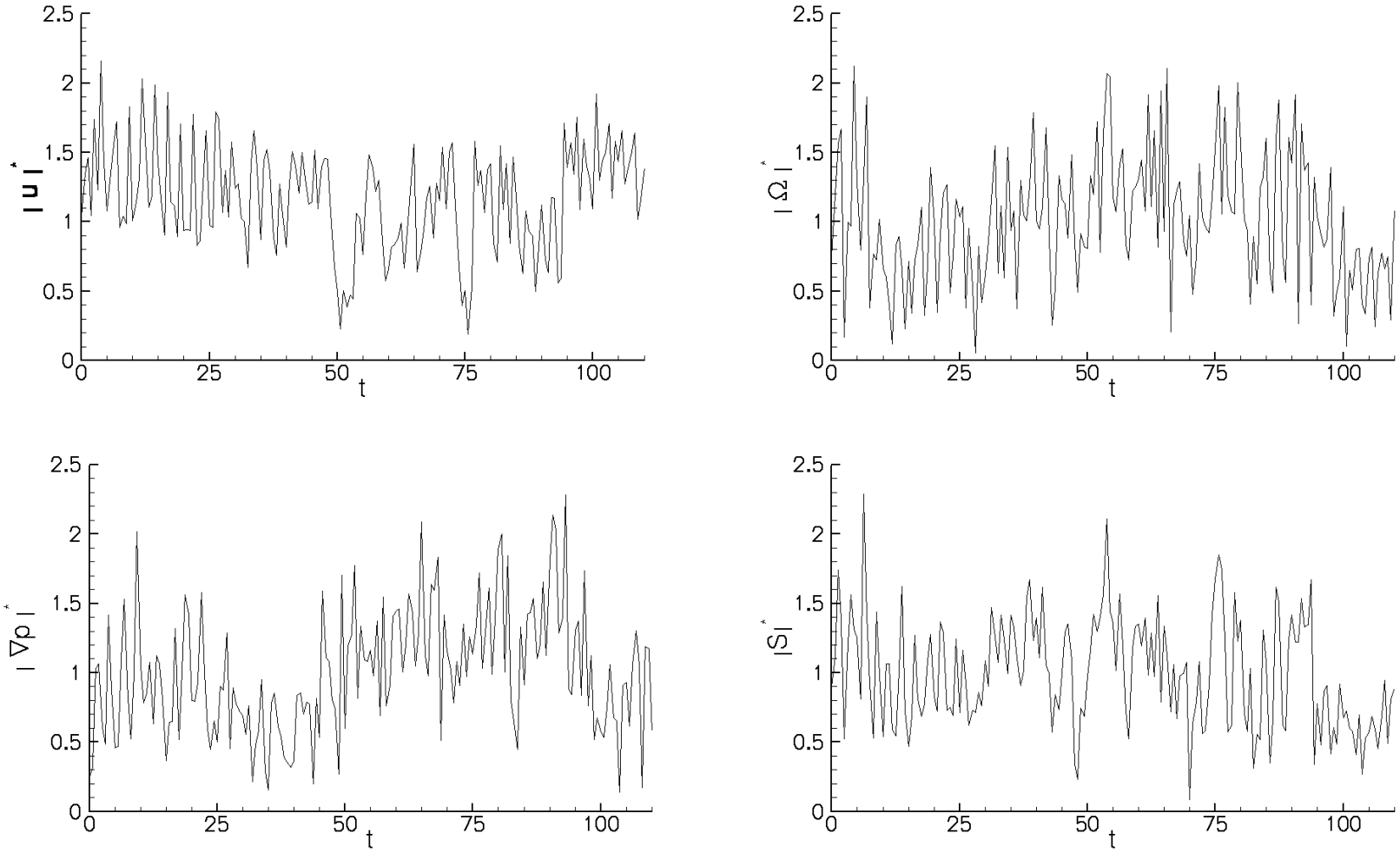

Figure 14. Calculated time histories of the normalized velocity magnitude $|\mathbf{u}|^*$, vorticity magnitude $|\boldsymbol{\Omega}|^*$, pressure gradient $|\nabla P|^*$, and the strain-rate $|S|^*$ at $x = 5.0$, $y = 0.5$, $z = 0.0$.

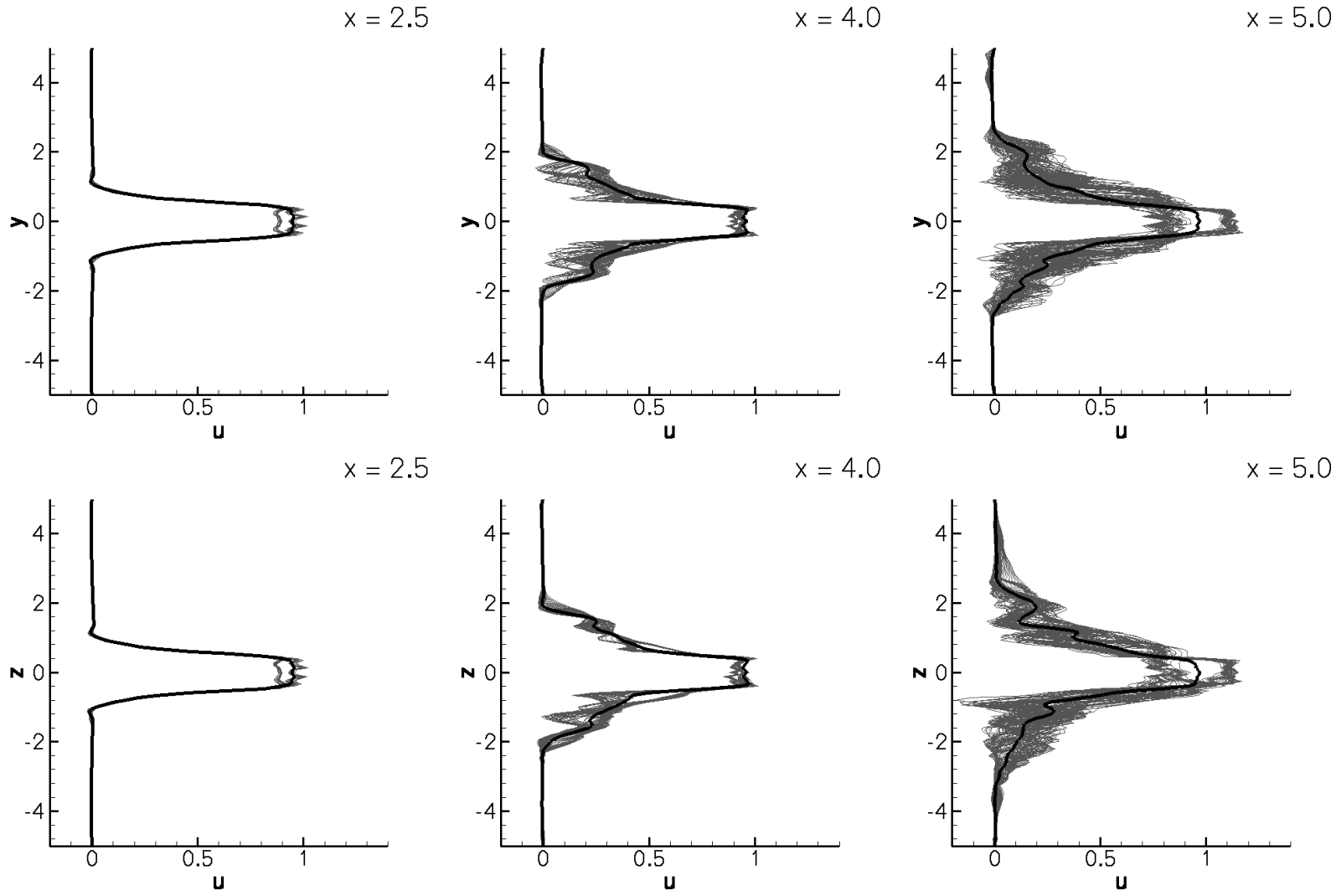

Figure 15. Profiles of the axial velocity near the jet inlet. The thick black lines are the time-averaged profiles. The thin gray lines are instantaneous profiles spaced 50 time steps apart. The *y* profiles are on the *z* = constant plane and likewise for the *z* profiles.

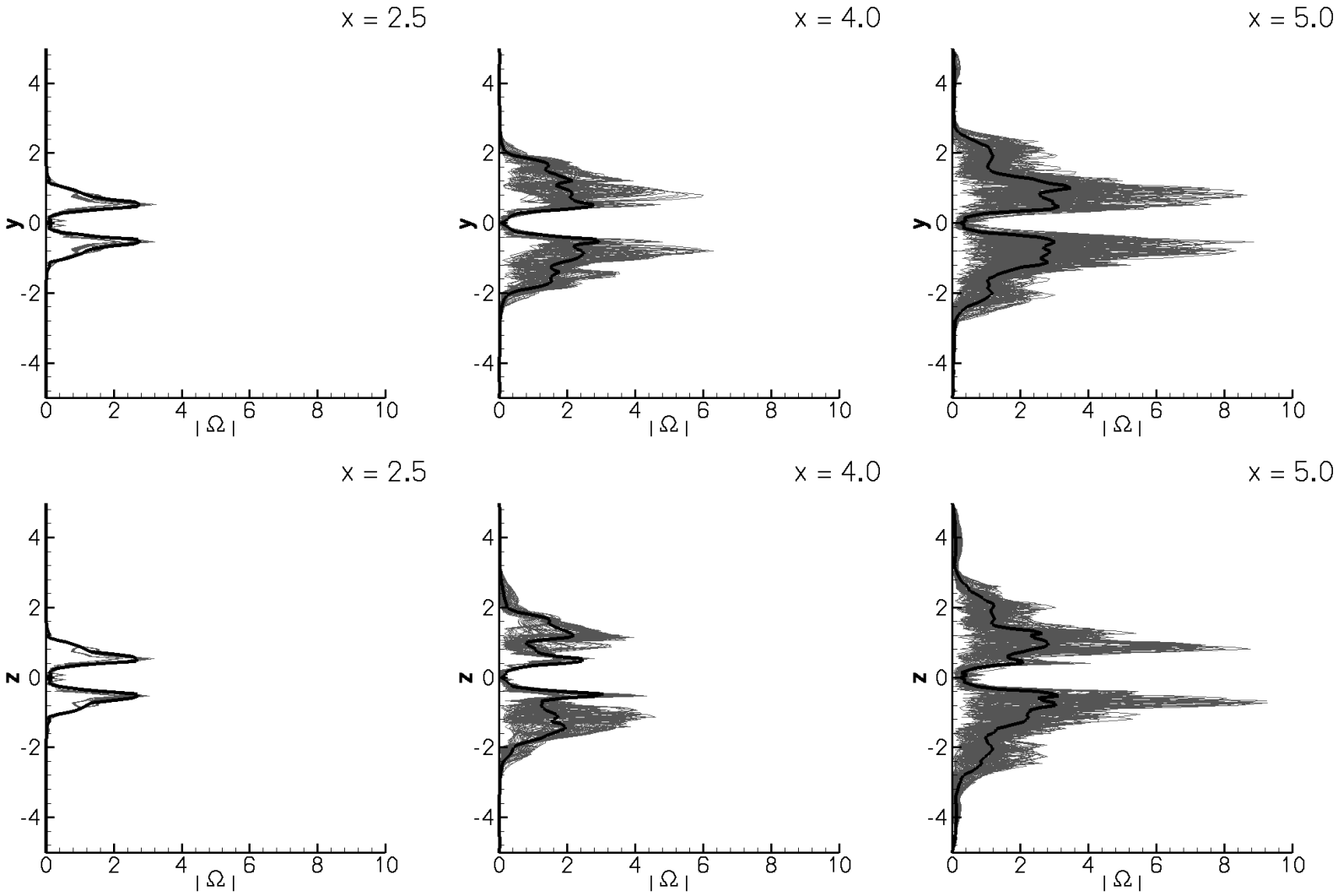

Figure 16. Profiles of the vorticity magnitude near the jet inlet. The thick black lines are the time-averaged profiles. The thin gray lines are instantaneous profiles spaced 50 time steps apart. The *y* profiles are on the *z* = constant plane and likewise for the *z* profiles.

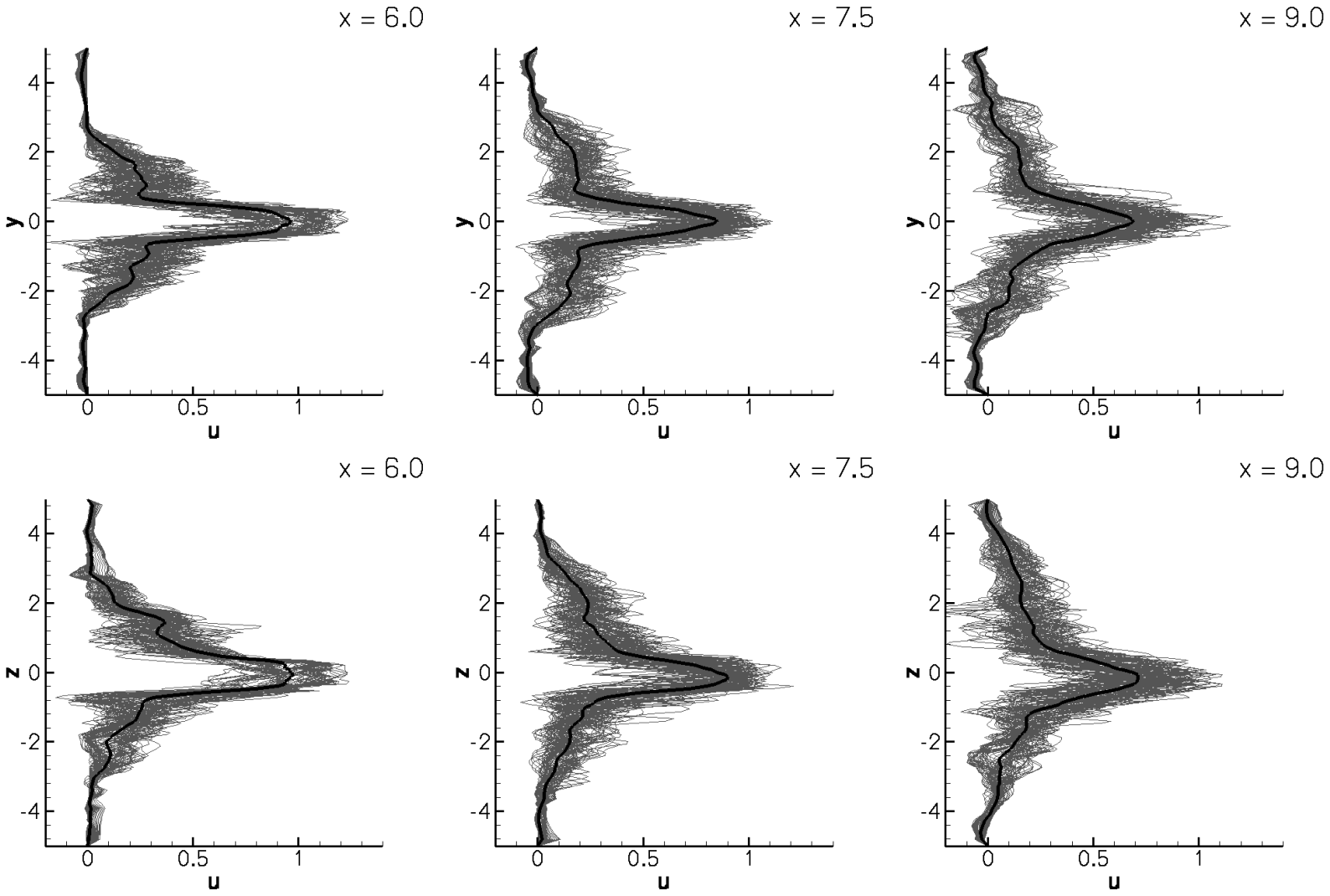

Figure 17. Profiles of the axial velocity near the exit of the computational domain. The thick black lines are time-averaged profiles. The thin gray lines are instantaneous profiles spaced 50 time steps apart. The *y* profiles are on the *z* = constant plane and likewise for the *z* profiles.

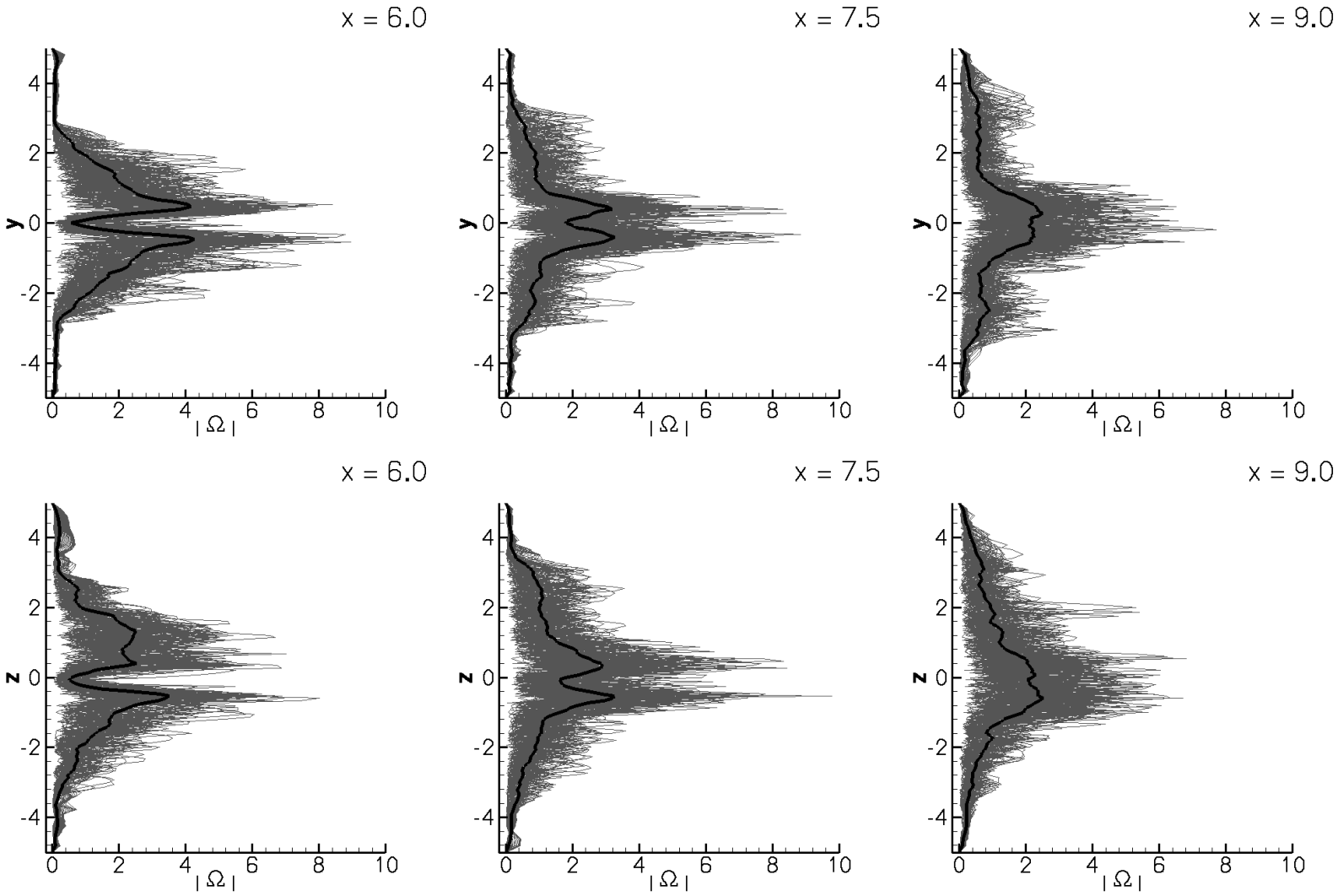

Figure 18. Profiles of the vorticity magnitude near the exit of the computational domain. The thick black lines are time-averaged profiles. The thin gray lines are instantaneous profiles spaced 50 time steps apart. The *y* profiles are on the *z* = constant plane and likewise for the *z* profiles.

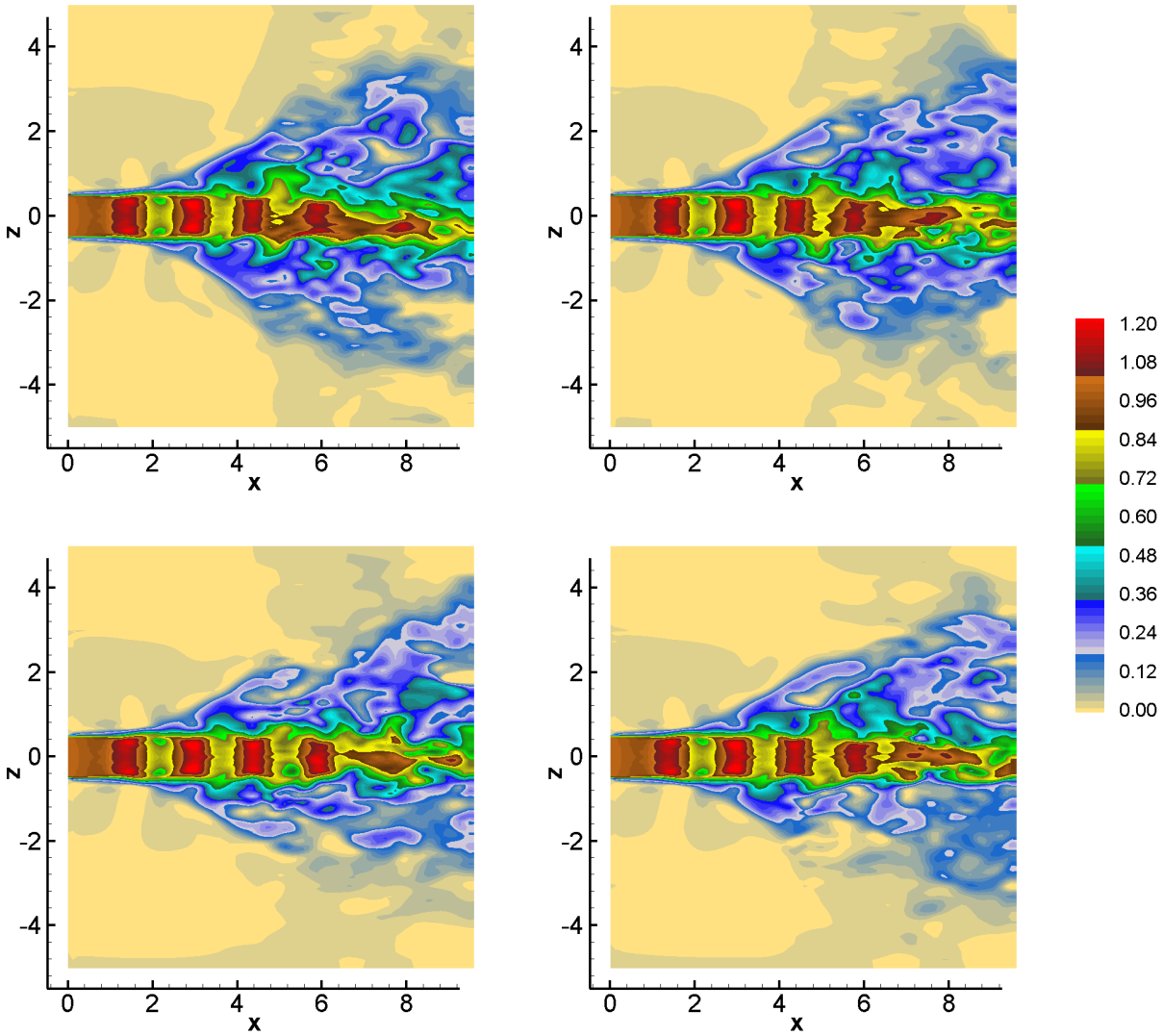

Figure 19. Contours of the axial velocity u on the $y = 0$ plane plotted at four instants in time (t = 25, 50, 75, and 100).

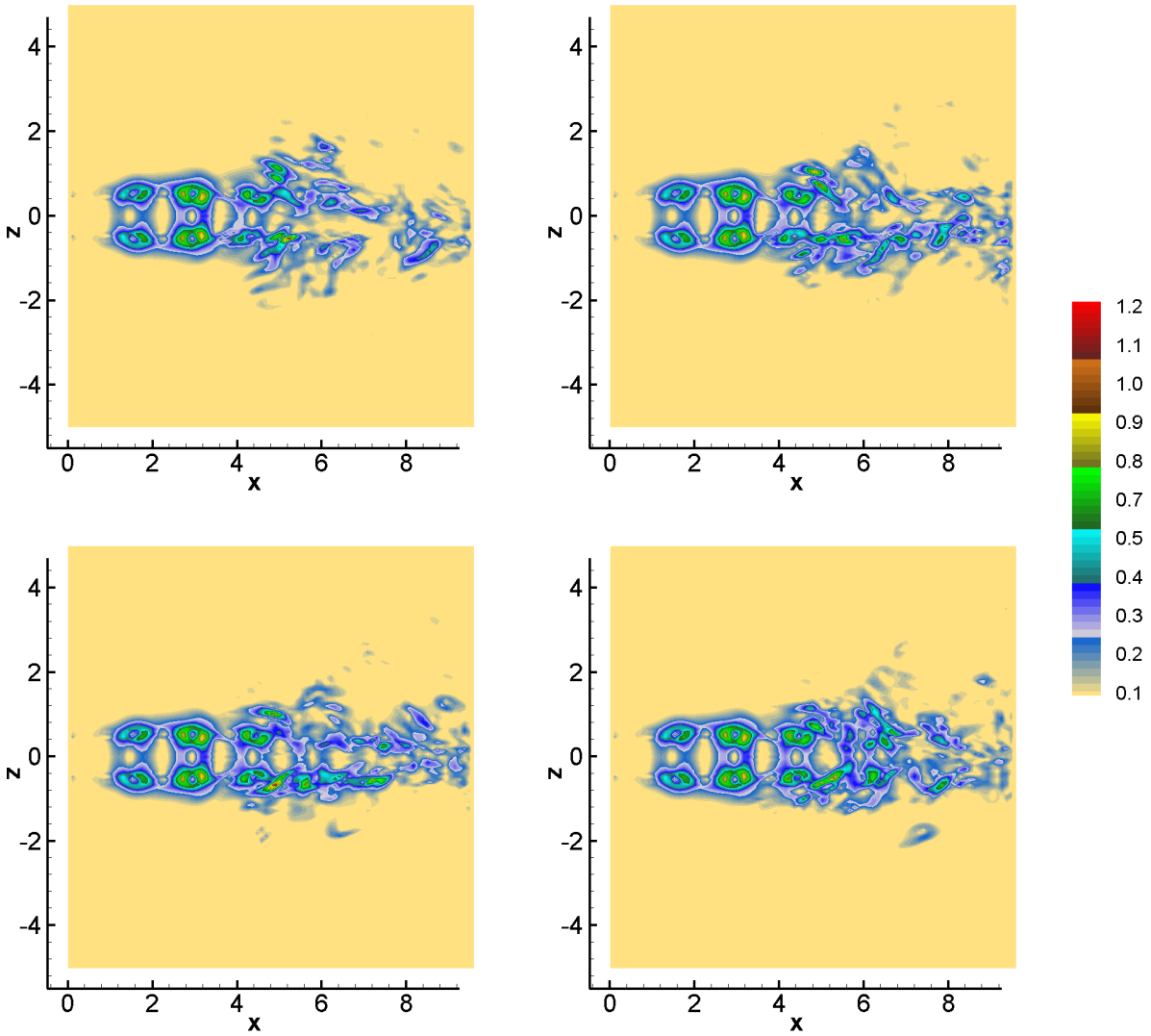

Figure 20. Contours of the pressure gradient $|\nabla P|$ on the $y = 0$ plane plotted at four instants in time (t = 25, 50, 75, and 100).

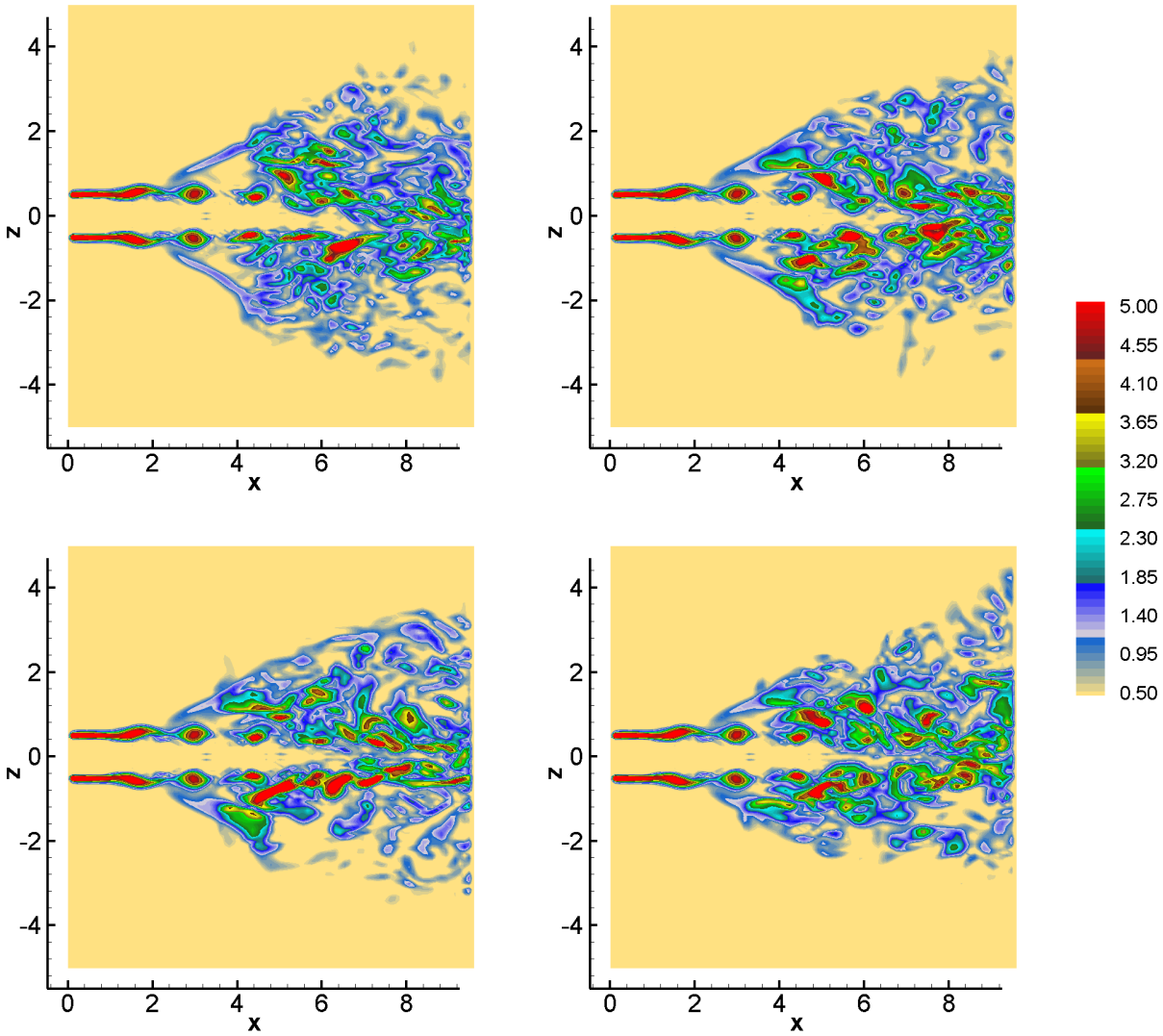

Figure 21. Contours of the vorticity magnitude $|\Omega|$ on the $y = 0$ plane plotted at four instants in time (t = 25, 50, 75, and 100).

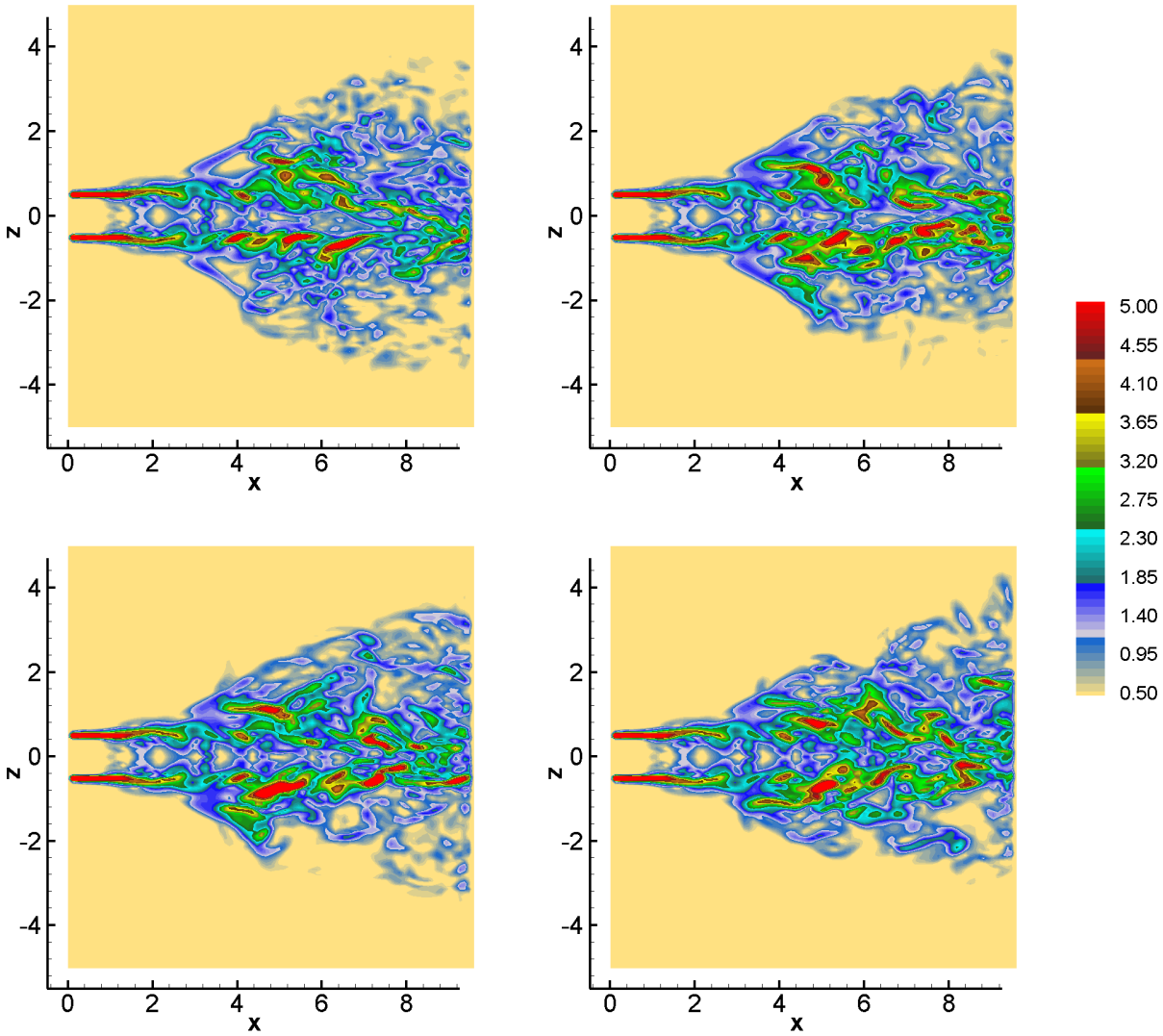

Figure 22. Contours of the strain rate $|S|$ on the $y = 0$ plane plotted at four instants in time (t = 25, 50, 75, and 100).

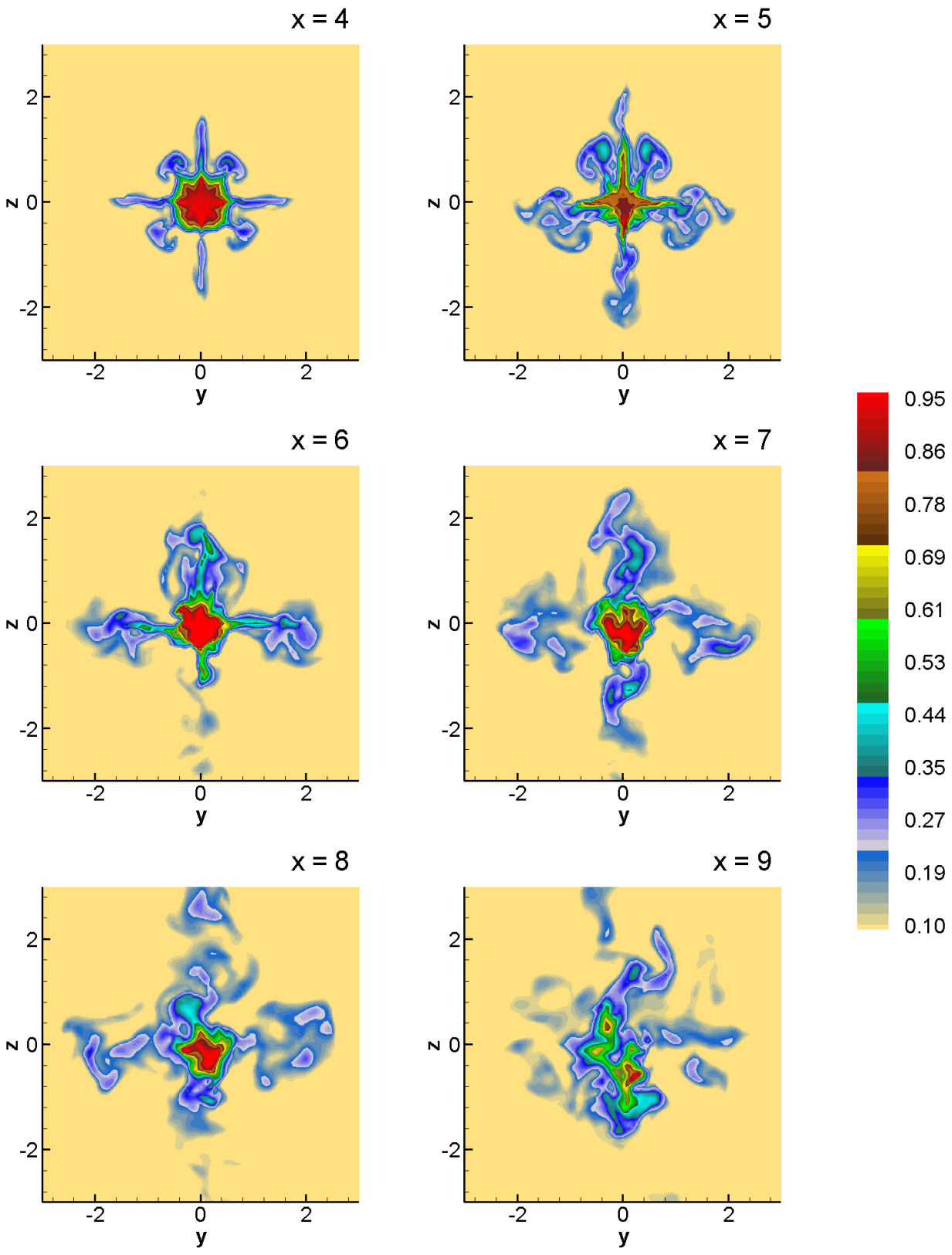

Figure 23. Instantaneous contours (t = 30) of axial velocity u at several cross sections.

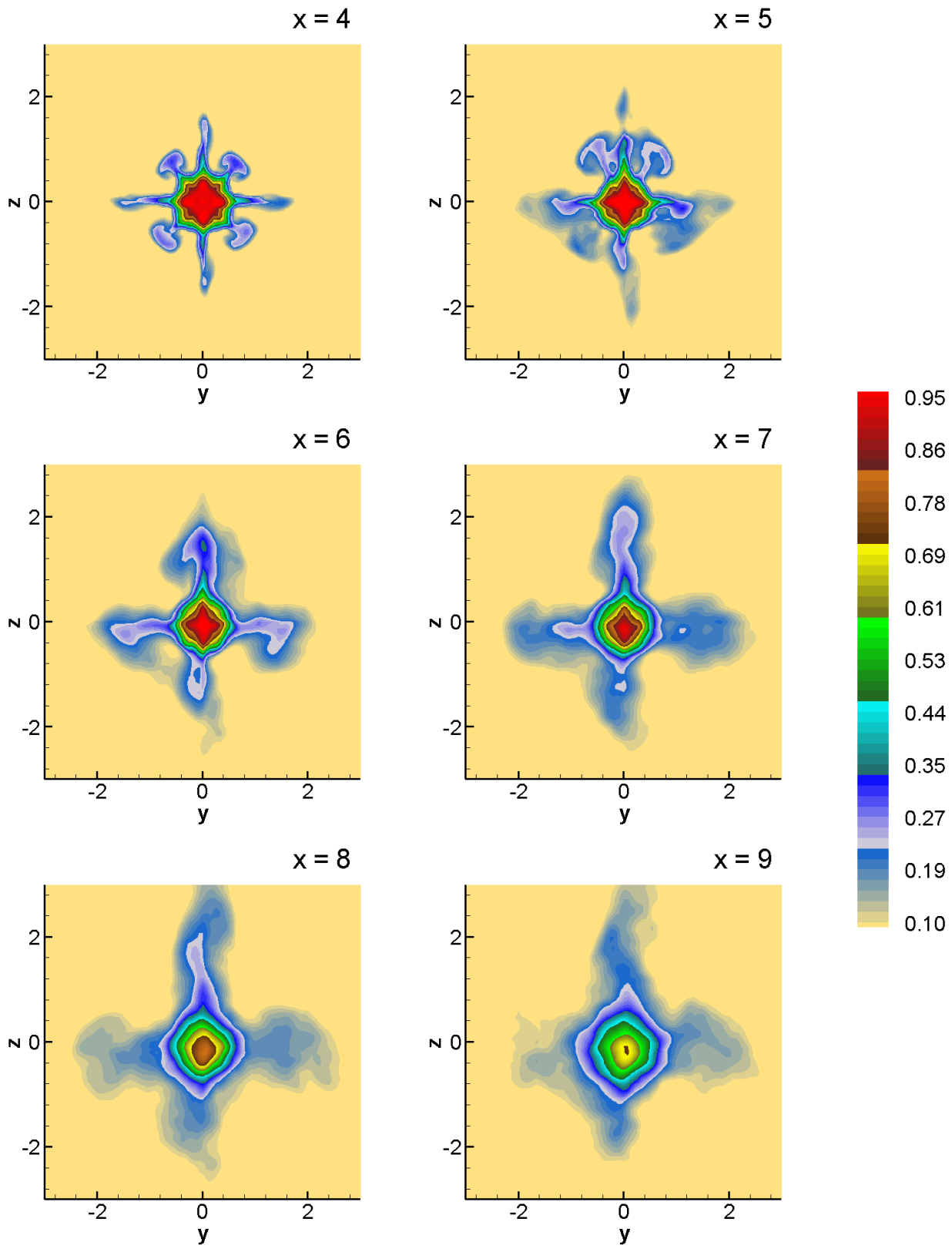

Figure 24.Contours of the time-averaged axial velocity $\bar{u}$ for several cross sections.

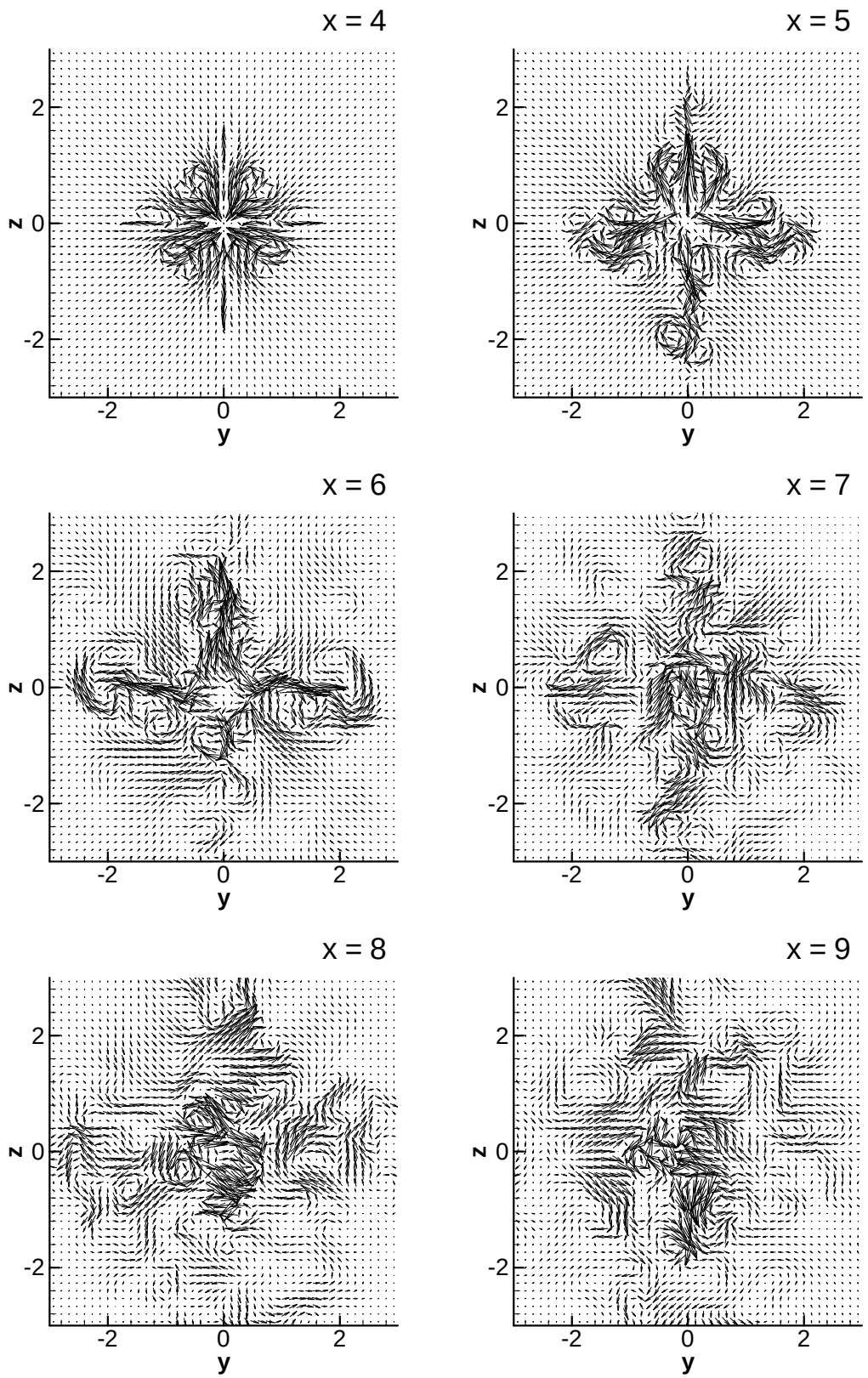

Figure 25. Instantaneous (t = 30) vectors of the transverse velocities (v and w) for several cross sections.

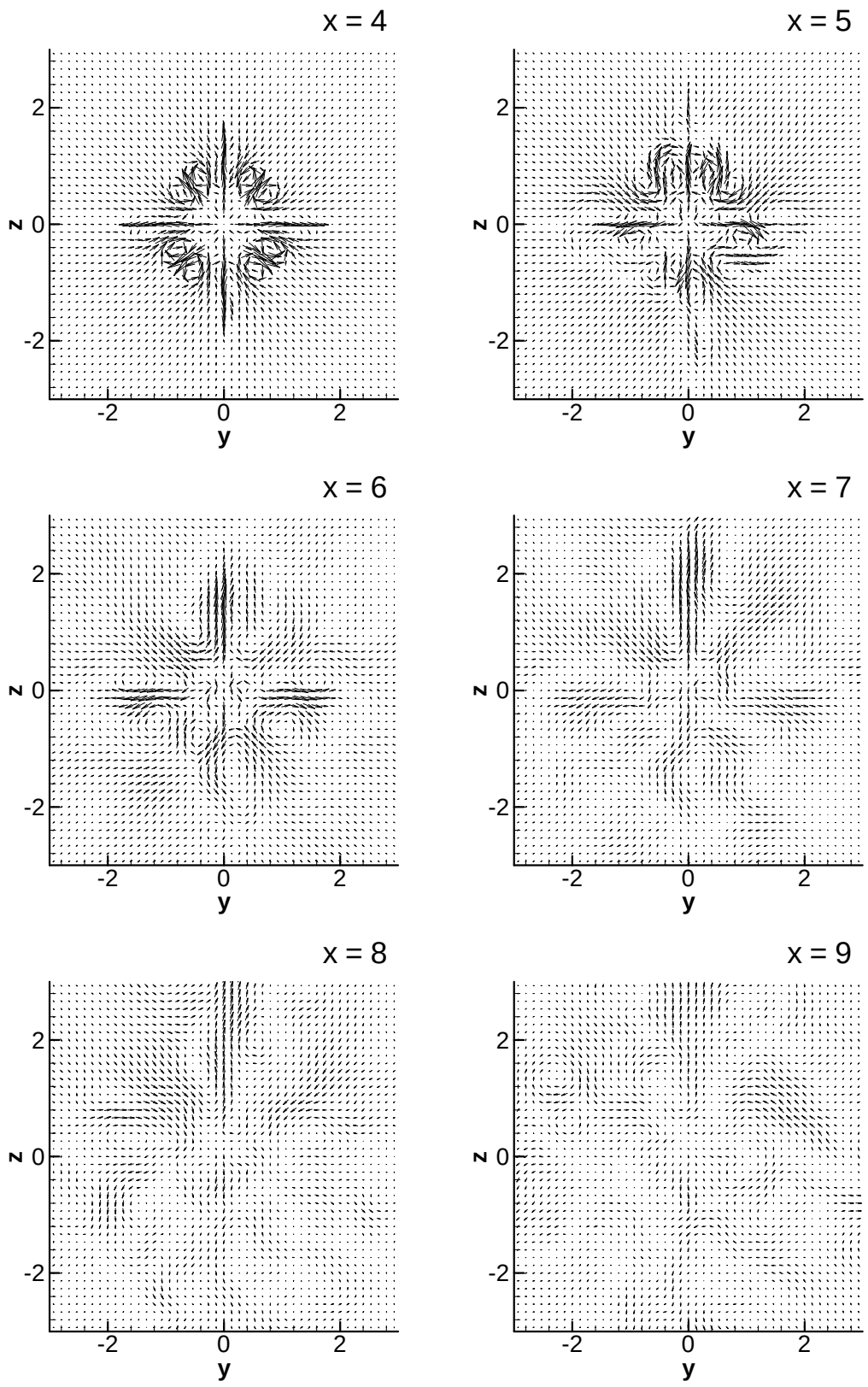

Figure 26. Vectors of the time-averaged transverse velocity $(\overline{v}$ and $\overline{w})$ for several cross sections.

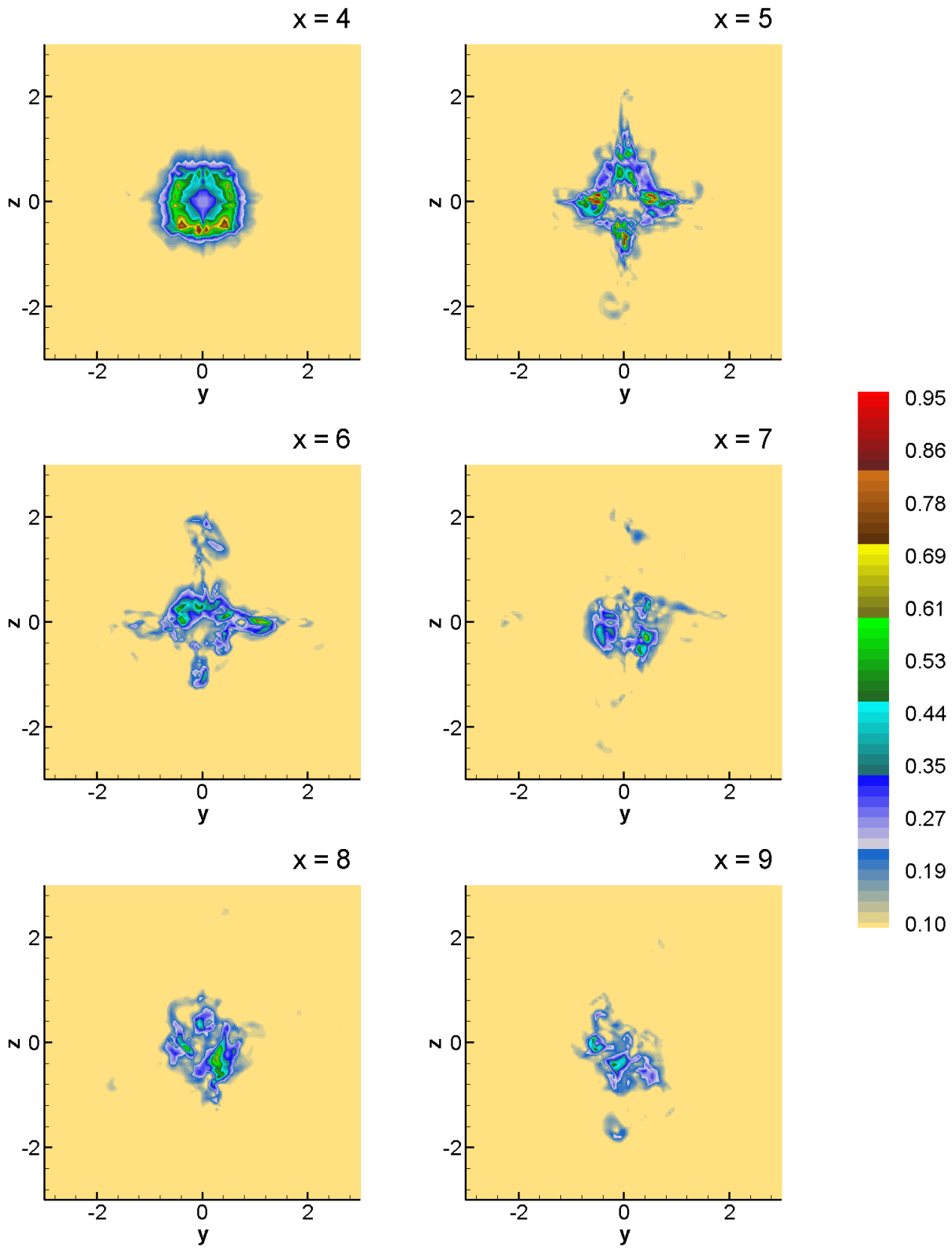

Figure 27. Instantaneous (t = 30) contours of pressure gradient $|\nabla P|$ for several cross sections.

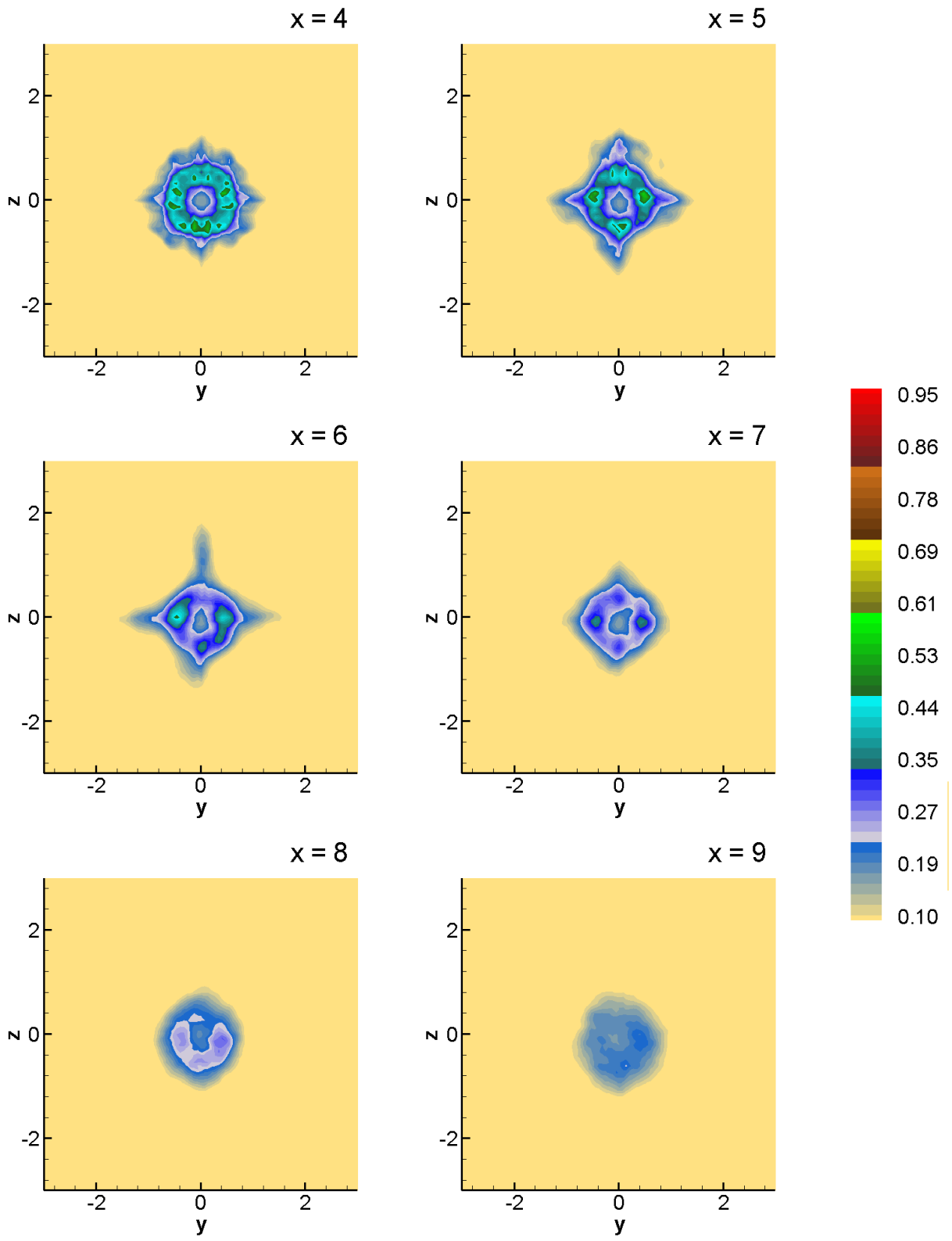

Figure 28. Contours of the time-averaged pressure gradient $\left|\nabla \overline{P}\right|$ for several cross sections.

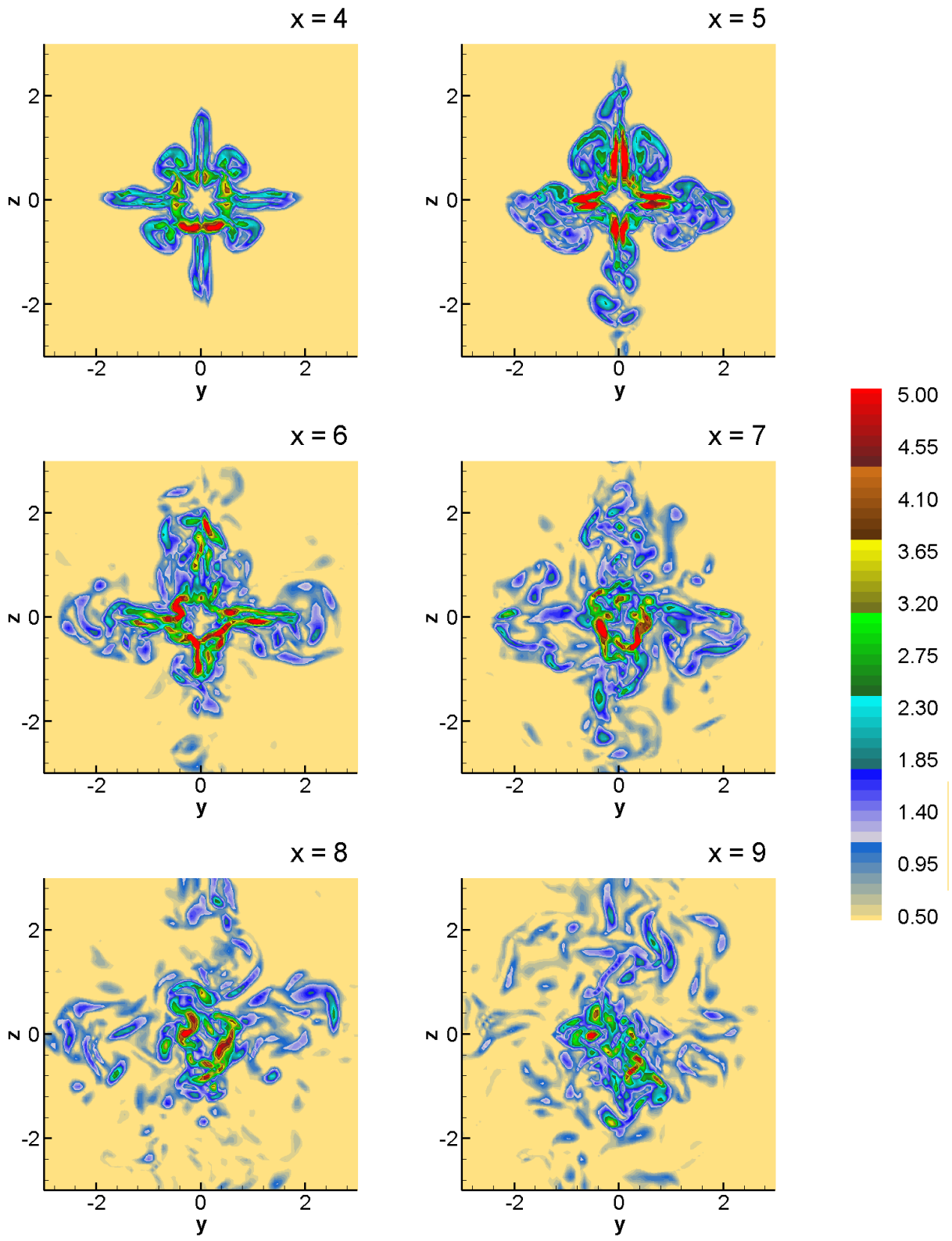

Figure 29. Instantaneous (t = 30) contours of the vorticity magnitude $|\Omega|$ for several cross sections.

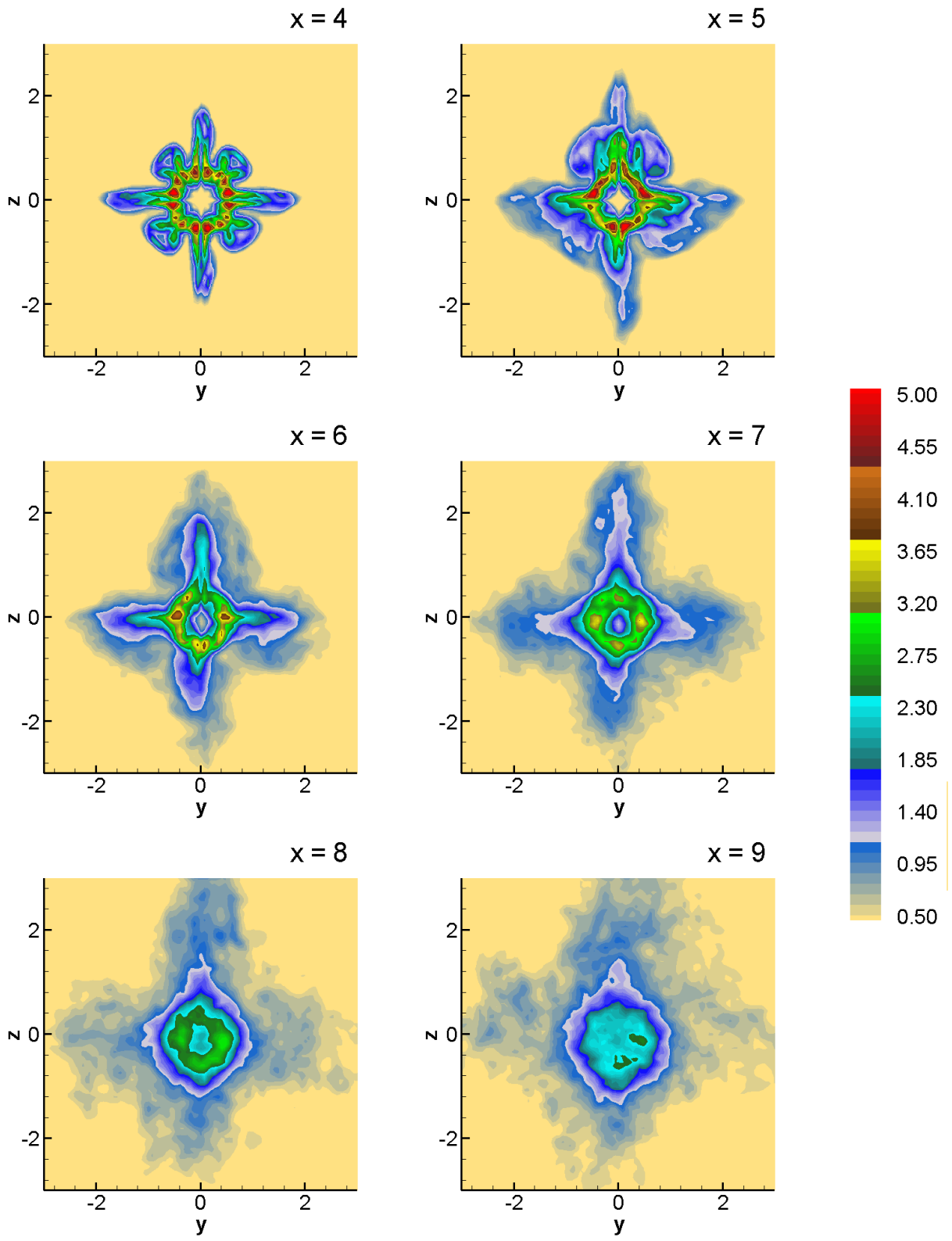

Figure 30. Contours of the time-averaged vorticity magnitude $|\bar{\Omega}|$ for several cross sections

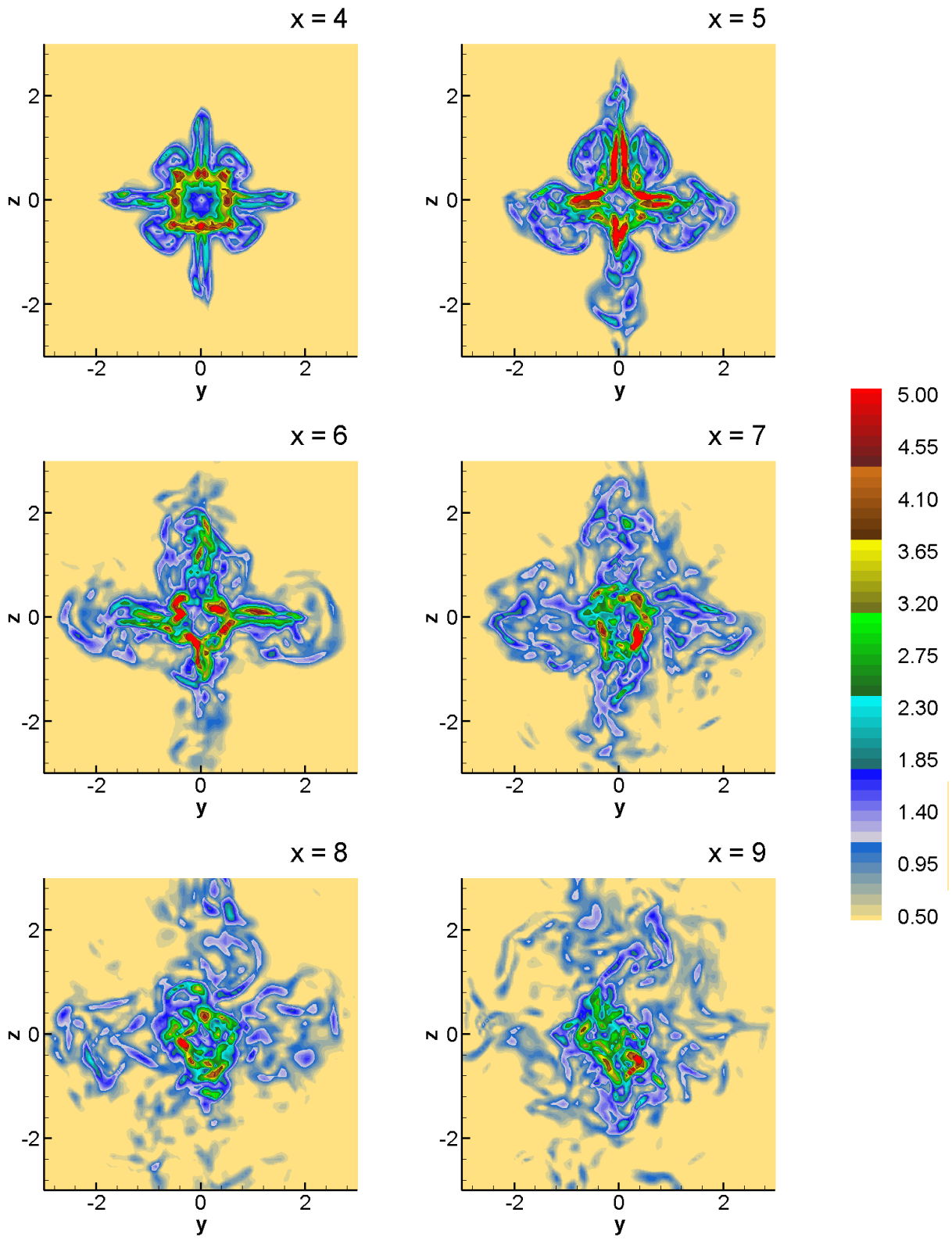

Figure 31. Instantaneous (t = 30) contours of the strain rate $|S|$ for several cross sections.

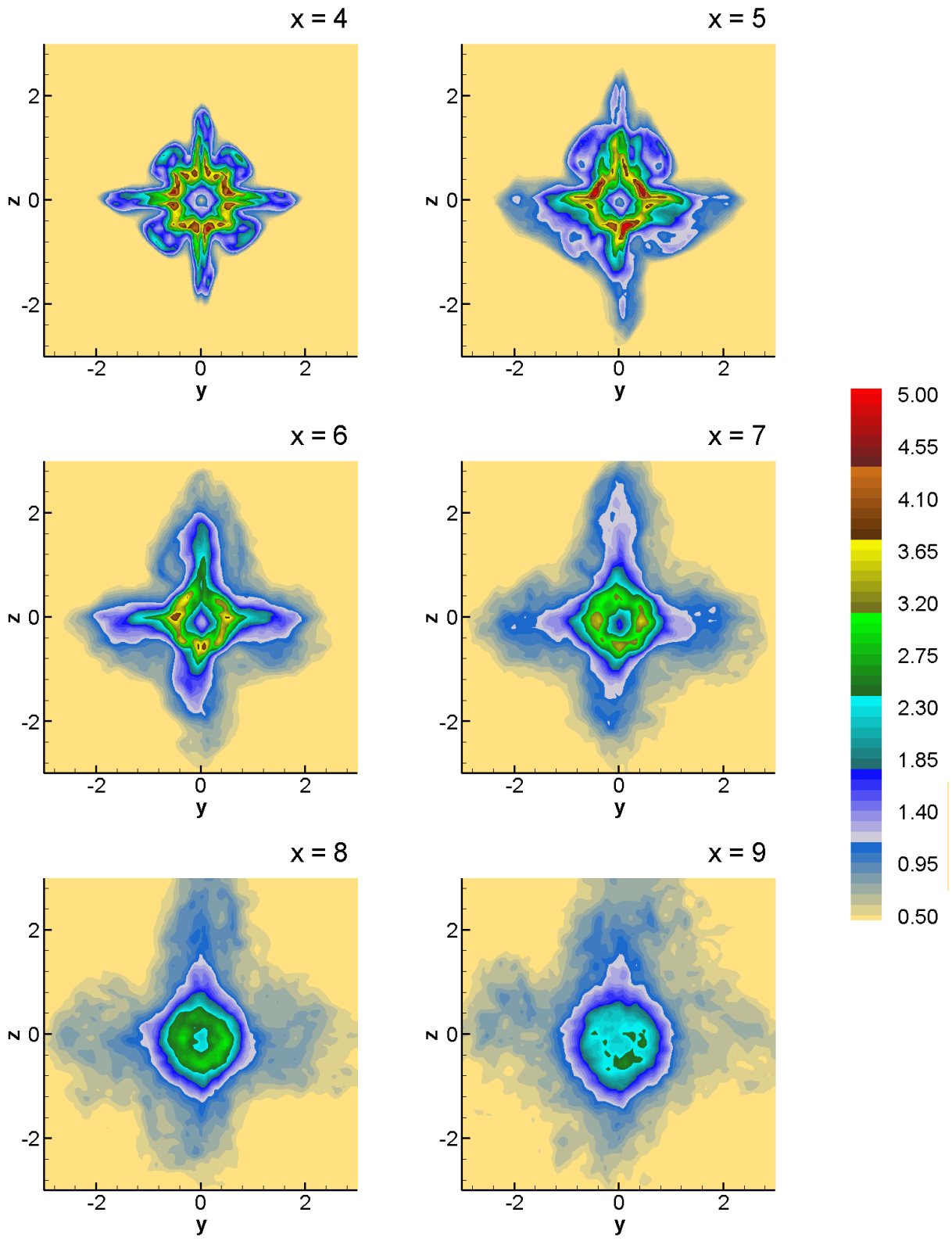

Figure 32. Contours of the time-averaged strain rate $\left|\bar{S}\right|$ for several cross sections.

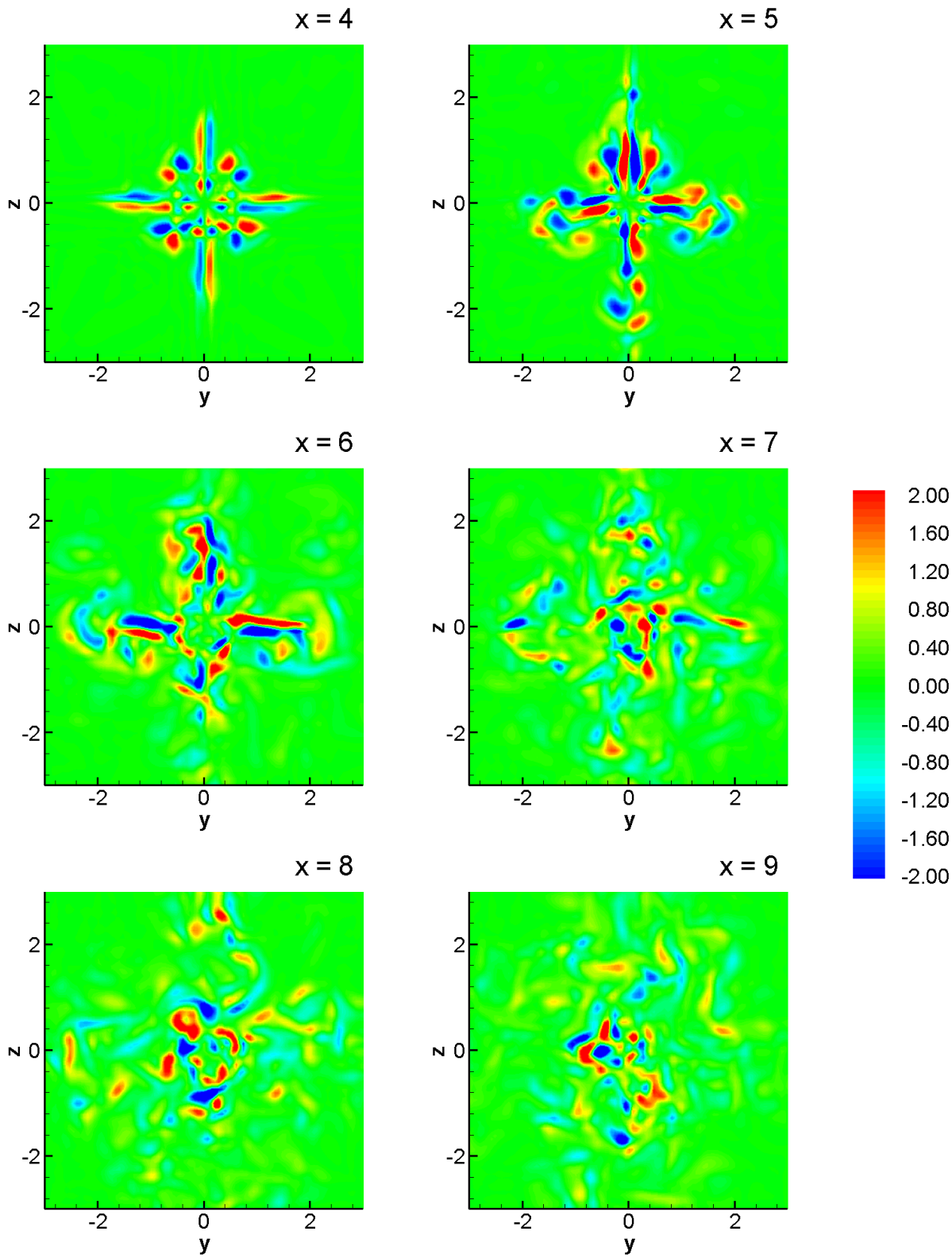

Figure 33. Instantaneous (t = 30) contours of the axial vorticity Ω_x for several cross sections.

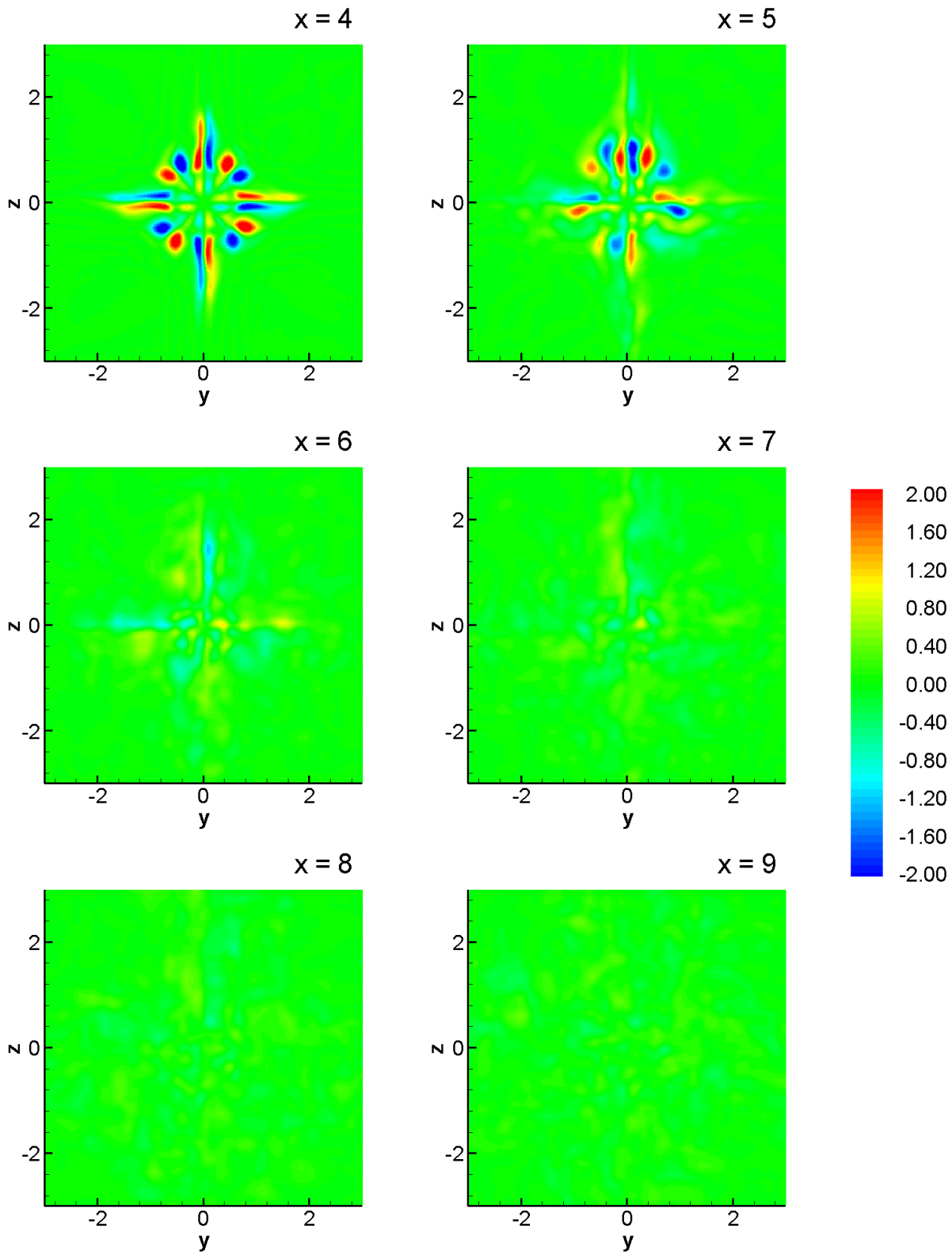

Figure 34. Contours of the time-averaged axial vorticity $\bar{\Omega}_x$ for several cross sections.

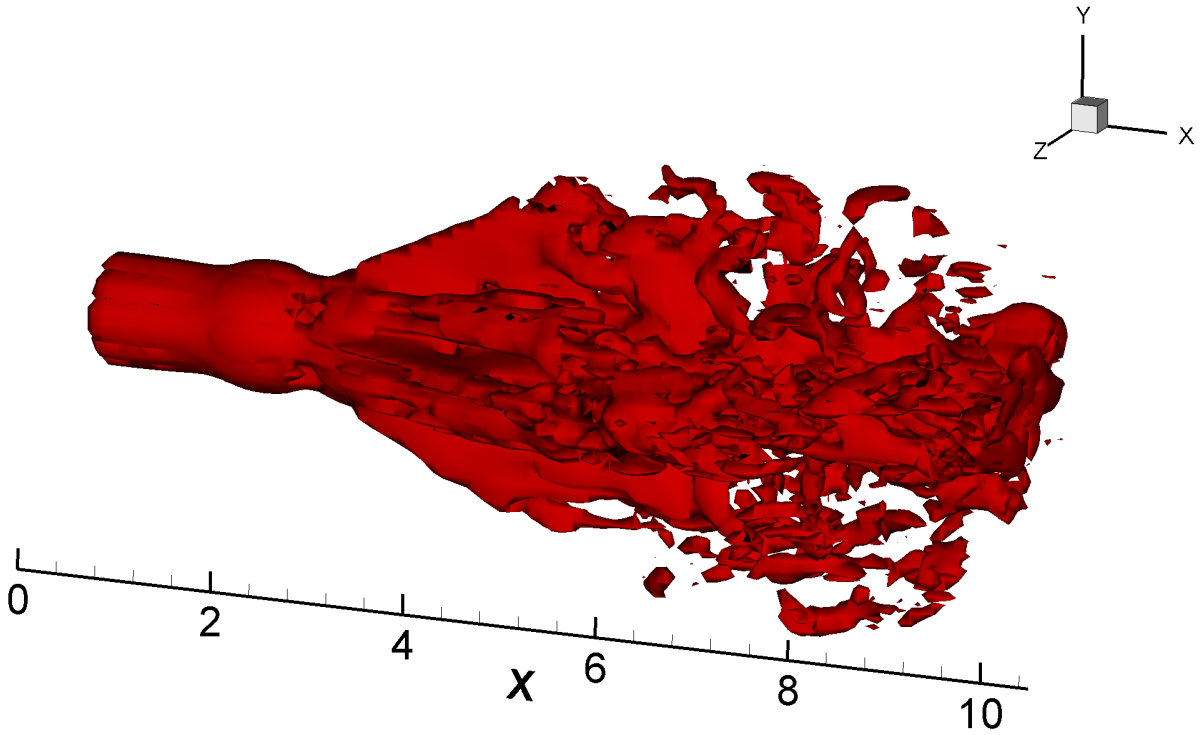

Figure 35. Instantaneous (t = 30) iso-surface of constant vorticity magnitude $\left(|\Omega| = 1.5\right)$.

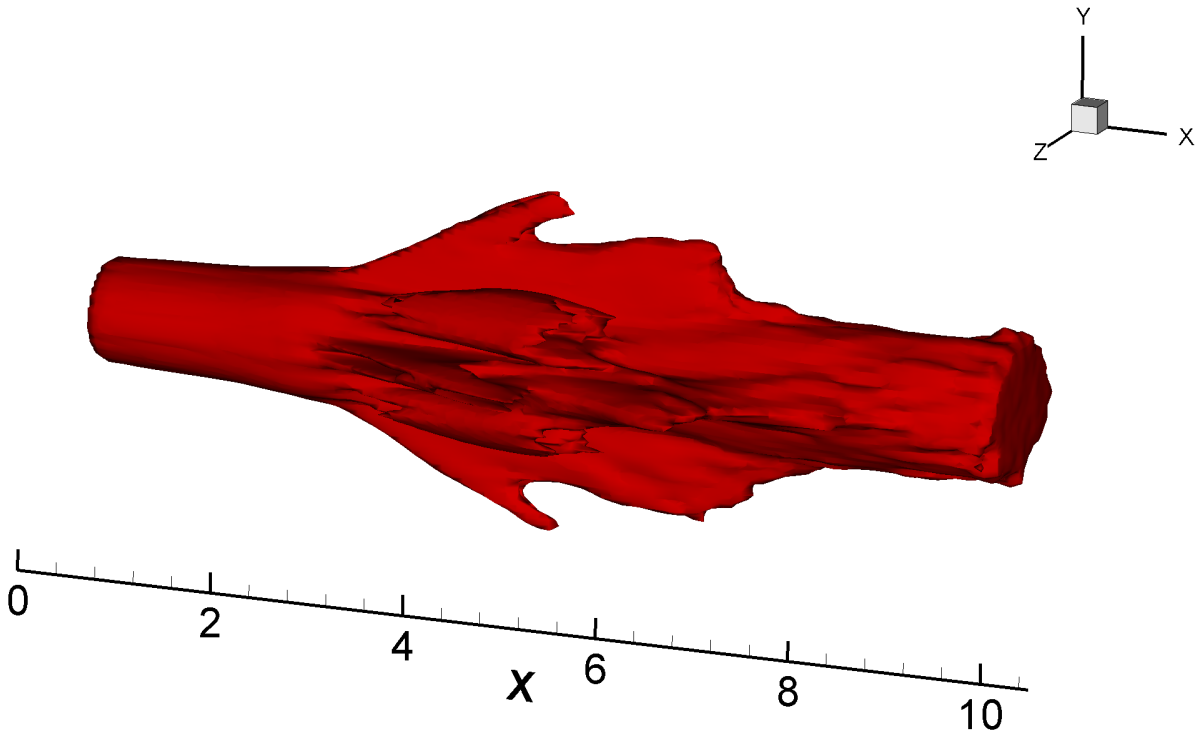

Figure 36. Surface of constant vorticity magnitude $\left(|\bar{\Omega}| = 1.5\right)$ in the time-averaged flow field.

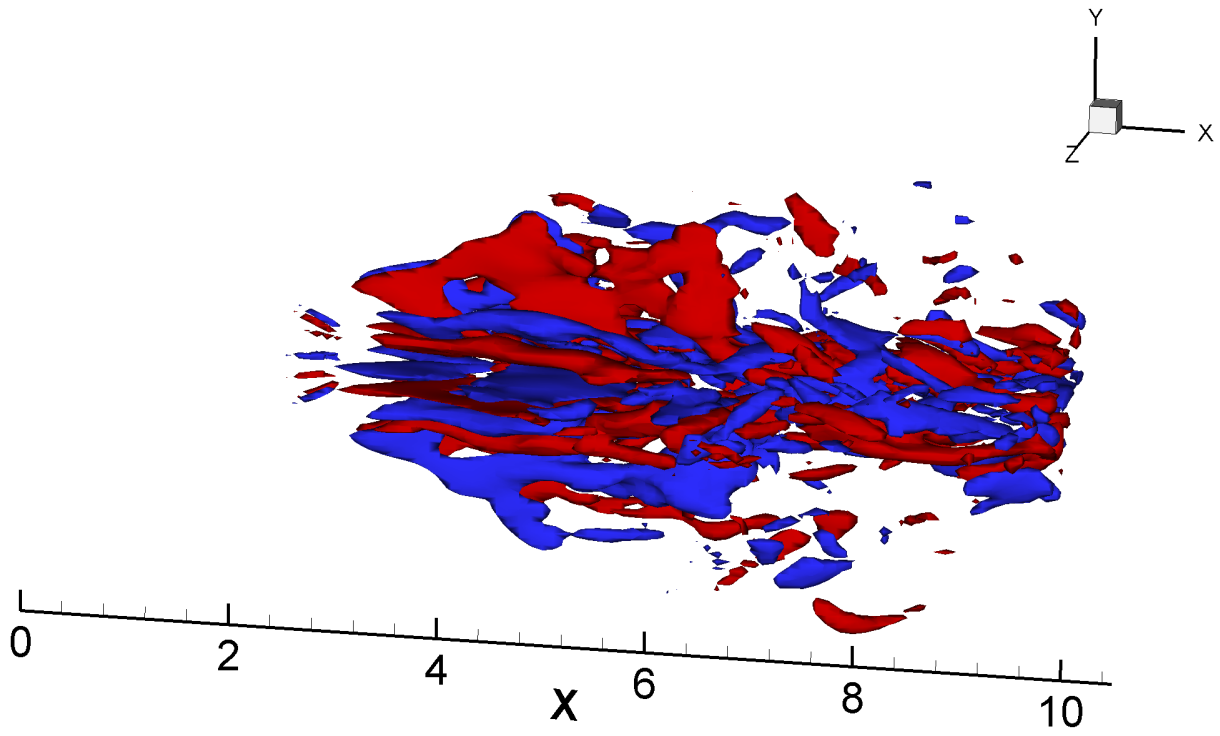

Figure 37. Surfaces of positive (red) and negative (blue) axial vorticity $(\Omega_x = \pm 1.5)$ at t = 30.

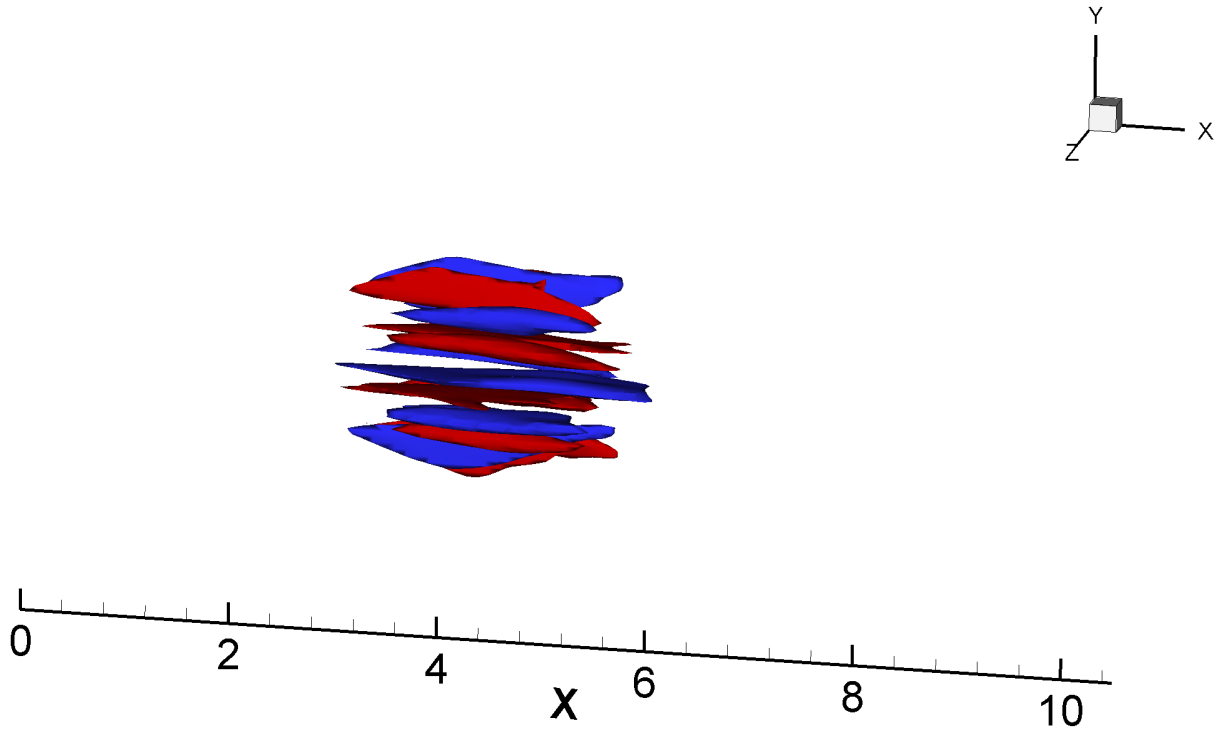

Figure 38. Surfaces of positive (red) and negative (blue) axial vorticity $(\Omega_x = \pm 1.5)$ in the time-averaged flow field.

7. Comparison of *Re* = 100,000 and 300,000 Predictions

In this section, we consider the effect of the Reynolds number on the simulated jet by comparing the snapshots of predicted instantaneous flow fields in the same manner as was followed in §6, where we compared the instantaneous to the time-averaged flow. In addition to the components of the instantaneous velocity, we also compare several computed quantities—the pressure gradient, the vorticity, and the strain rate—whose magnitudes are proportional to the forces that would act on a fish suspended in such a flow. Definitions of these quantities are given Eqs. 36–39 in §6.

Figs. 39–43 show the flow fields at the two Reynolds numbers studied with two snapshots of the flow field for each Reynolds number. The snapshots for *Re* = 100,000 are shown on the top of each figure, those for *Re* =300,000 are on the bottom of each figure. For both Reynolds numbers, the snapshots are 10.5 non-dimensional time units apart (d/U). Note that the contour levels in the figures in this section are different from those presented in the §6. The magnitudes of the various quantities that are shown are in general higher in the *Re* = 300,000 simulation; therefore, a wider range of contour levels were required to show the details in the flow fields at both Reynolds numbers.

The axial velocity plots in Fig. 39 show that the potential core region of the higher *Re* jet is significantly shorter than in the lower *Re* jet. This can be most clearly seen by concentrating on the yellow contours in both of the jets. In the lower *Re* jet, the yellow contours are visible in the jet region $(-0.5d < z < 0.5d)$ along the whole length of the jet, and the contour seems to remain a part of the same structure even though it appears to have begun to oscillate about the centerline. However, in the higher *Re* jet any coherence of the yellow contours disappeared for $x > 5d$, and only small patches of yellow appear in the downstream portion of the jet.

Fig. 40 shows the instantaneous magnitude of the pressure gradient in both jets. The most remarkable difference between the jets in this figure is that much more small scale structure is present in the higher *Re* jet. This reduction in scale is a hallmark of higher Reynolds number turbulence, and we will return to this issue in the subsequent discussion. The pressure gradient plots also indicate the presence of vortex rings (see also Figs. 1,2) just downstream of the nozzle

exit as high pressure areas. In the high *Re* jet, the pressure gradient in these rings have much higher levels than in the lower *Re* jet.

Figs. 41 and 42 show the vorticity magnitude and the strain-rate magnitude in the low and the high *Re* simulated jets.Comparing the two *Re* jets in these figures dramatically illustrates the much finer structure of the turbulent region of the high *Re* jet. This result is expected for the turbulent flows where the range of length scale is directly proportional to the Reynolds number. The largest length scale in the flow is dictated by the geometry and in the case of the jet is on the order of the diameter of the jet, which is fixed by the experimental appratus. The smallest length scale, however, decreases with increasing *Re*. Moreover, and perhaps more importantly for fish that are suspended in such a flow, the time scales in the flow also decrease with increasing *Re*. Therefore, as the *Re* increases the rate at which the flow field (and quantities like the strear rate and vorticity) fluctuates increases, and the fish's immediate environment changes more and more rapidly.

The vorticity magnitude and strain-rate magnitude plots also show several relatively large-scale pockets (meaning the size of the pockets is of the same order as the jet diameter) that have very high instantaneous values of vorticity and shear. More of these structures appear in the high *Re* jet than in the low *Re* jet. In both jets, however, the magnitude of these structures is the same or larger than the magnitude at the exit of the jet nozzle suggesting that fish in the turbulent region may encounter the very high levels of shear and rotation that they experienced upon release into the jet.

Figs. 43–48 show three cross sections for each *Re* located at the same distance from the nozzle exit for one instant in time for both jets. The figures are arranged with the lower *Re* jet on the left, and the higher *Re* jet on the right. For both *Re*, each figure contains a cross section located at $x = 4d$, $6d$, and $8d$. In the following, we discuss each of these figures, which include the axial velocity contours (Fig. 43), transverse velocity vectors (Fig. 44), pressure gradient magnitude contours (Fig. 45), vorticity magnitude contours (Fig. 46), strain-rate magnitude contours (Fig. 47), and axial vorticity contours (Fig. 48).

Considering these figures as a whole, they reinforce the point made previously. that the potential core region is shorter in the high *Re* jet. In particular, the velocity contours (Fig. 43), vor-

ticity contours (Figs. 46, 48), and strain-rate contours (Fig. 47) clearly show that the large-scale mode-four structures that dominated instantaneous flow at the $x = 4d$ cross section in the low *Re* jet have already disappeared at this cross section at higher *Re*. This is consistent with the fact that the potential core has shortened significantly in the higher *Re* jet, and thus the jet transitions to turbulence much closer to the nozzle exit. The transverse velocity vectors in Fig. 44 also show this same trend. Moreover, the high *Re* jet shows a much stonger transverse flow throughout the cross section especially in the center of the jet. Incidentially this figure also reinforces the increase in grid resolution that was necessary to capture the smaller scale structure of the higher *Re* jet. The increase in small scale features of the higher *Re* flow is evident in all of the figures in this group (Fig. 43–48), but it is most clearly evident in the contours of axial vorticity shown in Fig. 48. In this figure, many pairs of fish-sized longitudinal vortices are present.

Fig. 49 shows a three-dimensional snapshot of iso-surfaces of vorticity magnitude in the two different *Re* jets. The high *Re* jet clearly posses much finer scale structure and this structure fills a much large volume of the jet. In both jets, vortex rings are clearly visibile near the nozzle exit with longitudinal (also called braid-region) vortices clearly shown in the low *Re* jet.

In summary, comparisons of the flow fields in the two simulated jets showed that the *Re* = 300,000 jet contains much finer small-scale structures than the Re = 100,000 jet. The higher *Re* jet transitions to turbulence much closer to the nozzle exit.

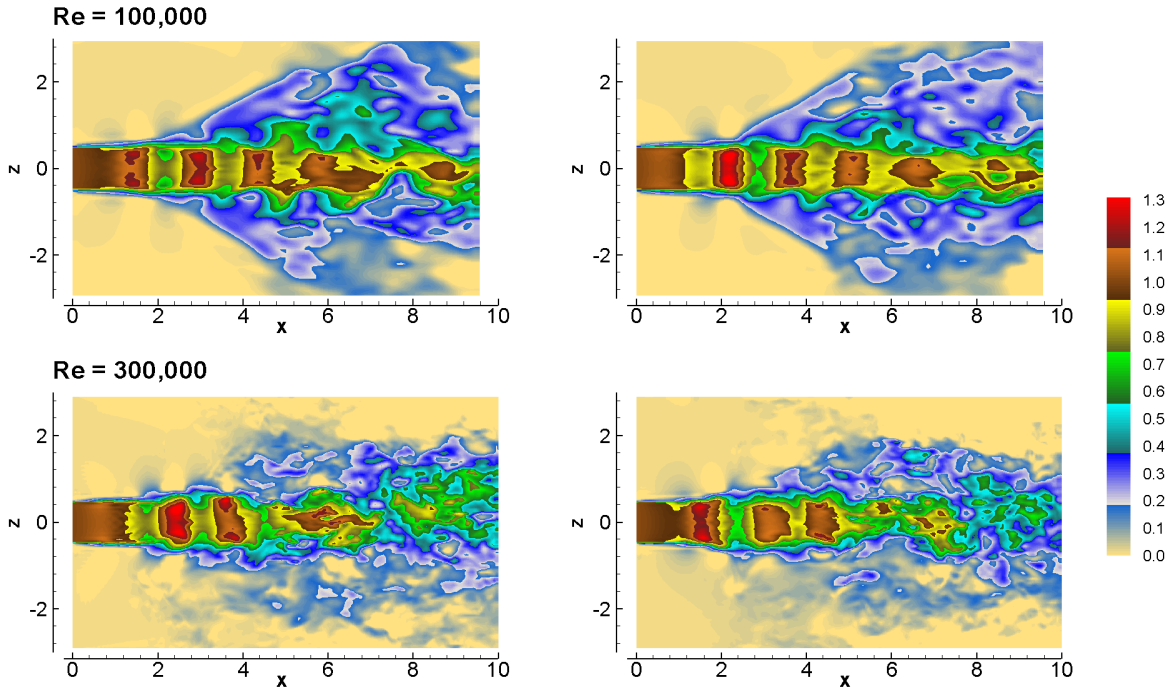

Figure 39. Instantaneous contours of axial velocity u at two different instants in time for both Re = 100,000 and 300,000.

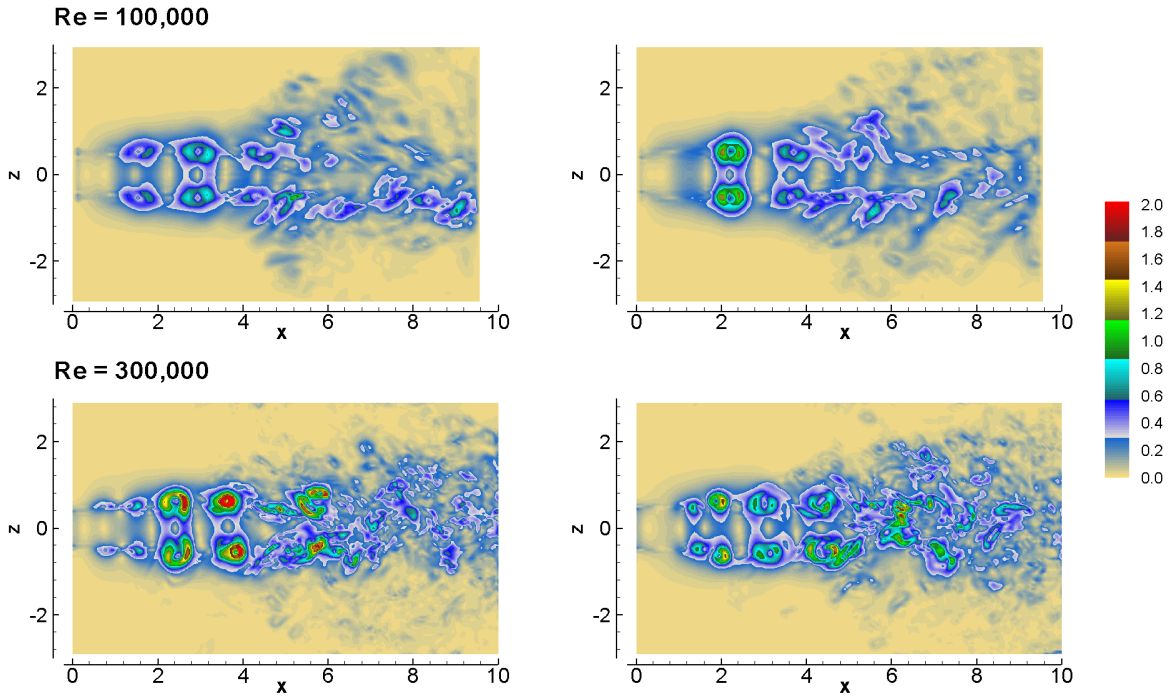

Figure 40. Instantaneous contours of pressure gradient $|\nabla P|$ at two different instants in time for both Re = 100,000 and 300,000.

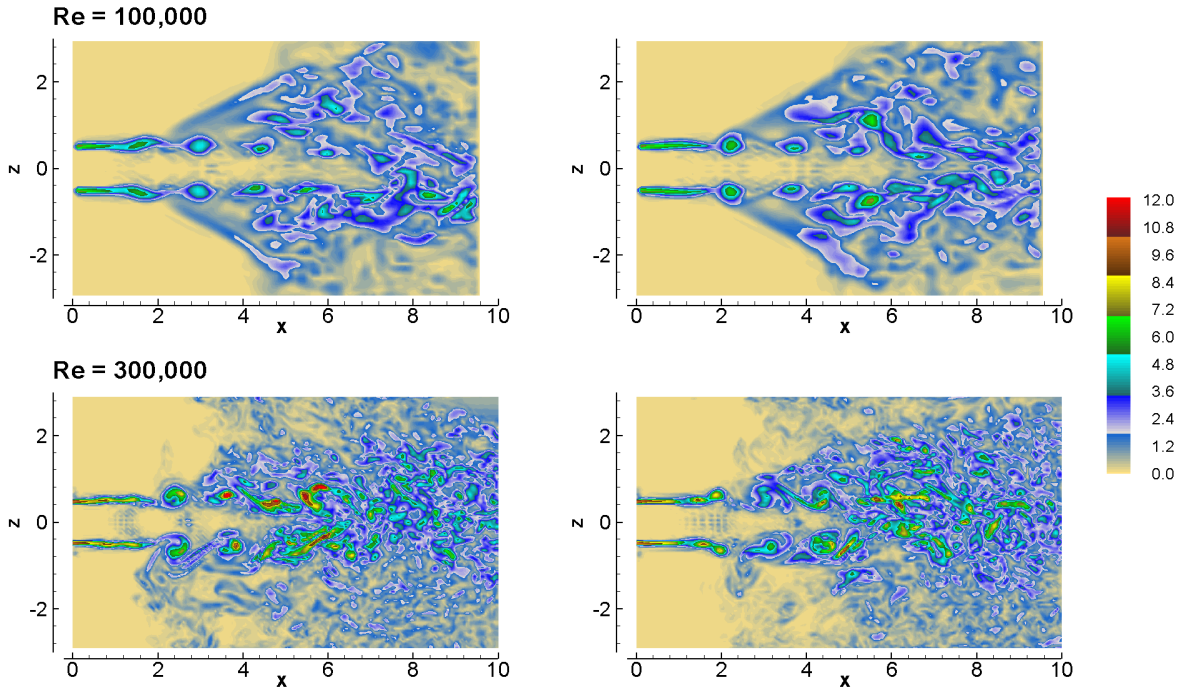

Figure 41. Instantaneous contours of vorticity magnitude $|\Omega|$ at two different instants in time for both *Re* = 100,000 and 300,000.

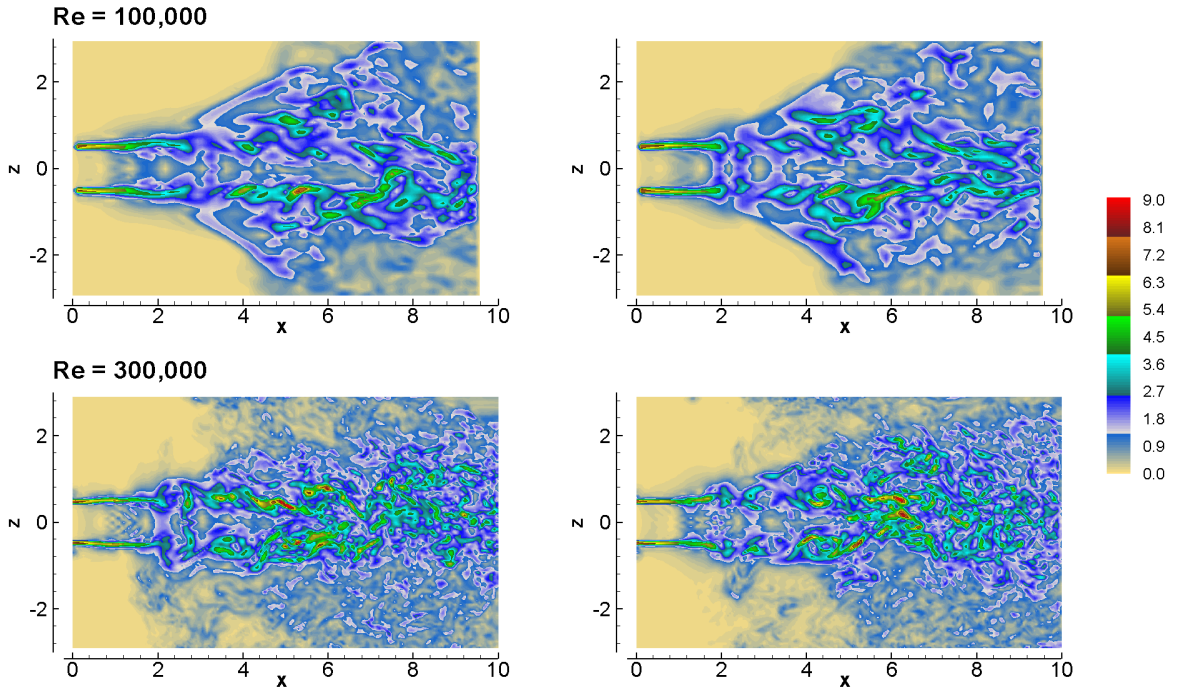

Figure 42. Instantaneous contours of strain rate magnitude $|S|$ at two different instants in time for both *Re* = 100,000 and 300,000.

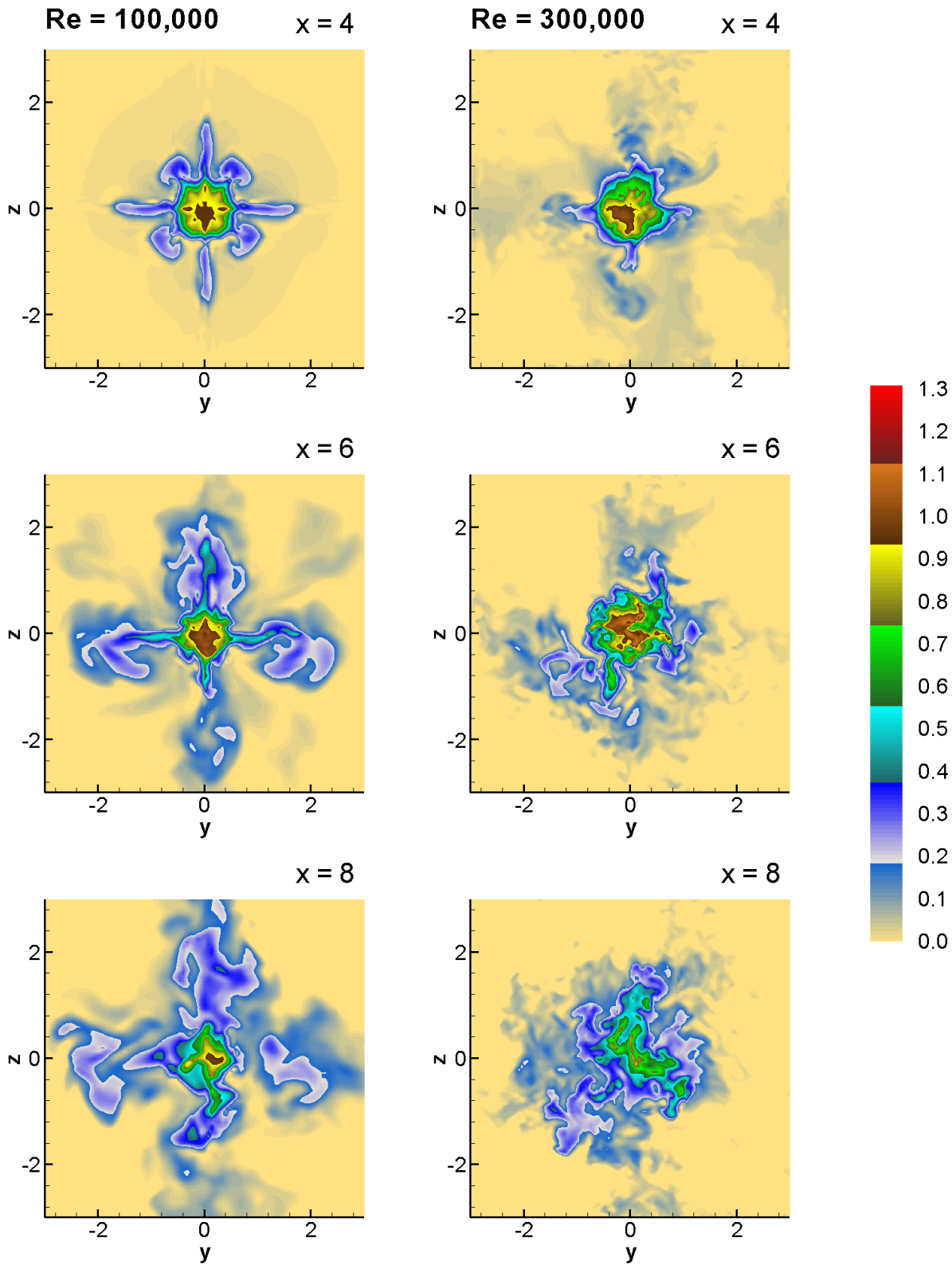

Figure 43. Instantaneous contours of axial velocity *u* at three axial locations for the two Reynolds numbers simulated.

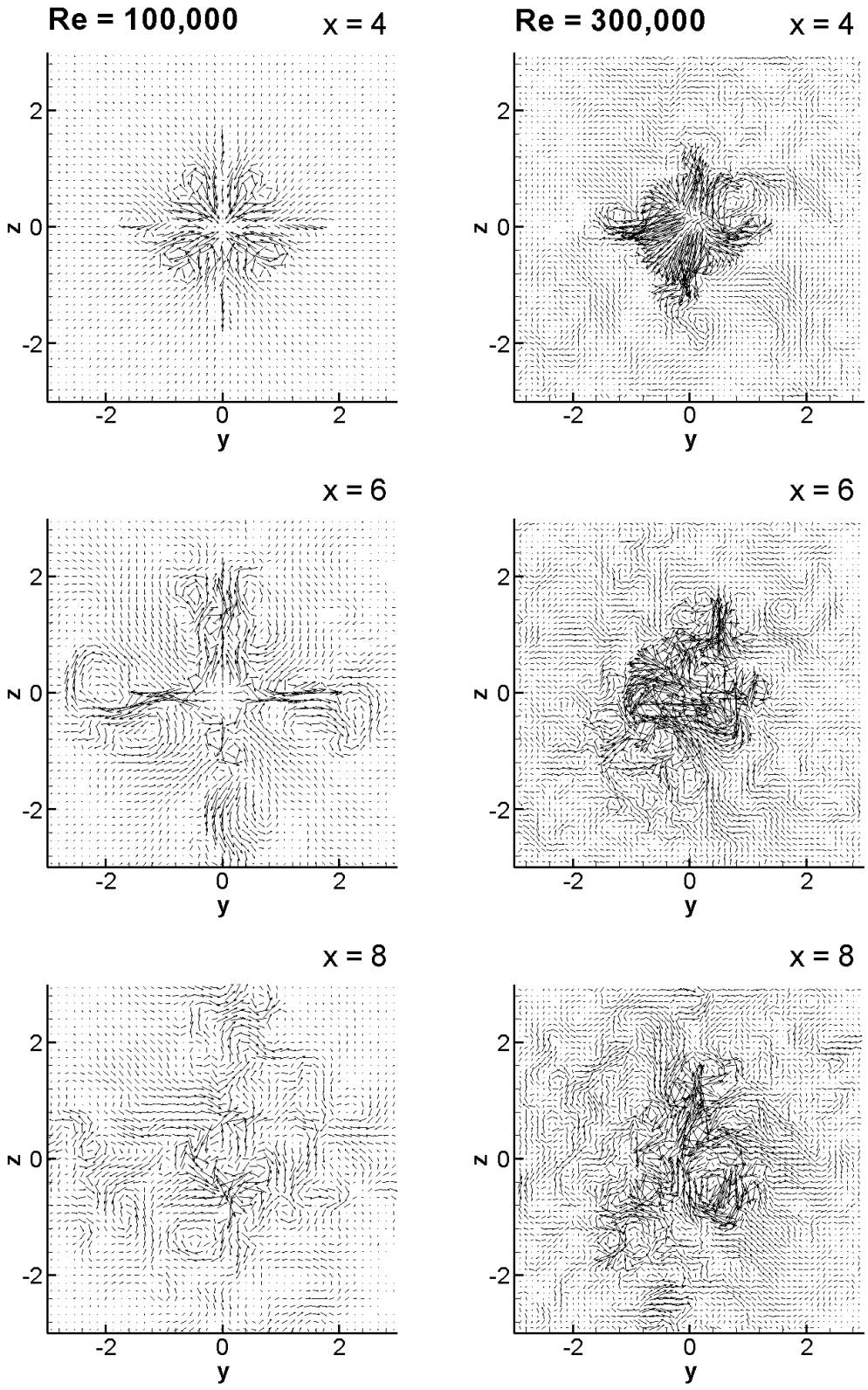

Figure 44. Instantaneous vectors of the transverse velocity field (*v* and *w*) for three cross sections for the two Reynolds numbers simulated.

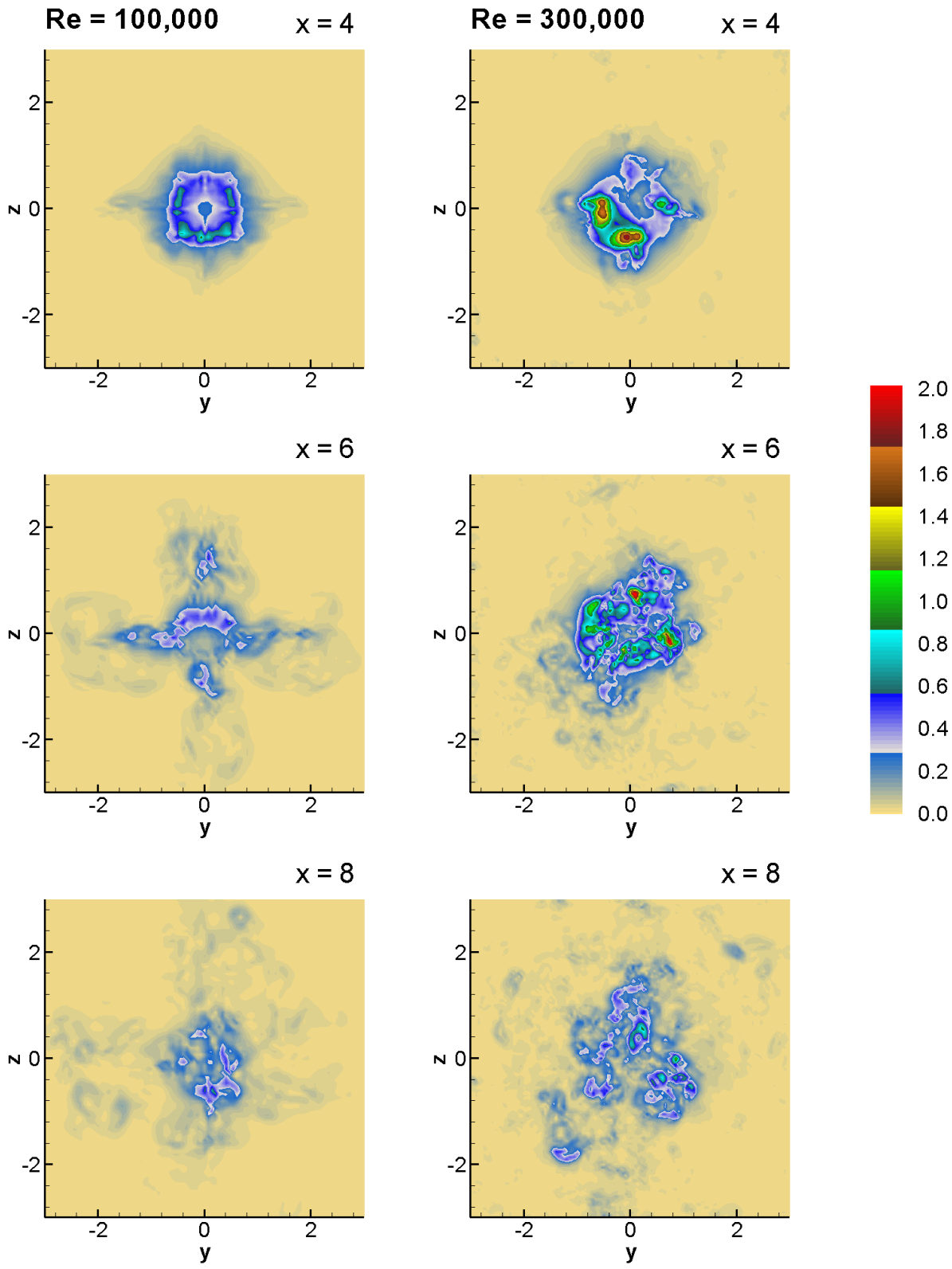

Figure 45. Contours of the instantaneous pressure gradient $|\nabla P|$ for three cross sections in the two Reynolds numbers simulated.

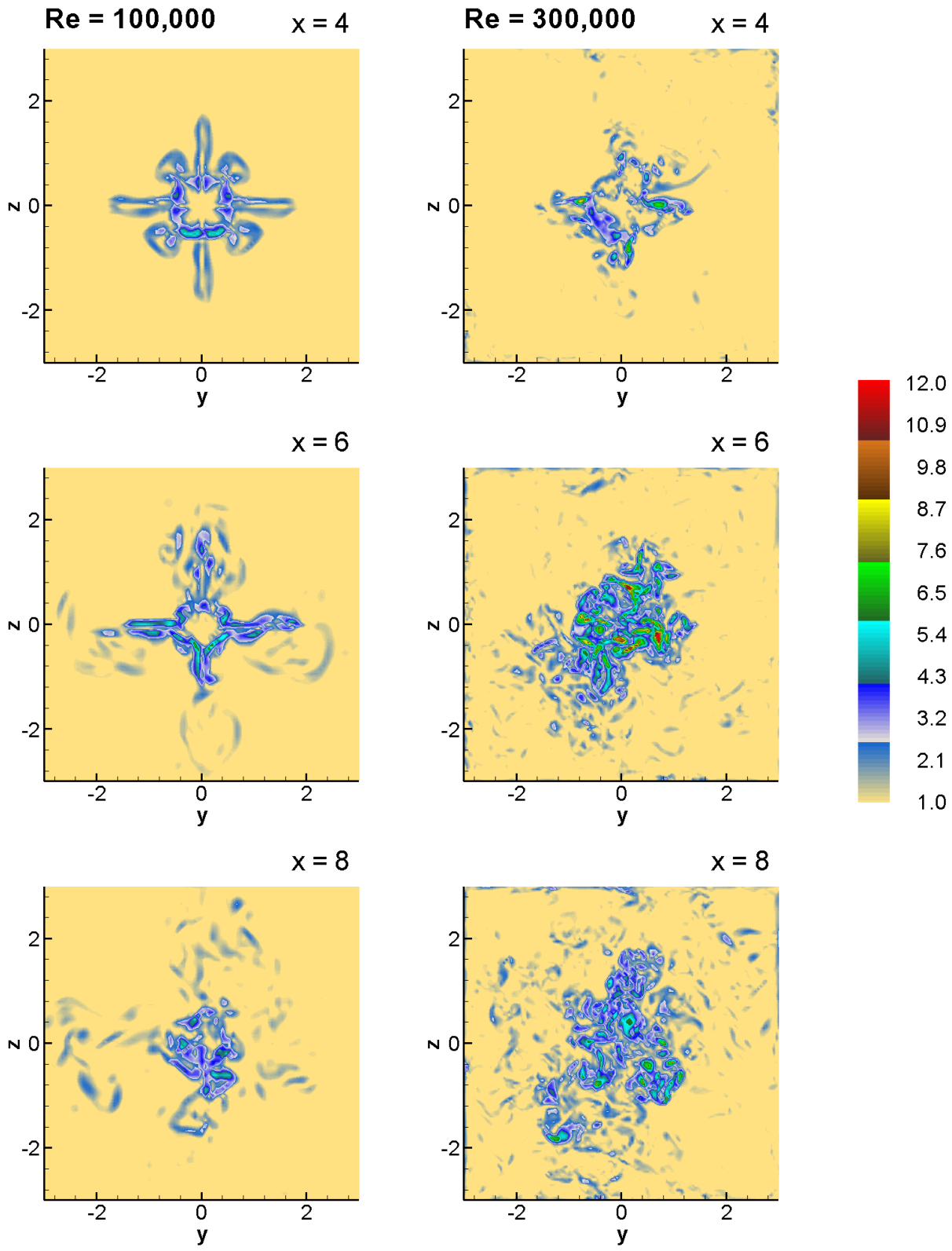

Figure 46. Contours of the instantaneous vorticity magnitude $|\Omega|$ for three cross sections in the two Reynolds numbers simulated.

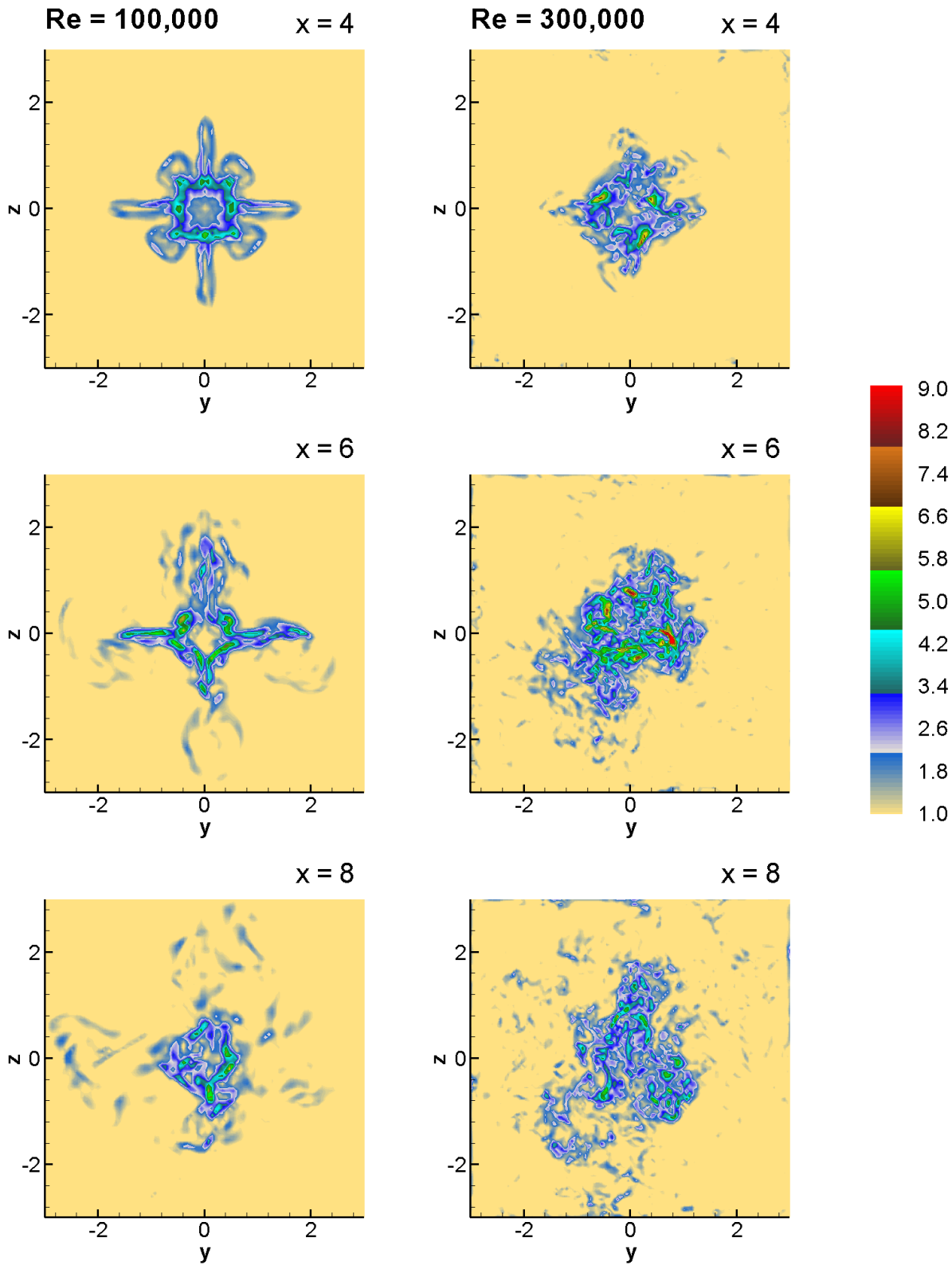

Figure 47. Contours of the instantaneous vorticity magnitude $|S|$ for three cross sections in the two Reynolds numbers simulated.

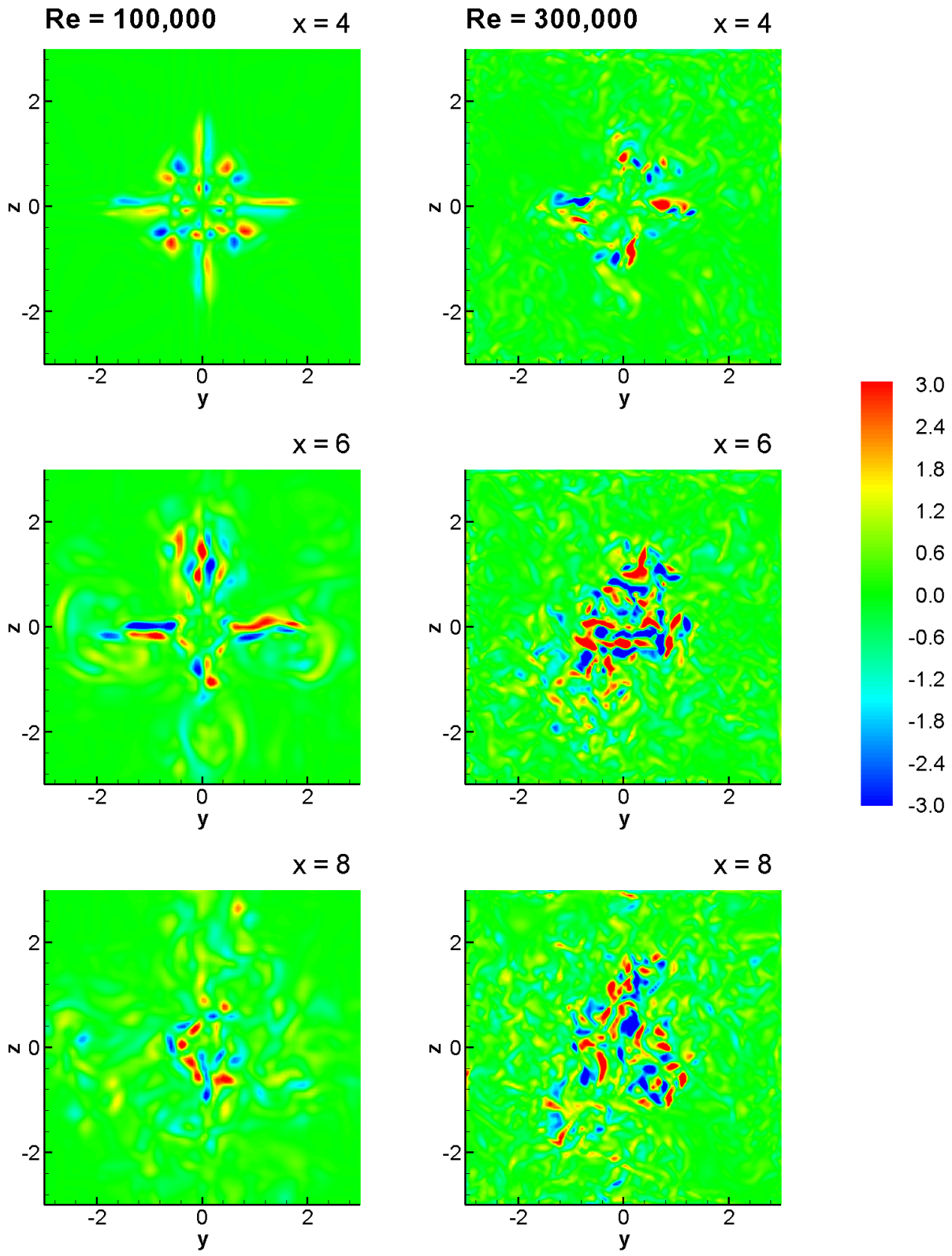

Figure 48. Contours of the instantaneous axial vorticity Ω_x for three cross sections in the two Reynolds numbers simulated.

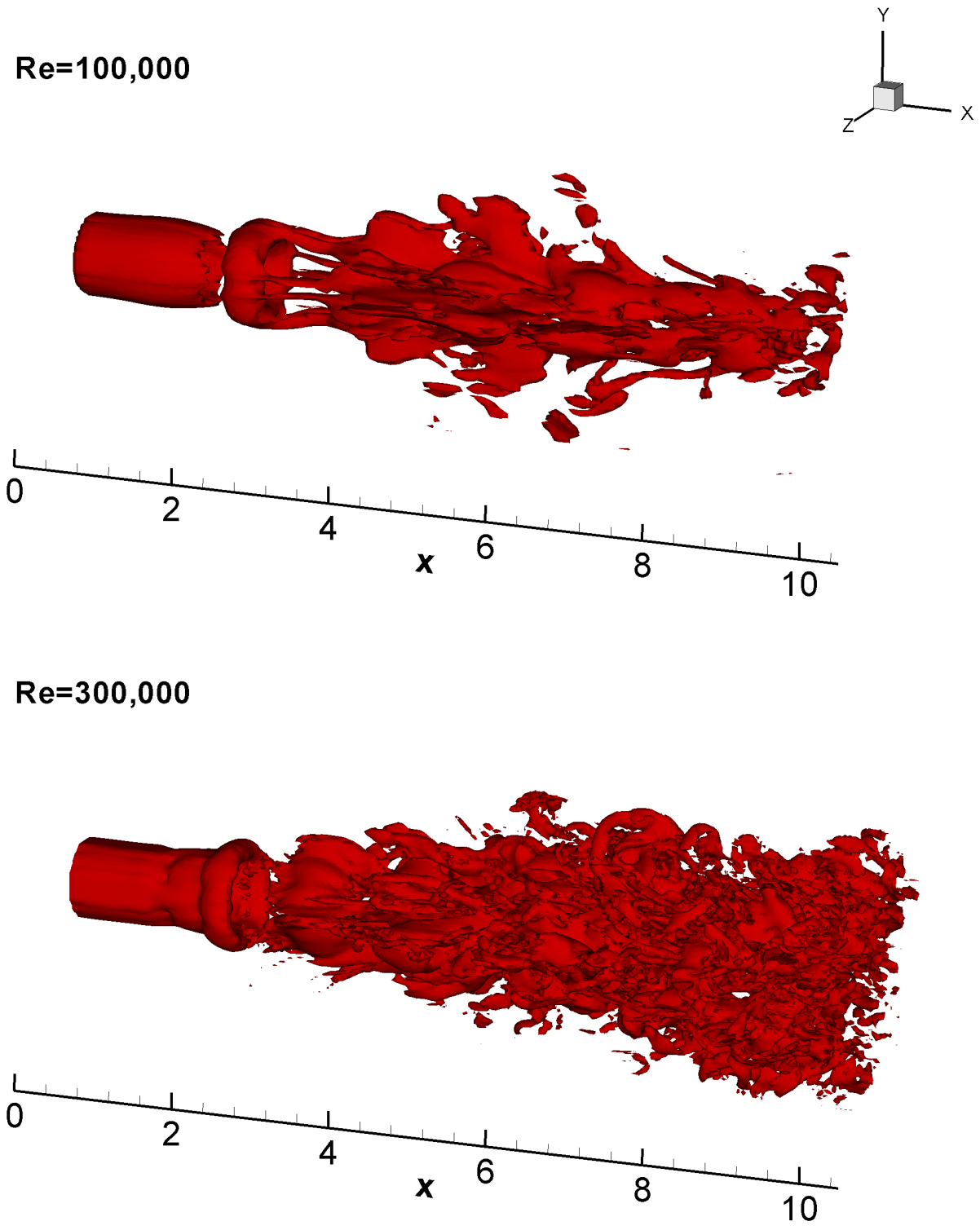

Figure 49. Instantaneous iso-surface of constant vorticity magnitude $|\Omega = 3|$ for the two Reynolds numbers simulated.

8. Particle Tracking Study

In this section, we present the results of a Lagrangian analysis of the computed flow field for Re = 100,000. This study is carried out by releasing into the flow and tracking the trajectories of several passive particles. The intensity of various flow quantities (pressure gradient, vorticity magnitude, and strain-rate) encountered by each particle at every point along its trajectory are then extracted by interpolation from the instantaneous flow field and plotted as a function of time. As we have already indicated, the results of this section are preliminary and serve to illustrate the manner in which a fish introduced into the flow experiences the instantaneous turbulent flow field.

The particle trajectories presented in this section were computed using the methodology presented in §4.4. Fifty particles were introduced into the jet every 10 time steps. The particles were released from the same location each time. The 50 release locations were evenly distributed among 5 concentric circles. The radius of the circles varied from 0.4 to 0.6d as measured from the centerline of the jet. All particles were released at $x = 1d$, which corresponds to the axial location where fish were released in the PNNL study. This procedure of releasing 50 particles every 10 time steps continued for more than 1800 time steps. During this time, more than 9000 particles were released into the jet, and more than 3000 of the particles subsequently exited the domain during that same time. In the following, we concentrate on only two of the release locations. The results from the other release locations were consistent with the two release locations that we present here.

Figs. 50 and 51 show the trajectories of over 150 particles released from a radial location of 0.45 and 0.6, respectively. (The radius of the jet is 0.5.) We reiterate that for a given figure the only difference between any two particles is that it was released at a different time. The color of the particles is not significant, and the different colors are only used to help differentiate among the different trajectories. Both figures show that the particles follow trajectories that are consistent with the overall structure of the jet. That is, within the potential core of the jet, the trajectories are very similar. However, once the particles get into the turbulent region of the jet ($x > 4d$),

they follow widely different trajectories. A close look at some of the trajectories in Fig. 50 shows that several of the particles, near the exit of the computational domain, reverse direction and begin traveling in the negative x direction. Another particle in Fig. 50, a red-colored particle at the bottom of the figure, is transported outside of the high-momentum region of the jet and follows a straight and probably very slow path—first it goes straight down and then turns and heads straight toward the exit. Many of the particles in Fig. 51 follow a winding or twisting trajectory. Some of the particles have this twisting trajectory even in the potential core region. These twisting trajectories are the result of the axial vorticity of the jet that we discussed in §6 on the instantaneous flow field.

Figs. 52 and 53 show the pressure gradient, vorticity magnitude, and strain rate that each particle from Figs. 50 and 51 experiences as it moves through the flow field The quantities are plotted with respect to the time since their release t_r. Both of these figures show very clearly that the particles experience a wide range of pressure gradients, vorticity magnitudes, and strain rates. The maximum vorticity magnitudes and strain rates occur at times near and greater than 10, which would be well into the turbulent region for most of the particles. (A particle with an average u velocity of 0.5 which is released at $x = 1d$ would be located at $x = 6d$ after $t_r = 10$.) Both plots also show that even during the early times $0 < t_r < 5$, the vorticity magnitudes and strain rates vary from 2 to 5. These early times correspond to the times when the particles are in the potential core and travel along similar trajectories (Figs. 50, 51). All of the time histories shown in Figs. 52 and 53 show a distinct tailing at large times. These particles have likely traveled into a slow moving region of the flow field, and since these regions have low velocities the particles experience little vorticity and strain. Most of the particles leave the computational domain at much earlier times.

The small sample of trajectories and time-records presented here exhibit trends that were also observed in the PNNL experiments when live fish were introduced into the flow. For instance, it was quite common for fish to experience intense bending and flexing of their bodies and undergo a tumbling-like motion. As we discussed above, there are several particles whose trajectories exhibit similar complex twisting patterns in the immediate vicinity of the jet. It was also observed in the laboratory that fish would frequently reverse direction and move upstream

toward the nozzle. A few of the trajectories we have obtained here do exhibit this behavior, which can be easily explained by the complexity of the instantaneous velocity field discussed in the previous section. Finally, it was quite common to observe in the laboratory erratic injury and mortality patterns. That is, the severity of the biological effects experienced by fish introduced into the flow at different instants in time but through the same injection tube would seem to depend on the time instant they were released. The time-records shown in Figs. 52 and 53 suggest a similar trend as particles released from the same point but at different times encounter widely different flow-induced loads along their trajectories—a trend that is not surprising given the chaotic nature of the instantaneous jet flow field.

In summary, the results presented here underscore the need to supplement the numerical simulations of the flow field with Lagrangian studies to fully explain the injury and mortality patterns observed in the laboratory. For such an undertaking to yield quantitatively meaningful results, however, a model for tracking the trajectories of three-dimensional fish-like bodies in the instantaneous turbulent flow should be developed. This model should account for the flexing and bending of the fish body and the effect that the presence and complex deformations of the fish have into the local flow. Given the progress we have already made and the experience gained from the application of a similar, albeit simpler, model that is only applicable to steady flows (the so-called virtual-fish model), such an undertaking is well within reach and could be pursued as part of future research.

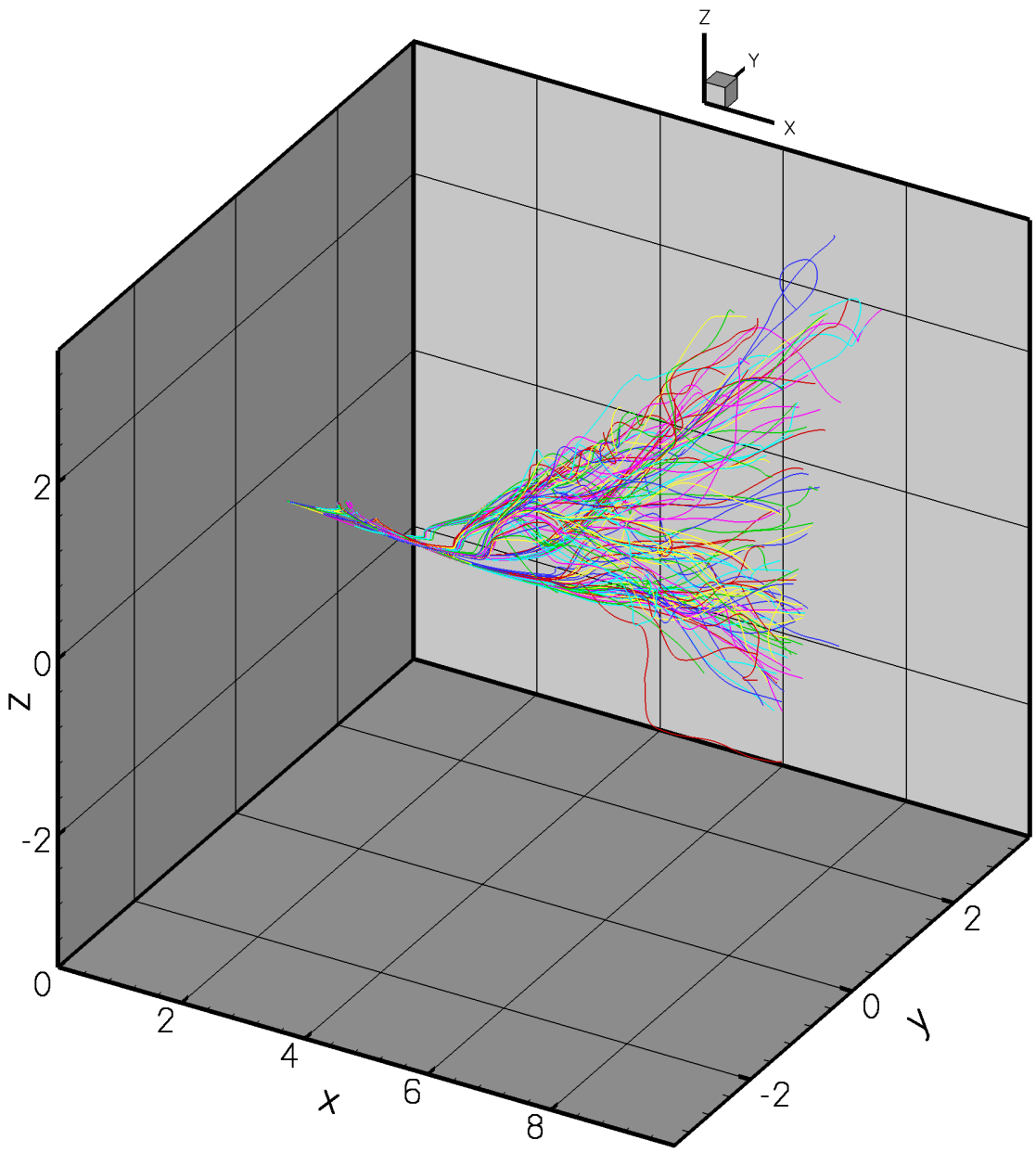

Figure 50. Trajectories of fluid particles released from $x = 1d$, $y = -0.25d$, $z = 0.375d$ ($r = 0.45d$). One particle was released every 10 time steps for a total of 150 particles.

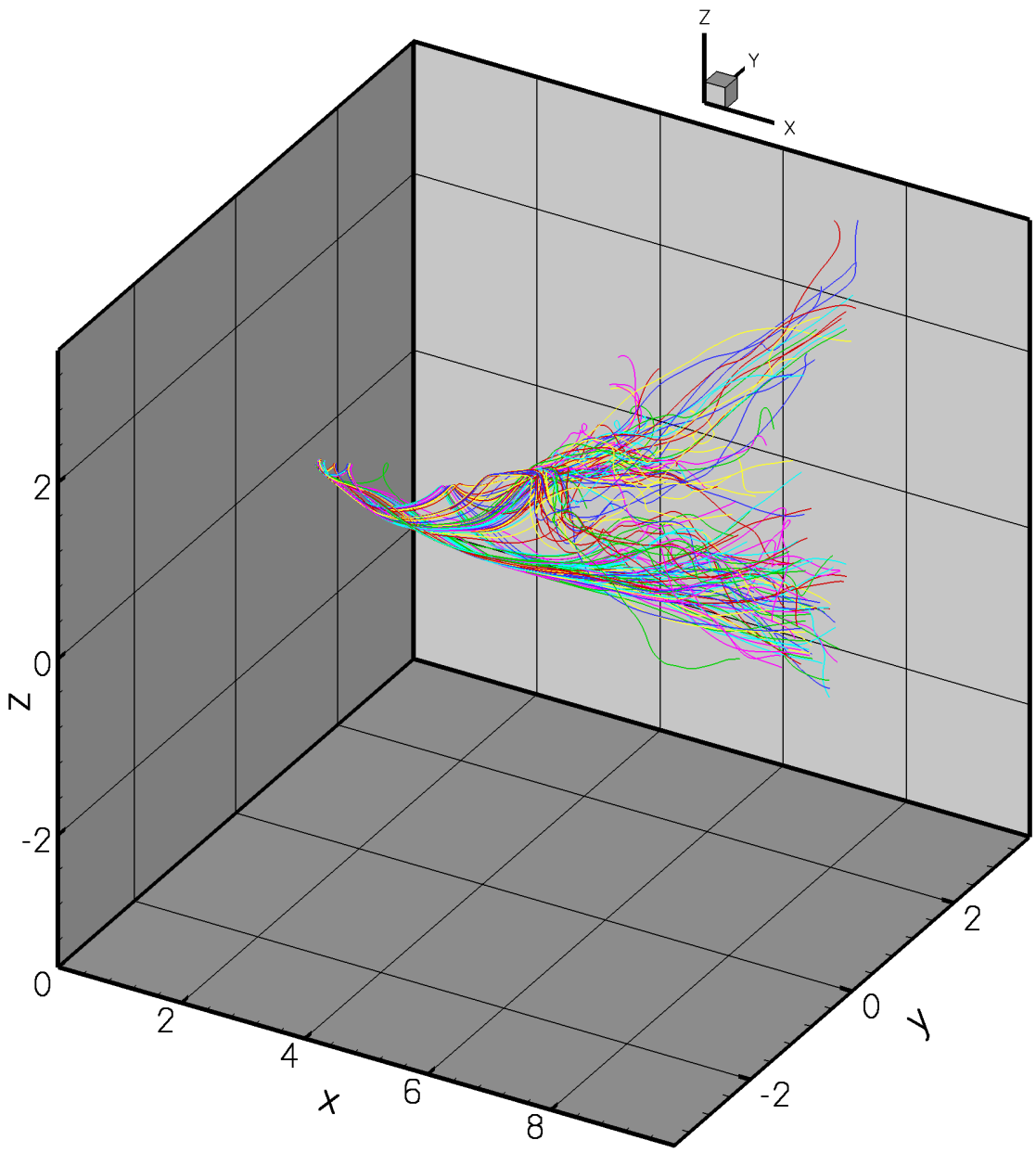

Figure 51. Trajectories of fluid particles released from $x = 1d$, $y = 0.35d$, $z = 0.49d$ ($r = 0.60d$). One particle was released every 10 time steps for a total of 150 particles.

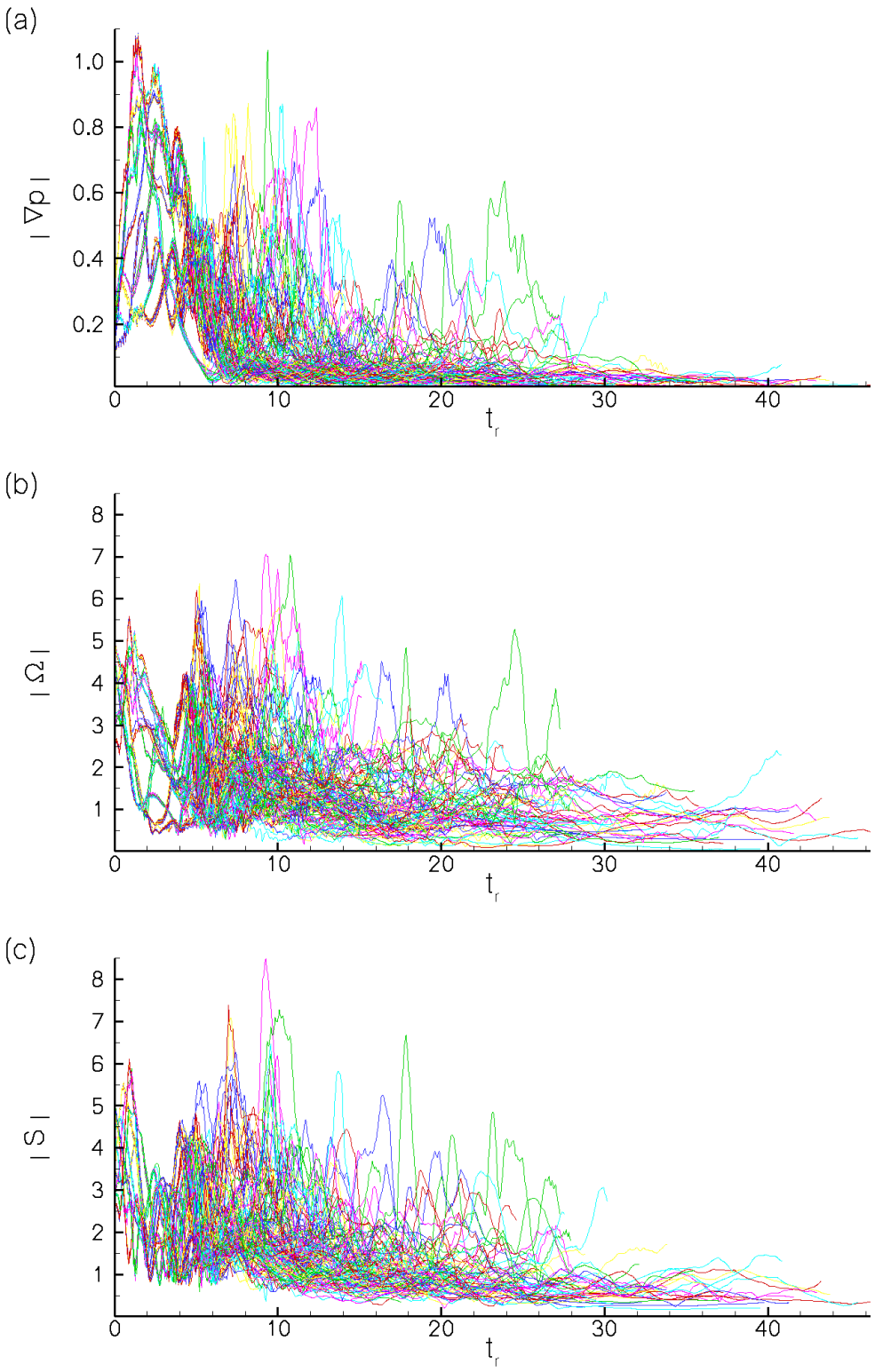

Figure 52. Time records of pressure gradient (a), vorticity magnitude (b), and strain rate (c) for along the particle trajectories shown in Fig. 50 (t_r is the time elapsed from the moment each particle was released).

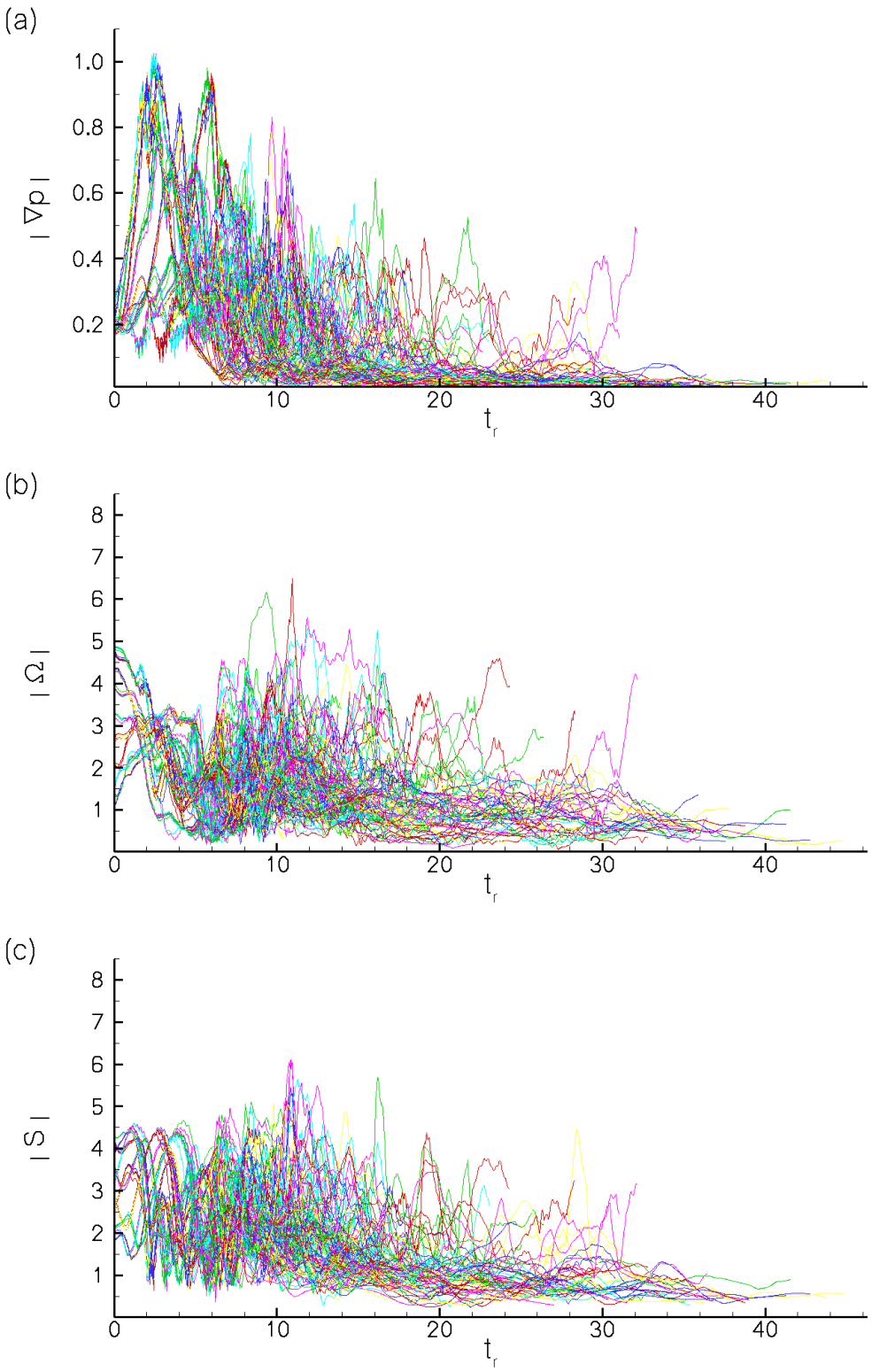

Figure 53. Time records of pressure gradient (a), vorticity magnitude (b), and strain rate (c) for along the particle trajectories shown in Fig. 51 (t_r is the time elapsed from the moment each particle was released).

9. Conclusions and Recommendations

In this section, we summarize the work and discuss its implications and importance. We also discuss areas of future research that are needed to further interpret the results of the PNNL experiments with real fish. Finally, we underscore the need for a realistic fish-tracking algorithm and outline a numerical approach for developing such a model.

1. Unsteady (LES) numerical simulations have been carried out for the turbulent flow through a circular jet issuing into a stagnant tank. The computed flow fields at two Reynolds numbers (100,000 and 300,000) were compared with the PNNL experimental data and found to be in good overall agreement. Some discrepancies between the data and the numerical simulations could be due to the lack of a precise description of the conditions at the exit of the experimental nozzle. Note that the near field evolution of jet flows is extremely sensitive to small disturbances at the inlet and differing levels of turbulence at the nozzle exit, thus, inexact specification of inlet conditions could be a major source of uncertainty in the comparison with measurements. However, in the fully turbulent region the experiments and computations were in good agreement—especially the calculated turbulence statistics.

2. Analysis of the computed instantaneous flow fields and comparisons with the time-averaged flow clearly demonstrates that unsteady flow analysis is essential for understanding the interaction of fish with the flow that was observed in the laboratory. The instantaneous flow is characterized by fluctuations of all quantities of interest (vorticity, shear stresses, pressure gradients) that can be considerably higher than the mean. Eddies of various sizes are continuously generated in the flow, interact with each other, and break-up into smaller eddies. Regions of very high instantaneous strain and vorticity, which can be potentially hazardous to passing fish, appear and disappear in a random manner throughout the flow field, even several diameters downstream of the nozzle.

3. It is important to recognize that a fish introduced into the flow interacts with and gets injured by the instantaneous flow. However, out of the continuous range of eddy sizes in a turbu-

lent flow, only eddies whose size is comparable to the fish body (fish-sized eddies) are likely to inflict the most serious damage. It is, therefore, essential that the energy content of such fish-sized eddies be correctly resolved. The LES formulation employed here is perhaps the best modeling alternative for resolving such eddies and quantifying the flow gradients associated with them. Even though LES modeling of flows in hydropower turbines is not presently possible, due to the excessive computational resources required, LES of the "simple" model flows used to conduct experiments with live fish, such as the jet flow considered here, are certainly within reach of present day computers. For wall-bounded flows like those in a hydropower plant, a very large-eddy simulation approach (coarser grids in conjunction with more sophisticated turbulence models) should be adopted.

4. To further understand the laboratory video recordings of live fish, we introduced into the flow passive particles and tracked their trajectories in a fully unsteady manner. Even though treating fish as passive particle is not a good approximation, especially since the size of the fish used in the PNNL experiment was comparable to the jet diameter, such numerical experiment did lead to some useful insights. For instance, we found that particles originating from the same spatial location but at different time instants could experience widely different histories of various flow-induced loads along their trajectories. This is, of course, consistent with the chaotic nature of the flow, but it further underscores the need for combining unsteady flow analysis with laboratory experiments to facilitate the interpretation of the results of these experiments.

5. The instantaneous flow fields obtained from these calculations could be analyzed using extensive particle tracking studies to develop a comprehensive understanding of the correlation between particle release location and the flow-induced loads it experiences. As we discussed above, due to the chaotic nature of turbulent flows particles originating from the same spatial location but at different times are bound to have widely different fate. Therefore, correlations between release location and flow loads can only be established in a statistical sense. For example, by releasing sufficiently many particles from a given location, we can calculate the probability that a particle will experience a given threshold of, say, shearing load or turbulent intensity before it exits the computational domain. Such probability distributions can be used to interpret and

further clarify the results of the PNNL experiments with live fish. This will require obtaining and analyzing the full record of the PNNL experimental observations of fish passage, including both the trajectory video recordings and the injury and/or mortality records for each fish.

6. It is important to recognize that particle studies can be useful only up to a certain point, especially when the fish used in the experiments are very large compared to the characteristic dimensions of the flow field (for example, the jet diameter in this case). This is because, even if one is to ignore the swimming capacity of such fish, their presence in the flow will have a significant effect on the local flow itself—unlike passive particles, which are simply transported by the flow without altering it. Therefore, a more rigorous treatment of this problem will require the development of an advanced numerical model that treats fish as full three-dimensional objects, which are not only transported by the flow but also influence the local flow as well. Although the existing virtual fish model incorporates some of these elements, in its present form it is valid only for steady flows, does not account for the effects of fish on the flow, and treats fish as rigid objects (no flexing and bending is allowed). Therefore, the virtual fish model cannot be useful in the context of the unsteady analysis we believe is essential for understanding the fish-flow interaction. A realistic fish-tracking algorithm can be developed using the so-called immersed boundary method, which has been successfully applied to many biological flows. Such a numerical fish will be flexible, that is, it will be deformed by the flow, and its trajectory will be computed in an unsteady manner and fully coupled with the flow. That is, the presence of the fish body at a given point in the flow field will result in a drag force exerted on the local fluid volume. Such a force will be incorporated in the governing flow equations and will in turn affect the evolution of the flow field at subsequent times. The development of such a sophisticated model will undoubtedly be a major undertaking but it is now well within our reach. In conjunction with properly designed experiments with real fish, such a model could serve as a powerful tool for clarifying and precisely quantifying the links between the flow field and injury and mortality rates.

9. References

Boris, J. P., Grinstein, F. F., Oran, E. S., and Kolbe, R. L. (1992). New insights into large eddy simulation. Fluid Dynamics Research. 10, 199-228.

Brandt, A. (1977). Multi-level adaptive solutions to boundary-value problems. Mathematics of Computation. 31, 333-390.

Coutant, C. C., and Whitney, R. R. (2000). Fish behavior in relation to passage through hydropower turbines: A review. Transactions of the American Fisheries Society 129, 351-380.

Danaila, I., Dušek, J., and Anselmet, F. (1997). Coherent structures in a round, spatially evolving, unforced, homogeneous jet at low Reynolds numbers. Physics of Fluids. 9, 3323-3342.

Darmofal, D. L. and Haimes, R. (1996). An analysis of 3D particle path integration algorithms. Journal Computational Physics. 123, 182-195.

Fisher, R. K., Franke, G. F., March, P. A., Mathur, D., and Sotiropoulos, F. (1999). Increasing fish survival prospects at hydro plants. Hydropower and Dams 5, 77-82.

Franke, G. F., Webb, D. R., Fisher, R. K., Mathur, D., Hopping, P., March, P., Headrick, M., Laczo, I., Ventikos, Y., and Sotiropoulos, F. (1997). Development of environmentally friendly advanced hydropower turbine system design concepts. Voith Hydro, Inc. Report No. 2677-0141, US Department of Energy Contract DE-AC07-96ID13382.

Gutmark, E. J. and Grinstein, F. F. (1999). Flow control with noncircular jets. Annual Review of Fluid Mechanics. 31, 239-272.

Grinstein, F. F., Oran, E. S., and Boris, J. P. (1987). Direct numerical simulation of axisymmetric jets. AIAA Journal. 23, 92-98.

Grinstein, F. F. (1994). Open boundary conditions in the simulation of subsonic turbulent shear flows. Journal Computational Physics. 115, 43-55.

Grinstein, F. F. and DeVore C. R. (1996). Dynamics of coherent structures and transition to turbulence in free square jets. Physics of Fluids. 8, 1237-1251.

Grinstein, F. F., Gutmark, E. J., Parr, T. P., Hanson-Parr, D. M., and Obeysekare, U. (1996). Streamwise and spawise vortex interaction in an axisymmetric jet. A computational and experimental study. Physics of Fluids. 8, 1515-1524.

Groves, A. B. (1972). Effects of hydraulic shearing actions on juvenile salmon (Summary Report). Northwest Fisheries Center, National Marine Fisheries Service, Seattle, Washington.

Hinze, J. O. (1975). Turbulence. McGraw-Hill, New York.

Killgore, K. J., Miller, A. C., and Conley, K. C. (1987). Effects of turbulence on yolk-sac larvae of paddlefish. Transactions of the American Fisheries Society 116, 670-673.

Li, N., Balaras, E., and Piomelli, U. (2000). Inflow conditions for large-eddy simulations of mixing layers. Physics of Fluids. 12, 935-938.

Lin, F. B. and Sotiropoulos, F. (1997a). Assessment of artificial dissipation models for three-dimensional, incompressible flow solutions. ASME Journal Fluids Engineering. 119, 314-324.

Lin, F. B. and Sotiropoulos, F. (1997b). Strongly-coupled multigrid method for 3-D incompressible flows using near-wall turbulence closures. ASME Journal Fluids Engineering. 119, 331-340.

Jameson A. (1985). Multigrid algorithms for compressible flow calculations. MAE Report 1743, Princeton University.

Lasheras, J. C. and Prestridge, K. (1997). Three-dimensional vorticity dynamics in coflowing jets subjected to axial and azimuthal forcing. AIAA Paper 98-1880.

Lund, T. S., Wu, X., and Squires, K. D. (1998). Generation of turbulent inflow data for spatially-developing boundary layer simulations. Journal of Computational Physics. 140, 233-258.

Martin, J. E. and Meiburg, E. (1991). Numerical investigation of three-dimensionally evolving jets subject to axisymmetric and azimuthal perturbations. Journal of Fluid Mechanics. 230, 271-318.

Merkle, C. L. and Athavale, M. (1987). Time-accurate unsteady incompressible flow algorithms based on artificial compressibility. AIAA Paper 87-1137.

Murman, E. M. and Powell, K. G. (1989). Trajectory integration in vortical flows. AIAA Journal. 27, 982-984.

Morgan, R. P., II, Ulanowicz, R. E., Rasin, Jr., V. J. Noe, L. A., and Gray, G. B. (1976). Effects of shear on eggs and larvae of striped bass, *Morone saxatili*s, and white perch, *M. americana*. Transactions of the American Fisheries Society. 105, 149-154.

Neitzel, D. A., Richmond, M. C., Dauble, D. D., Mueller, R. P., Moursund, R. A., Abernethy, C. S., Guensch, G. R., and Cada, G. F. (2000). Laboratory studies on the effects of shear and turbulence on fish: Final report. DOE/ID-10822. U.S. Department of Energy, Idaho Operations Office, Idaho Falls, Idaho.

Piomelli, U. (1999). Large-eddy simulation: achievements and challenges. Progress Aerospace Sciences. 35, 355-362.

Poinsot, T. J. and Lele, S. K. (1992). Boundary conditions for direct simulations of compressible viscous flows. Journal Computational Physics. 101, 104-129.

Rajaratnam, N. (1975). Turbulent jets. Elsevier, New York.

Samimy, M., Zaman, K. B. M. Q., and Reeder, M. F. (1993). Effect of tabs on the flow and noise field of an axisymmetric jet. AIAA Journal. 31, 609-619.

Smagorinsky, J. (1963). General circulation experiments with the primitive equations. I. The basic experiment. Monthly Weather Review. 91, 99-164.

Sotiropoulos, F. and Ventikos, Y. (1998). Transition from bubble vortex breakdown to a columnar vortex in a closed cylinder with a rotating lid. International Journal of Heat and Fluid Flow. 19, 446-458.

Sotiropoulos, F. (2001). Progress in modeling 3D shear flows using RANS equations and advanced turbulence closures. Calculation of Complex Turbulent Flows. Advances in Fluid Mechanics Series, Vol. 27, WIT Press, Southampton UK.

Thompson, K. W. (1990). Time-dependent boundary conditions for hyperbolic systems, II. Journal Computational Physics. 89, 439-461.

Turnpenny, A. W. H., Davis, M. H., Fleming, J. M., and Davies, J. K. (1992). Experimental studies relating to the passage of fish and shrimps through tidal power turbines. Marine and Freshwater Biology Unit, National Power, Fawley, Southhampton, Hampshire, England.

Van Dyke, M. (1982). Album of fluid motion, Parabolic Press, Stanford, California.

Wilson, R. V. and Demuren, A. O. (1998). Numerical simulation of turbulent jets with rectangular cross-section. ASME J Fluids Engineering. 120, 285-290.

Zaman, K. B. M. Q., Reeder, M. F., and Samimy, M. (1994). Control of an axisymmetric jet using vortex generators. Physics of Fluids. 6, 778-793.